

Linköping Studies in Science and Technology

Dissertation No. 1314

Growth and Phase Stability Studies of Epitaxial Sc-Al-N and Ti-Al-N Thin Films

Carina Höglund



Linköping University
INSTITUTE OF TECHNOLOGY

Thin Film Physics Division
Department of Physics, Chemistry, and Biology (IFM)
Linköping University, Sweden

Linköping 2010

THE COVER IMAGE

The cover shows an energy landscape of the wurtzite $\text{Sc}_{0.5}\text{Al}_{0.5}\text{N}$ solid solution as a function of c/a and volume. The global energy minimum on the front page corresponds to a wurtzite phase and is connected with a shallow region originating from a residue of the hexagonal ScN-phase on the backside. The result from the calculation on which the image is based, is a part of the explanation for the high piezoelectric response reported in the $\text{Sc}_{1-x}\text{Al}_x\text{N}$ system. The original image is found in *Origin of the anomalous piezoelectric response in wurtzite $\text{Sc}_x\text{Al}_{1-x}\text{N}$ alloys*, Physical Review Letters **104**, 137601 (2010).

Thanks to Björn Alling for letting me use his calculations for the cover. The color scheme is of course chosen in my very special way!

ISBN: 978-91-7393-391-9

ISSN: 0345-7524

Printed by LiU-Tryck, Linköping, Sweden

ABSTRACT

This Thesis treats the growth and characterization of ternary transition metal nitride thin films. The aim is to probe deep into the Ti-Al-N system and to explore novel Sc-Al-N compounds. Thin films were epitaxially grown by reactive dual magnetron sputtering from elemental targets onto single-crystal substrates. Ion beam analyses were used for compositional analysis and depth profiling. Different X-ray diffraction techniques were employed, *ex situ* using Cu radiation and *in situ* during deposition using synchrotron radiation, to achieve information about phases, texture, and thickness of films, and to follow roughness evolution of layers during and after growth. Transmission electron microscopy was used for overview and lattice imaging, and to obtain lattice structure information by electron diffraction.

In the Sc-Al-N system, the perovskite Sc_3AlN was for the first time synthesized as a thin film and in single phase, with a unit cell of 4.40 Å. Its hardness was found to be 14.2 GPa, elastic modulus 21 GPa, and room temperature resistivity 41.2 $\mu\Omega\text{cm}$. Cubic solid solutions of $\text{Sc}_{1-x}\text{Al}_x\text{N}$ can be synthesized with AlN molar fraction up to ~60%. Higher AlN contents yield three different epitaxial relations to ScN(111), namely, #1 $\text{Sc}_{1-x}\text{Al}_x\text{N}(0001) \parallel \text{ScN}(111)$ with $\text{Sc}_{1-x}\text{Al}_x\text{N}[\bar{1}2\bar{1}0] \parallel \text{ScN}[\bar{1}\bar{1}0]$, #2 $\text{Sc}_{1-x}\text{Al}_x\text{N}(10\bar{1}1) \parallel \text{ScN}(111)$ with $\text{Sc}_{1-x}\text{Al}_x\text{N}[\bar{1}2\bar{1}0] \parallel \text{ScN}[\bar{1}\bar{1}0]$, and #3 $\text{Sc}_{1-x}\text{Al}_x\text{N}(10\bar{1}1) \parallel \text{ScN}(113)$. An *in situ* deposition and annealing study of cubic $\text{Sc}_{0.57}\text{Al}_{0.43}\text{N}$ films showed volume induced phase separation into ScN and wurtzite-structure AlN, via nucleation and growth at the domain boundaries. The first indications for phase separation are visible at 1000 °C, and the topotaxial relationship between the binaries after phase separation is $\text{AlN}(0001) \parallel \text{ScN}(001)$ and $\text{AlN}\langle 0\bar{1}10 \rangle \parallel \text{ScN} \langle \bar{1}10 \rangle$. This is compared with $\text{Ti}_{1-x}\text{Al}_x\text{N}$, for which an electronic structure driving force leads to spinodal decomposition into isostructural TiN and AlN already at 800 °C. First principles calculations explain the results on a fundamental physics level. Up to ~22% ScN can under the employed deposition conditions be dissolved into wurtzite $\text{Sc}_{1-x}\text{Al}_x\text{N}$ films, while retaining a single-crystal structure and with lattice parameters matching calculated values.

In the Ti-Al-N system, the Ti_2AlN phase was synthesized epitaxially by solid state reaction during interdiffusion between sequentially deposited layers of AlN(0001) and Ti(0001). When annealing the sample, N and Al diffused into the Ti layer, forming $\text{Ti}_3\text{AlN}(111)$ at 400 °C and $\text{Ti}_2\text{AlN}(0001)$ at 500 °C. The Ti_2AlN formation temperature is 175 °C lower than earlier reported results. Another way of forming Ti_2AlN phase is by depositing understoichiometric TiN_x at 800 °C onto $\text{Al}_2\text{O}_3(0001)$. An epitaxial $\text{Ti}_2\text{Al}(\text{O},\text{N})(0001)$ oxynitride forms close to the interface between film and substrate through a solid state reaction. Ti_4AlN_3 was, however, not possible to synthesize when depositing films with a Ti:Al:N ratio of 4:1:3 due to competing reactions. A substrate temperature of 600 °C yielded an irregularly stacked $\text{Ti}_{n+1}\text{Al}_n$ layered structure because of the low mobility of Al ad-atoms. An increased temperature led to Al deficiency due to outdiffusion of Al atoms, and formation of the Ti_2AlN phase and a $\text{Ti}_{1-x}\text{Al}_x\text{N}$ cubic solid solution.

POPULÄRVETENSKAPLIG SAMMANFATTNING

Utvecklingen inom materialforskningen går allt mer mot skräddarsydda material för enskilda tillämpningar. Materialen kan ha *en* egenskap som perfekt matchar en viss tillämpning, eller vara multifunktionella och därmed ha *flera* kvaliteter samtidigt. I många fall kan man förbättra ett materials egenskaper genom att belägga det med ett tunt skikt av ett annat material, en såkallad *tunnsfilm*. Vi hittar dessa tunna filmer i all världens produkter, exempelvis i stekpannans beläggning, som förgyllning av smycken, på fönsterrutan, som skyddande skikt på verktyg, eller i en stor andel av elektronikkomponenterna i datorer och mobiltelefoner. Denna avhandling handlar om nya material i tunnsfilmsform.

I ett fast tillstånd ordnar sig atomerna i oorganiska material oftast i strukturer och bildar *kristaller*. Forskningen har idag gått så långt att man nästintill kan placera atomerna på önskad plats i kristallen. Fysikens lagar gäller dock alltså och termodynamiken ger oss en antydning om vilka materialstrukturer som är möjliga. Kvantmekaniska beräkningar är ett utmärkt hjälpmedel för att förutsäga hur termodynamiken yttrar sig i experiment. Den nyttjade beläggningstekniken *magnetronsputtring* kan i många fall vidga möjligheterna att tillverka material som inte är termodynamiskt stabila, utan bara metastabila. Tunnsfilmerna läggs på ett *substrat*, vilket här är ett bärande material som har en bestämd ordning av atomer för att kunna fungera som mall för tunnsfilmsatomerna. Ju mindre skillnaden mellan atomavstånden i substrat och tunnsfilm är, desto större är möjligheten att bilda den önskade strukturen. En tunnsfilm som är anpassad till en substratmall sägs vara *epitaxiell*, från grekiskans *epi* (ovanpå) och *taxi* (ordnat).

För att studera tunnsfilmerna används tekniker som elektronmikroskopi, röntgendiffraktion och jonstråleanalys. De möjliggör undersökningar på atomnivå. Man kan exempelvis se filmens tjocklek, fördelningen av atomsorter i materialet, avståndet mellan atomerna eller strukturen av kristallen. Utvecklingen går alltså mot att kombinera olika tekniker. Jag har kombinerat röntgendiffraktion med magnetronsputtring för att studera hur materialet utvecklas under syntetisering, eller med värmebehandling för att följa vad som händer när materialet utsätts för höga temperaturer.

En stor del av min forskning har ägnats åt att belägga tunna filmer ur ett materialsystem som i princip var outforskat innan det här arbetet startade, nämligen Sc-Al-N. Jag har tillverkat det första fasrena Sc₃AlN-materialet och visat att det är termodynamiskt stabilt. Jag har visat att lösligheten av AlN i ScN är maximalt ~60% och av ScN i AlN maximalt

~22% under applicerade beläggningsförhållanden. Genom att värmebehandla $\text{Sc}_{1-x}\text{Al}_x\text{N}$ -legeringar har jag kunnat visa att materialet fasset separerar på ett annorlunda sätt än vad som är känt från $\text{Ti}_{1-x}\text{Al}_x\text{N}$. Beräkningar förklarar att skillnaden beror på att det finns en elektronisk drivkraft för $\text{Ti}_{1-x}\text{Al}_x\text{N}$ att omvandlas, medan $\text{Sc}_{1-x}\text{Al}_x\text{N}$ berörs av den stora skillnaden mellan atomavstånden i ScN och AlN och den därpå följande elastiska töjningen inne i legeringen.

Jag har även presenterat två nya sätt att belägga Ti_2AlN och sänkt den lägsta syntestemperaturen för ett sådant material med 175 °C, till 500 °C. Man belägger flera skikt av AlN och Ti och värmer sedan dessa. Vid värmebehandlingen sker en reaktion i det fasta tillståndet och Ti_2AlN bildas. Alternativt kan man belägga TiN, på Al_2O_3 -substrat vid 800 °C. Om TiN är kvävefattigt blir det här materialet väldigt benäget att reagera med substratet för att bilda Ti_2AlN . Avslutningsvis har jag insett att det termodynamiskt stabila Ti_4AlN_3 -materialet är mycket svår att tillverka som en tunnfilm.

PREFACE

The work presented in this Thesis is a result of my PhD studies in the Thin Film Physics Division at Linköping University, starting in 2006. The work is a continuation of the work leading to my Licentiate Thesis (No. 1344, Linköping Studies in Science and Technology: *Reactive Magnetron Sputter Deposition and Characterization of Thin Films from the Ti-Al-N and Sc-Al-N Systems*), which I presented in 2008. The goal of my research has been to increase the knowledge about functional ternary transition metal nitrides deposited as thin films by reactive magnetron sputtering. Films have been deposited both in Linköping and with *in situ* X-ray diffraction at the European Synchrotron Radiation Facility in Grenoble, France. Model systems have been cubic and wurtzite solid solutions, $M_{n+1}AX_n$ phases, and perovskites in the Ti-Al-N and Sc-Al-N systems. Epitaxial growth is shown to be a useful synthesis route for the Ti_2AlN and Sc_3AlN phases as well as metastable $Sc_{1-x}Al_xN$ solid solutions. I have also taken part in introducing ion beam analysis as a useful technique in the every day thin film work at the department. The work was supported by the Swedish Research Council (VR) and the Swedish Foundation for Strategic Research (SSF). Most of the simulations were carried out at the National Supercomputer Centre (NSC), using resources allocated by the Swedish National Infrastructure for Computing (SNIC).

INCLUDED PAPERS AND MY CONTRIBUTION

PAPER 1

Sc₃AlN – A New Perovskite

C. Höglund, J. Birch, M. Beckers, B. Alling, Zs. Czigány, A. Mücklich,
and L. Hultman

European Journal of Inorganic Chemistry **8**, 1193 (2008).

I carried out the major part in the planning, synthesis and characterization,
and wrote the paper.

PAPER 2

*Cubic Sc_{1-x}Al_xN solid solution thin films deposited by reactive magnetron
sputter epitaxy onto ScN(111)*

C. Höglund, J. Bareño, J. Birch, B. Alling, Zs. Czigány, and L. Hultman

Journal of Applied Physics **105**, 113517 (2009).

I carried out the major part in the planning, synthesis and characterization,
and wrote the paper.

PAPER 3

*Effects of volume mismatch and electronic structure on the decomposition of ScAlN and
TiAlN solid solutions*

C. Höglund, B. Alling, J. Birch, M. Beckers, P. O. Å. Persson, C. Baehtz,
Zs. Czigány, J. Jensen, and L. Hultman

Submitted for publication

I carried out the major part in the planning, *in situ* and *ex situ* synthesis,
annealing, characterization, and wrote the paper.

PAPER 4

Wurtzite-structure $Sc_{1-x}Al_xN$ solid solution films grown by reactive magnetron sputter epitaxy – structural characterization and first-principles calculations

C. Höglund, J. Birch, B. Alling, J. Bareño, Zs. Czigány, P. O. Å. Persson, G. Wingqvist, A. Zukauskaitė, and L. Hultman

Submitted for publication

I carried out the major part in the planning, synthesis and characterization, and wrote the paper.

PAPER 5

Topotaxial growth of Ti_2AlN by solid state reaction in $AlN/Ti(0001)$ multilayer thin films

C. Höglund, M. Beckers, N. Schell, J. v. Borany, J. Birch, and L. Hultman

Applied Physics Letters **90**, 174106 (2007).

I took part in the planning, synthesis, *in situ* and *ex situ* annealing and characterization, and wrote the paper.

PAPER 6

$Ti_2Al(O,N)$ formation by solid state reaction between substoichiometric TiN thin films and $Al_2O_3(0001)$ substrates

P. O. Å. Persson, C. Höglund, J. Birch, and L. Hultman

Submitted for publication

I took part in the planning, synthesis and characterization (except for TEM), and contributed to the writing of the paper.

PAPER 7

The influence of substrate temperature and Al mobility on the microstructural evolution of magnetron sputtered ternary $Ti-Al-N$ thin films

M. Beckers, C. Höglund, C. Baetz, R. M. S. Martins, P. O. Å. Persson, L. Hultman, and W. Möller

Journal of Applied Physics **106**, 064915 (2009).

I took part in the planning, *in situ* and *ex situ* synthesis and characterization (except for XPS), and contributed to the writing of the paper.

RELATED PAPERS, NOT INCLUDED IN THE THESIS

PAPER 8

Origin of the anomalous piezoelectric response in wurtzite $Sc_xAl_{1-x}N$ alloys

F. Tasnádi, B. Alling, C. Höglund, G. Wingqvist, J. Birch, L. Hultman, and I. A. Abrikosov

Physical Review Letters **104**, 137601 (2010).

PAPER 9

Electronic structure of GaN and Ga investigated by soft X-ray spectroscopy and first-principles methods

M. Magnuson, M. Mattesini, C. Höglund, J. Birch, and L. Hultman

Physical Review B **81**, 085125 (2010).

PAPER 10

Electronic structure and anisotropy investigation of AlN

M. Magnuson, M. Mattesini, C. Höglund, J. Birch, and L. Hultman

Physical Review B **80**, 155105 (2009).

PAPER 11

Elastic properties and electro-structural correlations in ternary scandium-based cubic inverse perovskites: A first-principles study

M. Mattesini, M. Magnuson, F. Tasnádi, C. Höglund, I. A. Abrikosov, and L. Hultman

Physical Review B **79**, 125122 (2009).

PAPER 12

Stability of the ternary perovskites Sc_3EN ($E = B, Al, Ga, In$) from first principles

S. Mikhaylushkin, C. Höglund, J. Birch, Zs. Czigány, L. Hultman, S. I. Simak,
B. Alling, F. Tasnádi, and I. A. Abrikosov

Physical Review B **79**, 134107 (2009).

PAPER 13

A solid phase reaction between TiC_x thin films and Al_2O_3 substrates

P. O. Å. Persson, J. Rosén, D. R. McKenzie, M. M. M. Bilek, and C. Höglund

Journal of Applied Physics **103**, 066102 (2008).

PAPER 14

Electronic structure investigation of the cubic inverse perovskite Sc_3AlN

M. Magnuson, M. Mattesini, C. Höglund, I. A. Abrikosov, J. Birch, and L. Hultman

Physical Review B **78**, 235102 (2008).

PAPER 15

*Bonding mechanism in the nitrides Ti_2AlN and TiN : An experimental
and theoretical investigation*

M. Magnuson, M. Mattesini, S. Li, C. Höglund, M. Beckers, L. Hultman, and
O. Eriksson

Physical Review B **76**, 1 (2007).

ACKNOWLEDGEMENTS

I would like to thank everyone who directly or indirectly has been involved during the years leading to this Thesis. Special thanks go to the following persons, namely...

...my first supervisor *Lars Hultman*, who always has a few minutes for nice discussions and has an endless patience when reading manuscripts. Nothing is impossible!

...my second supervisor *Jens Birch*, for being one of the best persons to have around in research. He is just great!

...*Björn Alling*, for seeing my work from a theoretical point of view and at the same time understanding the experiments. Thanks for a nice collaboration!

...*Javier Bareño*, for spending endless of time discussing difficult stuff that no one else understands. I missed you when you left!

...*Manfred Beckers* for being my unofficial supervisor and helping me before I understood how things work.

...my nice colleagues in the *Thin Film, Plasma and Nanomaterials* groups, for making me look forward to go to work every day. We have had several scientific collaborations, but also a lot of fun during coffee breaks, lunches, on conferences, on the golf course, on the running course, on the skiing slopes and in the evenings at nice dinners, in pubs and on dance floors around the world!

...the *ROBL crew*, for helping me to make the ESRF beam times both successful and memorable!

...*Kalle, Thomas, Rolf, Inger* and everyone else around who helps me with all kind of things!

...all *friends outside research*, because it can not be healthy just to be around researchers. Sometimes my mind needs some rest and my body some exercising!

...my *family*, who always is there for me!

...and last but definitely not least *Richard*, for everything!

COPYRIGHT ACKNOWLEDGMENTS

PAPER 1:

Reprinted from Eur. J. Inorg. Chem. **8**, 1193 (2008), *Sc₃AlN – A new perovskite*, C. Höglund, J. Birch, M. Beckers, B. Alling, Zs. Czigány, A. Mücklich, and L. Hultman, with kind permission from Wiley-VCH Verlag GmbH & Co. KGaA, Weinheim.

PAPER 2:

Reprinted from J. Appl. Phys. **105**, 113517 (2009), *Cubic Sc_{1-x}Al_xN solid solution thin films deposited by reactive magnetron sputter epitaxy onto ScN(111)*, C. Höglund, J. Bareño, J. Birch, B. Alling, Zs. Czigány, and L. Hultman, with kind permission from the American Institute of Physics.

PAPER 5:

Reprinted from Appl. Phys. Lett. **90**, 174106 (2007), *Topotaxial growth of Ti₂AlN by solid state reaction in AlN/Ti(0001) multilayer thin films*, C. Höglund, M. Beckers, N. Schell, J. v. Borany, J. Birch, and L. Hultman, with kind permission from the American Institute of Physics.

PAPER 7:

Reprinted from J. Appl. Phys. **106**, 064915 (2009), *The influence of substrate temperature and Al mobility on the microstructural evolution of magnetron sputtered ternary Ti-Al-N thin films*, M. Beckers, C. Höglund, C. Baetz, R. M. S. Martins, P. O. Å. Persson, L. Hultman, and W. Möller, with kind permission from the American Institute of Physics.

FIGURES ADDED INTO CHAPTER 1 - 6:

Figure 5 and *Figure 6* are redrawn with kind permission from Prof. S. Limpijumnong and the American Physical Society.

Figure 29 is redrawn with permission from the American Institute of Physics.

The following figures are redrawn from my Licentiate Thesis (No. 1344, Linköping Studies in Science and Technology): *Figure 13*, *Figure 14*, *Figure 15*, *Figure 16*, *Figure 21*, *Figure 22*, *Figure 23*, *Figure 24*, *Figure 26*, *Figure 27*, *Figure 30*, and *Figure 31*.

TABLE OF CONTENTS

1. Introduction	1
1.1 Background	1
1.2 Research objective	1
1.3 Outline of the Thesis	2
2. Transition metal nitrides	5
2.1 The Sc-Al-N system	5
2.1.1 Scandium	5
2.1.2 Aluminum	6
2.1.3 Nitrogen	6
2.1.4 ScN	7
2.1.5 AlN	8
2.1.6 Sc-Al-N	9
2.2 The Ti-Al-N system	11
2.2.1 Titanium	11
2.2.2 TiN	12
2.2.3 Ti-Al-N	12
2.3 Binary phases	13
2.3.1 Rocksalt structure	14
2.3.2 Wurtzite structure	14
2.3.3 Hexagonal structure of ScN	16
2.4 Ternary phases	17
2.4.1 MAX phases	18
2.4.2 Perovskite phases	19
2.4.3 Pseudobinary phases	20
3. Theoretical modeling	23
3.1 Density functional theory	23
3.2 Ternary phase diagrams from first principles	25
3.2.1 Ti-Al-N system	26
3.2.2 Sc-Al-N system	28
3.3 Lattice parameter calculations	28
3.4 Mixing enthalpies of competing crystal structures	30
4. Phase formation and transformation	33
4.1 Crystallography	33

4.1.1	<i>Miller (3-) and Miller-Bravais (4-) indices</i>	34
4.1.2	<i>Diffraction patterns and pole figures</i>	36
4.2	<i>Epitaxy</i>	37
4.2.1	<i>Epitaxial growth</i>	37
4.2.2	<i>Lattice match</i>	38
4.3	<i>The substrate and role of seed layers</i>	40
4.4	<i>Phase transformation</i>	42
4.4.1	<i>Spinodal decomposition</i>	42
4.4.2	<i>Topotaxial phase formation</i>	43
5.	<i>Thin film deposition and growth</i> _____	49
5.1	<i>DC magnetron sputtering</i>	49
5.1.1	<i>Vacuum conditions</i>	49
5.1.2	<i>The magnetron sputtering process</i>	50
5.1.3	<i>Reactive magnetron sputtering</i>	52
5.1.4	<i>Magnetron sputter epitaxy</i>	53
5.2	<i>Nucleation and growth</i>	54
5.3	<i>The deposition systems</i>	55
5.3.1	<i>Magnetron sputter epitaxy in Ragnarök</i>	56
5.3.2	<i>In situ X-ray diffraction at the ESRF</i>	57
6.	<i>Analysis techniques for thin films</i> _____	59
6.1	<i>Ion beam analysis techniques</i>	59
6.1.1	<i>Ion-solid interactions</i>	60
6.1.2	<i>Rutherford backscattering spectroscopy</i>	62
6.1.3	<i>Channeling RBS</i>	65
6.1.4	<i>Elastic recoil detection analysis</i>	65
6.2	<i>X-ray diffraction</i>	67
6.2.1	<i>X-ray diffraction</i>	69
6.2.2	<i>Pole figures</i>	69
6.2.3	<i>X-ray reflectivity</i>	70
6.3	<i>Transmission electron microscopy</i>	72
6.3.1	<i>High-resolution transmission electron microscopy</i>	73
6.3.2	<i>Scanning transmission electron microscopy</i>	74
6.3.3	<i>Energy dispersive X-ray spectroscopy</i>	74
6.3.4	<i>Electron diffraction</i>	75
6.3.5	<i>Sample preparation</i>	75
6.4	<i>Electrical characterization</i>	75
6.4.1	<i>Van der Pauw resistivity measurements</i>	76
6.5	<i>Mechanical characterization</i>	77
6.5.1	<i>Nanoindentation</i>	77

7. Summary of results	79
7.1 The Sc-Al-N system	79
7.1.1 <i>The inverse perovskite Sc₃AlN</i>	79
7.1.2 <i>The cubic Sc_{1-x}Al_xN solid solution</i>	80
7.1.3 <i>The wurtzite Sc_{1-x}Al_xN solid solution</i>	82
7.2 The Ti-Al-N system	83
7.2.1 <i>New routes for Ti₂AlN MAX phase formation</i>	83
7.2.2 <i>Ti₄AlN₃ thin film growth attempts</i>	84
8. Contributions to the field	87
9. References	89
10. The Papers	99
Paper 1	101
Paper 2	107
Paper 3	117
Paper 4	131
Paper 5	145
Paper 6	151
Paper 7	163

1.

INTRODUCTION

1.1 BACKGROUND

Thin film technology is a rapidly growing research field where the number of applications increases every day. Films are used as protective coatings on tools, as decorative coatings found everywhere around us, as UV-light protections on windows, as diffusion barriers and connectors for all types of micro components in the electronics industry, etc.

The Thin Film Physics Division at Linköping University has a long tradition of depositing and characterizing epitaxial, single-crystal binary nitrides, especially TiN and AlN. The films are grown by reactive magnetron sputtering, often using X-rays to follow growth and phase transformations *in situ*. Nitrides are compounds belonging to the class of ceramics, meaning that they usually are insulating or semiconducting with properties like high melting point, high hardness, and oxidation resistance.

It has become clear that it is possible to design multifunctional coatings, which means that one coating fulfills several demands, but also that there can be one type of coating for each application. Simple binary phases are not enough and recent research has therefore focused on ternary and multinary coatings. Since the early 90s the Thin Film Physics Division has systematically explored the Ti-Al-N system as one of the first ternary nitride systems, using the knowledge about the binaries. Initially, the cubic solid solution of $Ti_{1-x}Al_xN$ was studied and more recently, the interest turned to the so called $M_{n+1}AX_n$ phases including Ti_2AlN and attempts to grow Ti_4AlN_3 .

The ScN system is much less explored. D. Gall, at that time at the University of Illinois, Urbana, together with co-workers from Linköping in the late nineties published a few papers about epitaxial magnetron sputtered ScN. Until the work in this Thesis started, there was essentially nothing more on the experimental side published. Now we see an increased interest in the solid solutions of Sc-A-N, where A is Al, Ga or In, mainly intended for optical and electrical applications.

1.2 RESEARCH OBJECTIVE

The aim of the present work is to further the basic understanding of epitaxial nitride thin film growth and phase evolution during reactive magnetron sputtering. Sc-Al-N and

Ti-Al-N have been employed as model systems. The Sc-Al-N system was essentially unexplored when this work started and there has been room for discoveries, attempts to understand the observed behaviors, and possibilities to identify differences with the Ti-Al-N system. The Ti-Al-N system has been addressed to resolve some outstanding topics on new ways for $M_{n+1}AX_n$ phase formation, but also for understanding the reasons why some phases can not easily be formed.

I wanted to replace Ti in relatively well-known Ti-Al-N alloys by another element. The transition metal Sc (next to Ti in the periodic table) was chosen, partly due to its interesting properties as an alloying element to Al,¹ and partly due to previous work on ScN/CrN superlattices for use in X-ray mirrors.² *Paper 1* reports on successful epitaxial growth of single-phase Sc_3AlN together with theoretical calculations showing that this phase is thermodynamically stable. In *Paper 2* the cubic solid solution $Sc_{1-x}Al_xN$ is shown to exist for $0 \leq x \leq 0.6$, while *Paper 3* theoretically claims and experimentally shows that this phase does not undergo spinodal decomposition, as is the case for $Ti_{1-x}Al_xN$. *Paper 4* explores the solubility of ScN in wurtzite-structure AlN.

The thin film growth of MAX phase structure Ti_2AlN , sometimes with inclusions of perovskite structure Ti_3AlN , is reported in References 3, 4, and 5. When further exploring the Ti-Al-N system I set out to lower the deposition temperature of Ti_2AlN , which was 675 °C at that time for parallel basal plane growth.⁶ In *Paper 5* a new way of depositing Ti_2AlN by solid state reaction in AlN/Ti multilayer thin films is developed, reducing the deposition temperature to 500 °C. Al_2O_3 is often referred to as a very temperature stable substrate material, but in *Paper 6* it is shown that TiN_x deposited onto Al_2O_3 at 800 °C forms Ti_2AlN through a solid state reaction between substrate and film. The attempt to grow thin films of Ti_4AlN_3 , a phase in the Ti-Al-N system that has been obtained through bulk synthesis, however, proves to be problematic, as reported in *Paper 7*.

1.3 OUTLINE OF THE THESIS

This Thesis starts with a presentation of the binary and ternary phases in this work, followed by a mainly experimental description of the components in the Ti-Al-N and Sc-Al-N systems. Then, a chapter is dedicated to theoretical studies that are relevant for this work, including comparisons between different Ti-Al-N and Sc-Al-N materials regarding phase stability, mixing enthalpies, and lattice parameters. After that, a chapter covers phase formation and phase transformation seen from an experimentalist's point of view. It briefly explains some important crystallographic terms, what is meant by epitaxy, and why the

choice of substrate and seed layer plays a paramount role. Some relevant phase transformation mechanisms are also described. Thereafter, the experimental part about thin film deposition and growth follows, explaining what is meant by reactive magnetron sputter epitaxy, nucleation and growth, and describing the deposition systems that were used. The films are characterized with ion beam analysis, X-ray diffraction, electron microscopy, as well as resistivity and hardness measurements. A large part of this Thesis is devoted to describing these techniques. After that, the seven included papers are summarized followed by a statement on the author's contribution to the field.

2. TRANSITION METAL NITRIDES

The papers included in this Thesis study compounds in the Sc-Al-N and Ti-Al-N systems. In this chapter I present the most relevant materials, including some properties and other useful information. I have put most focus on the ternary Sc-Al-N system, due to its novelty, and since I have contributed to the majority of the published work in this system.

2.1 THE Sc-Al-N SYSTEM

2.1.1 SCANDIUM

Scandium (Sc) is a transition metal* with element number 21 in the periodic table, next to titanium. It was discovered by Lars Fredrick Nilson from Sweden in 1876 in the minerals euxenite and gadolinite.⁷ Sc has a relative atomic mass of 44.9559, a density of 2.985 g/cm³ and a melting point of 1541 °C. The crystal structure of Sc is hexagonal close packed, with lattice parameters $a = 3.31 \text{ \AA}$ and $c = 5.27 \text{ \AA}$.⁸

Scandium is the 23rd most occurring element in the sun and certain stars, while on earth it is only the 50th most common element. Sc is never found as a free metal, but it is present in very small amounts in nearly a thousand different minerals. The world production of Sc is on the order of 2000 kg per year as scandium oxide. The production of metallic Sc is in the order of 10 kg per year, out of which I have used ~0.25%. The oxide is converted to scandium fluoride and reduced with metallic calcium.⁷

Sc is mostly used as an alloying element in Al, and it provides the highest increase in strength per atomic percent of added alloying element in Al.⁹ Sc acts as a grain refiner, and the fine, coherent Al₃Sc precipitates that form during annealing reduce recrystallization of the material.¹⁰ When Al is alloyed with 0.1 - 0.5% Sc, its hardness increases and the material becomes more suitable for high temperature applications.¹ Sc is mainly used in alloys where the materials cost is a minor issue, and where there is a demand for a good weldability in combination with a high materials strength.^{9,10,11} Sports equipment with

* Sc was historically considered to be a rare earth metal, since it often occurs in the same ore deposits as Y and the lanthanides and shows similar chemical properties. Following the IUPAC definition of a transition metal being "an element whose atom has an incomplete *d* sub-shell, or which can give rise to cations with an incomplete *d* sub-shell",¹² it is also correct to consider Sc a transition metal.

high demands on reliable performance, like bicycles and baseball bats, are frequently manufactured from Sc containing Al alloys. In the former USSR, the development of Sc-Al-alloys began in the 1980s and they were originally used for military applications in, e.g., the MIG-29 fighter aircraft.⁹

High cost (Sc metal with a purity of 99.99% and a lot size of 1000 g costs 5.42 US\$ per 1 g as of 2010-03-23)¹³ has precluded widespread application of Sc-containing alloys. As long as there is no demand for Sc, there is no motivation for a larger production. With an increased demand, followed by a more large scale mining, the price could go down. Therefore, the introduction of functional Sc-based nitrides may further promote the interest in the metal.

2.1.2 ALUMINUM

Aluminum (Al) is a metal with element number 13 in the periodic table. Al salts were used already by the ancient Greeks and Romans, but the first metal Al was produced in 1825.¹⁴ Al has a relative atomic mass of 26.9815, a density of 2.70 g/cm³ and a melting point of 660 °C.¹⁵ The crystal structure is face centered cubic, with lattice parameter $a = 4.05 \text{ \AA}$.⁸ Al is the third most abundant element in the earth crust after oxygen and silicon. It is mostly found as oxides or silicates due to its high affinity to oxygen. Almost all Al is produced from bauxite ($\text{AlO}_x(\text{OH})_{3-2x}$) and extracted through an energy-intensive smelting process. The largest producers of Al are China, Russia, and Canada. The world production of Al will soon reach 40 000 000 ton per year. Recycling Al requires only 5% of the energy needed to produce it from bauxite. Large quantities of Al are therefore recycled and nowadays 85% of the Al in construction materials and 95% of Al in vehicles are recycled.¹⁵

Aluminum has a remarkable ability to resist corrosion by forming a thin oxide layer on the surface. It is also known for its low density, which makes it highly attractive for aerospace, building, and transportation industries. The tensile strength of pure Al is relatively low, which is why most processed Al is alloyed with other elements, like Zn, Mg, Mn, Si or Sc.¹⁵

2.1.3 NITROGEN

Nitrogen (N), with element number 7, is a colorless gas that occurs as N₂. It is formally considered as discovered by Daniel Rutherford in 1772.¹⁶ The name stems from the Latin

word *nitrogenium*, where *nitrum* means saltpeter (a naturally occurring mineral source of nitrogen) and *genes* means “forming”, but it was for a long time also referred to as *azote* (“lifeless” gas) due to animals dying in it. In many languages nitrogen still has a name alluding to the danger of suffocation, like *azote* in French, *Stickstoff* in German and *kväve* in Swedish.¹⁷

N has a relative atomic mass of 14.007 and a boiling point of -195.79 °C. Nitrogen is the most abundant element in the Earth atmosphere (78%), but it is also present in all living organisms and in a number of minerals. In the atmosphere, most nitrogen is present in its molecular form, N₂, and relatively non-reactive.¹⁷ In this Thesis nitrogen is introduced as a reactive gas in the deposition process. In the high energy plasma, the N-N bonds are broken and N condensates on the substrate together with other sputtered elements, forming solid nitride films. Nitrogen is also used in its liquid form in cold traps to achieve better vacuum in deposition chambers and microscopes.

2.1.4 ScN

ScN is a rocksalt structure transition metal nitride with lattice parameter $a = 4.50 \text{ \AA}$.¹⁸ ScN shows typical nitride properties like high hardness (21 GPa)¹⁹ and high temperature stability with a melting temperature of 2600 °C.²⁰ Still quite unexplored, only about 50 papers have been published within the field. Many of these papers consist of theoretical calculations discussing whether ScN is a semimetal or a semiconductor. The most recent publications present the material as a semiconductor with a bandgap between 0.9 and 1.6 eV.^{21,22,23,24}

Already in early 1970's Dismukes and co-workers showed that ScN can be grown as a thin film using hydride vapor phase deposition,²⁵ later even epitaxially onto Al₂O₃(0001).^{26,27} In 1998 Gall *et al.* reported about polycrystalline ScN films grown via magnetron sputtering in pure N₂ atmosphere and under ultra high vacuum conditions. The film texture developed through a competitive growth mode, resulting in a complete 111 preferred orientation for thicknesses above 40 nm. The films showed semiconducting behavior.²⁸ Later, the same group showed that an increased energy of the N₂⁺ sputter gas yields single-crystal films.¹⁹ Significantly improved ScN film quality was achieved through molecular beam epitaxy onto MgO(001)²⁹ or Si(111) substrates, where the optimum growth temperature was identified to be 850 °C.³⁰

In addition, my co-workers in the Thin Film Physics Division have shown that ScN/CrN superlattices are very well suited for use in X-ray mirrors in extreme environments.² The films show similar reflectance as state-of-the-art Cr/Sc multilayers and, additionally, have a thermal stability up to 850 °C and a mechanical hardness of 19 GPa.² ScN is shown to act as a diffusion barrier against N loss from CrN at elevated temperatures.²

ScN is used as a seed layer in *Paper 1*, *Paper 2*, and *Paper 3* for growth of epitaxial cubic Sc-Al-N films. In all cases MgO(111) or Al₂O₃(0001) substrates were used, resulting in ScN(111) layers. The substrate bias has been floating, so with the employed growth conditions, the hexagonal template from the substrate is enough for single-crystal growth.

Moram *et al.* showed that ScN has a higher affinity to oxygen than TiN and ZrN when deposited under similar conditions.³¹ Similar observations are made in *Paper 2*, where Sc_{1-x}Al_xN films are deposited onto ScN seed layers. The samples with the lowest Al contents ($0 \leq x \leq 0.14$) have up to 10 at.% O incorporated. The higher the Al-content in the film is, the lower is the oxygen content.

First-principles calculations report about a metastable layered hexagonal structure of ScN.³² This structure is interesting because hexagonal ScN could form an alloy with wurtzite semiconducting AlN, InN or GaN, leading to materials with a wide range of band gaps.³² Even hexagonal superlattices consisting of GaN/ScN or InN/ScN, which would combine four and fivefold coordination, are expected to affect the piezoelectric response, electronic band gap, and phonon spectra.³³ Up until and during the work leading to this Thesis, the hexagonal structure of ScN has never been observed.

2.1.5 AlN

AlN is an extensively studied semiconductor, mainly used in optical and electronic device applications. The material has a wide energy band gap (6.2 eV),³⁴ high hardness (>20 GPa),^{35,36} high thermal conductivity (3.19 W/cmK at RT),³⁷ and high-temperature stability (melting point >2000 °C).³⁸ In this Thesis, AlN is used as a seed layer for growing high quality wurtzite-structure Sc_{1-x}Al_xN in *Paper 4* or as an epitaxial precursor to form Ti₃AlN and Ti₂AlN through a solid state reaction with Ti.

The thermodynamically stable structure of AlN is wurtzite, but it has also been shown that AlN has a metastable cubic structure at high enough pressures and temperatures. Epitaxial cubic AlN can be deposited by pulsed laser ablation³⁹ and is observed as an intermediate product during spinodal decomposition of Ti_{1-x}Al_xN.^{40,41,42} In *Paper 3* I compare the phase

separation mechanisms for $\text{Ti}_{1-x}\text{Al}_x\text{N}$ and $\text{Sc}_{1-x}\text{Al}_x\text{N}$ and explain why $\text{Sc}_{1-x}\text{Al}_x\text{N}$ does not decompose isostructurally, i.e. leading to c-AlN, as is the case for $\text{Ti}_{1-x}\text{Al}_x\text{N}$.

2.1.6 Sc-Al-N

The ternary Sc-Al-N system is still a relatively unexplored material. The ternary phase diagram is given in Figure 1, showing the known intermetallic binary phases Al_3Sc , Al_2Sc , AlSc , AlSc_2 , as well as the above mentioned nitrides ScN and AlN .⁴³

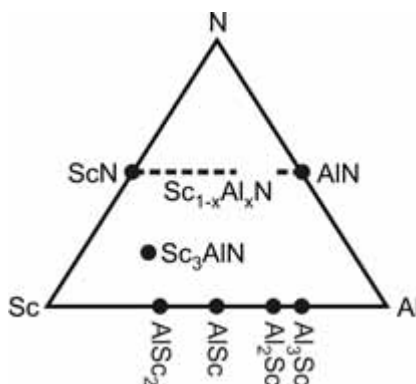


Figure 1: The ternary phase diagram of the Sc-Al-N system.

The only reported ternary compound is the inverse perovskite Sc_3AlN , reported in Reference 44 and in *Paper 1*. It has a hardness of 14.2 GPa, an elastic modulus of 249 GPa, and an electrical resistivity of 41.2 $\mu\Omega\text{cm}$. Bulk-sensitive soft-X-ray emission spectroscopy was performed by Magnuson *et al.* and compared with first principles calculations, to investigate the electronic structure and chemical bonding of Sc_3AlN . The main bonding is found to be Sc 3d – N 2p at -4 eV below the Fermi level, while Al 3p – Sc 3d shows a weaker covalent bonding at -1.4 eV below the Fermi level.⁴⁵ The mechanical and thermodynamic stability of Sc_3AlN was studied with first principles calculations by Mikhaylushkin and co-workers.⁴⁶ Their results confirm the stability of Sc_3AlN , but also propose phonon softening as a possible reason for the experimentally observed nonperiodic stacking faults along the $\langle 111 \rangle$ growth direction of Sc_3AlN in *Paper 1*. Defect-free crystals are suggested to exhibit anomalous carrier properties.⁴⁶ Mattesini *et al.* performed a first principles study of the elastic properties and electrostructural correlations in Sc_3EN , with

$E = \text{Al, Ga, In}$. Sc_3AlN is shown to have the most metallic like conductivity, but the Sc-N bonding is less covalent than in Sc_3InN and Sc_3GaN , leading to the lowest Young, shear and bulk moduli among the three compounds.⁴⁷

From *Paper 2*, a maximum solubility of ~60% was observed for AlN in cubic ScN(111) films grown by reactive magnetron sputtering. Higher AlN contents result in phase separation into wurtzite-structure AlN or AlN-rich wurtzite $\text{Sc}_{1-x}\text{Al}_x\text{N}$, occurring in up to four epitaxial relationships to the seed layer. Alling *et al.* have calculated the lattice parameters, electronic densities of states, and mixing enthalpies of cubic $\text{Ti}_{1-x}\text{Al}_x\text{N}$ and $\text{Sc}_{1-x}\text{Al}_x\text{N}$. Electronic-structure effects in $\text{Ti}_{1-x}\text{Al}_x\text{N}$ lead to a strongly asymmetric contribution to the mixing enthalpy, resulting in an increased driving force for decomposition at high AlN concentrations. In $\text{Sc}_{1-x}\text{Al}_x\text{N}$, however, the large lattice mismatch yields a symmetric contribution to the mixing enthalpy, which hinders isostructural decomposition.⁴⁸ In *Paper 3*, annealing studies of cubic $\text{Sc}_{1-x}\text{Al}_x\text{N}$ and $\text{Ti}_{1-x}\text{Al}_x\text{N}$, with $x \approx 0.5$, show that $\text{Sc}_{1-x}\text{Al}_x\text{N}$ separates into cubic ScN and wurtzite AlN at 1100 °C via nucleation and growth at grain boundaries, while $\text{Ti}_{1-x}\text{Al}_x\text{N}$ phase separates isostructurally via coherent spinodal decomposition.

Akiyama *et al.* have reported that wurtzite $\text{Sc}_{1-x}\text{Al}_x\text{N}$ has the highest piezoelectric response among tetrahedrally bonded semiconductors. Due to its high-temperature stability, this material is promising for high-temperature piezoelectric devices.⁴⁹ Textured $\text{Sc}_{1-x}\text{Al}_x\text{N}$ thin films, with $0.54 \leq x \leq 1$, were deposited by reactive rf dual-magnetron sputtering onto Si(001) substrates.⁴⁹ The results show that the piezoelectricity of $\text{Sc}_{1-x}\text{Al}_x\text{N}$ improves with increasing Sc content, but also that it has a strong dependence on growth temperature. Lower temperatures yielded better crystalline quality, which is considered necessary for a high piezoelectric response.⁵⁰ For films grown at 400 °C and $x = 0.57$, the piezoelectric coefficient d_{33} is measured to be 27.6 pC/N.⁵⁰ First-principles calculations by Tasnádi *et al.* in Reference 51 show that the hexagonal structure of ScN plays a role on the enhanced piezoelectricity for $x \approx 0.5$ in $\text{Sc}_{1-x}\text{Al}_x\text{N}$ alloys. One key explanation for the high piezoelectricity is on the cover of this Thesis. It shows an energy landscape for $\text{Sc}_{0.5}\text{Al}_{0.5}\text{N}$ with the c/a ratio versus volume. The global minimum on the front page corresponds to the wurtzite structure, while the almost degenerate hexagonal structure is seen as an energy plateau on the backside. The shallow region between these structures enables elastic softening, which leads to sensitivity for internal strain and a large piezoelectric effect. *Paper 4* shows that up to ~22% ScN can be dissolved into AlN(0001), while retaining a single-crystal wurtzite structure, when using reactive magnetron sputtering under conditions optimal for high quality w-AlN growth. The lattice parameters and mixing enthalpies of the solid solution, from first principles calculations, agree with the

experimental results. These results also raise questions regarding the phase purity of the samples studied in References 49 and 50.

Finally, there are a few publications dealing with what could be called doping of wurtzite AlN with ScN. Bohnen *et al.* report about $\text{Sc}_{0.05}\text{Al}_{0.95}\text{N}(0001)$ nanowires, for which cathodoluminescence studies show a sharp emission near 2.4 eV. Therefore, wurtzite $\text{Sc}_{1-x}\text{Al}_x\text{N}$, with x close to 0, is presented as an alternative to $\text{In}_{1-x}\text{Al}_x\text{N}$ for optoelectronic applications operating in the 200-550 nm range.⁵² Lei and co-workers have fabricated Sc-doped AlN sixfold-symmetrical hierarchical nanostructures, which at room temperature show ferromagnetic behavior, showing that Sc is a potential nonmagnetic dopant that could be used in nanostructures of dilute magnetic semiconductors.⁵³

2.2 THE Ti-Al-N SYSTEM

2.2.1 TITANIUM

Titanium (Ti) is a transition metal with element number 22 in the periodic table. It was discovered by William Gregor in 1791 and named for the Titans, which were a race of powerful deities said to have ruled during the Golden Age of Greek mythology.^{54,55} Ti has a relative atomic mass of 44.867, a density of 4.506 g/cm³ and a melting point of 1673 °C. The crystal structure of Ti is hexagonal close packed, with lattice parameters $a = 2.95 \text{ \AA}$ and $c = 4.68 \text{ \AA}$.⁸ Titanium is the ninth most abundant element in the earth crust. Ti is found in most igneous rocks and in sediments derived from them. The largest deposits of Ti are found in Australia, South Africa, and Canada. The world production of Ti is on the order of 90 000 ton per year and total reserves of Ti are estimated to exceed 600 000 000 ton.⁵⁴

Ti is recognized for its high strength-to-weight ratio. The metal is sometimes called the “space age metal”, due to its low density, high strength, high corrosion resistance, and its shiny silver color. It is used in a wide range of applications (both pure or with alloying elements added) within aerospace, military or automotive industry, but there are also a large number of medical applications or high-end products for the consumer market that contain Ti.⁵⁴

2.2.2 TiN

TiN is the most investigated transition metal nitride. It has been used for over 40 years as a coating on cutting tools, enabling machining of harder materials at higher cutting speeds. TiN is also used as a diffusion barrier,^{56, 57} for corrosion protection,⁵⁸ and as a decorative coating due to its shiny, golden color.⁵⁹ The drawback with TiN coatings is that they start oxidizing at 550 °C, which limits the usability at elevated temperatures.^{60, 61} For elevated temperature applications, TiN is often replaced by $Ti_{1-x}Al_xN$, which at high enough temperatures phase separates via spinodal decomposition into isostructural TiN and AlN, yielding increased hardness.

2.2.3 Ti-Al-N

The Ti-Al-N system is quite well explored and a ternary phase diagram for Ti-Al-N is given in Figure 2. The known binary phases are Ti_3Al , TiAl, TiAl₂, TiAl₃, and the nitrides Ti_2N , TiN and AlN.⁴³ The ternary phases Ti_2AlN ,⁶² Ti_3AlN ,⁶³ and Ti_4AlN_3 ⁶⁴ are all reported to exist together with a solid solution between TiN and AlN yielding $Ti_{1-x}Al_xN$ (with $0 \leq x \leq 0.67$).⁴² Ti_3AlN_2 does not exist in bulk form, but is predicted theoretically as a metastable phase.⁶⁵

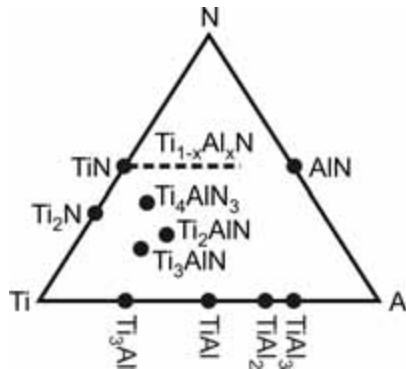


Figure 2: The ternary phase diagram of the Ti-Al-N system, partly redrawn from Reference 66.

Ti_3AlN is in this Thesis only seen in *Paper 5* as an intermediate phase during annealing of AlN and Ti multilayers to form Ti_2AlN . Ti_2AlN still remains the only nitride $M_{n+1}AX_n$

phase, to have been synthesized as a thin film, using reactive sputtering from either a compound 2Ti:Al target³ or elemental Ti and Al targets.⁴ It has been shown that the microstructure of Ti₂AlN is determined by the substrate temperature. Parallel basal plane growth requires temperatures of at least 675 °C,⁶ while lower values induce growth with the *c*-axis tilted 60° away from the substrate normal, accompanied by surface roughening.⁴ *Paper 5* presents a new way to decrease the synthesis temperature of Ti₂AlN, namely by depositing layers of AlN and Ti and annealing them afterwards to induce a solid state reaction. *Paper 6* shows that Ti₂AlN also can be synthesized through a solid state reaction between film and substrate when depositing understoichiometric TiN_x onto a single-crystal Al₂O₃ substrate at sufficiently high temperatures. *Paper 7* explores the possibility of synthesizing the related second M_{n+1}AX_n phase nitride Ti₄AlN₃ as a thin film.

The solid solution of TiN and AlN in Ti_{1-x}Al_xN is widely used to increase the lifetime and cutting speed of coated tools.^{67,68} It is often used as a replacement for TiN due to the better oxidation resistance,⁶⁹ which originates from the Al-rich oxide layer that forms on the film surface. Another advantage with Ti_{1-x}Al_xN compared to TiN is the improved cutting performance due to age hardening of the material at high temperatures, caused by phase transformation into TiN and rocksalt AlN via spinodal decomposition.⁴⁰

2.3 BINARY PHASES

Transition metal compounds with nitrogen form close-packed or nearly closed-packed structures, where the non-metal atoms are inserted into interstitial sites of the metal lattice.⁷⁰ The metallic structures can for example be face center cubic (fcc), body center cubic (bcc), hexagonal close packed (hcp), or simple hexagonal. In 1931, Hägg formulated a few empirical rules for crystal structures of transition metal nitrides and carbides. One rule says that the structure is determined by the ratio between the radius of the non-metal r_X and the radius of the transition metal r_{Me} according to

$$r = \frac{r_X}{r_{Me}}. \quad (2.1)$$

If r is smaller than 0.59 the metal sublattice is expected to be simple (fcc, bcc, hcp, or simple hexagonal), while compounds with larger r values have a more complex metal sublattice.⁷⁰ Both ScN and TiN fulfill the rule, because they have an fcc metal sublattice and a radii ratio of 0.34 and 0.38, respectively.

2.3.1 ROCKSALT STRUCTURE

Many transition metal nitrides, with a 1:1 metal-to-nitrogen ratio, crystallize in the rocksalt (c or B1) structure. The structure is shown in Figure 3(a) and can be described by an fcc Bravais lattice with a basis consisting of two atoms (nitrogen and metal) sitting at [000] and [0.5 0.5 0.5]. Each atom is octahedrally coordinated to six neighbors of the other element.

Thermodynamically stable rocksalt structure binaries mentioned in this Thesis are TiN and ScN. In *Paper 3* the metastable rocksalt structure of AlN forms during annealing of $Ti_{1-x}Al_xN$, before it transforms to the thermodynamically stable wurtzite structure.

When looking at the (111)-planes, shown in Figure 3(b), the cubic structure is comparable with the (0001)-surface of a hexagonal structure. The atoms indexed with A, B, and C are positioned in the three uppermost monolayers, respectively. All films in this Thesis are grown epitaxially (defined below), meaning that the crystalline structure and orientation of the underlying template is of great importance. In all experiments some kind of a hexagonal structure is (or could possibly be) seen. Therefore, all depositions of rocksalt structure phases are performed either on a (111)-surface of a cubic structure, or on the (0001)-surface of a hexagonal structure.

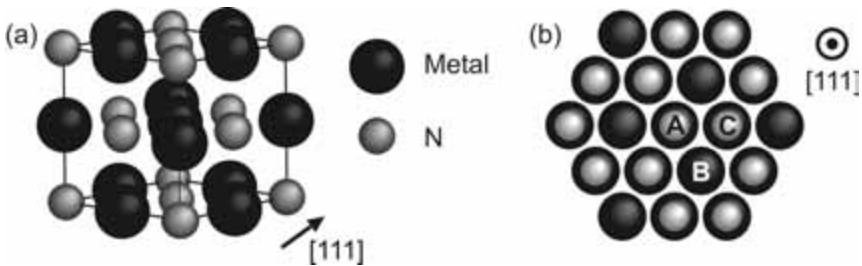


Figure 3: The unit cell of a rocksalt structure is shown in (a) and the (111)-surface of the same structure is shown in (b).

2.3.2 WURTZITE STRUCTURE

Several binary nitrides crystallize in the wurtzite (w or B4) crystal structure, which is a hexagonal structure named after the mineral with the same structure, (Zn,Fe)S. The mineral Wurtzite was in turn named after the French chemist Charles Adolphe Wurtz in 1861.⁷¹ Like in the rocksalt structure, the metal-to-nitrogen ratio has to be one. Characteristic for a

wurtzite structure is that it is non-centrosymmetric and has a tetragonal coordination, meaning that every atom has four nearest neighbours with equal bond lengths. The wurtzite structure is shown in the left part of Figure 5. When it is a nitride phase it can be described as two hexagonal close packed lattices, one containing metal atoms and one containing nitrogen atoms. The relative displacement between both sublattices is $u \cdot c$, where u is the *internal parameter* of the structure. Ideally, wurtzite structures have a c/a ratio of $\sqrt{8/3}$ and a u -parameter of $3/8$. The nitrogen atoms are placed so that they occupy half of the available tetrahedral sites in the lattice of metal atoms.⁷²

AlN is the only wurtzite structure binary phase in this Thesis. Though, as mentioned before, AlN can under certain conditions also crystallize in the rocksalt structure. For a material that can crystallize in both the rocksalt and wurtzite structures (so called *polytypes*), it is important to be able to determine its structure. Even though the (111)-planes of a rocksalt crystal have a hexagonal surface, there is a clear difference between the stacking of atomic layers in a rocksalt structure in comparison to a wurtzite structure. This is illustrated in Figure 4, where AlN is taken as an example. In all drawings, the $\langle 0001 \rangle$ growth direction for a wurtzite structure (or $\langle 111 \rangle$ for the cubic structure) points upwards.

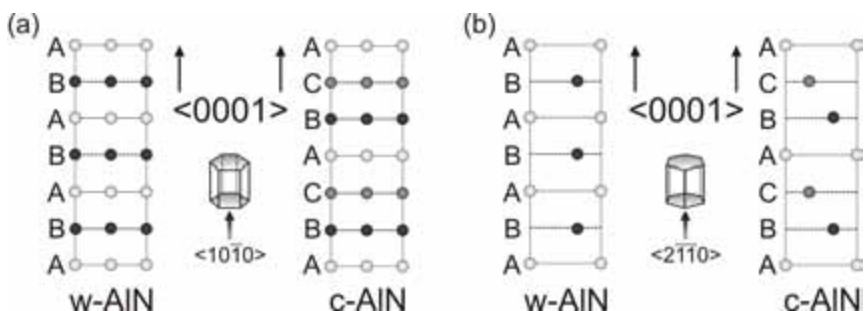


Figure 4: Schematic drawing of the stacking of wurtzite (ABAB) and rocksalt (ABCA) structure AlN, with the $\langle 0001 \rangle$ direction pointing up, and seen along the wurtzite (a) $\langle 10\bar{1}0 \rangle$ and (b) $\langle 2\bar{1}\bar{1}0 \rangle$ zone axes, respectively.

In Figure 4(a) the structure is seen along the $\langle 10\bar{1}0 \rangle$ zone axis. Along this projection it can not be distinguished between the ABAB-stacking of the wurtzite structure and the ABCA stacking of a cubic structure. In Figure 4(b), along the $\langle 2\bar{1}\bar{1}0 \rangle$ zone axis, a clear dissimilarity between the two stacking sequences is seen. This difference is also seen in diffraction patterns in transmission electron microscope or in X-ray diffraction

measurements. This example, however, does not take into account that the crystal structures in most cases can be distinguished due to different lattice constants. When working with epitaxial and crystalline samples, where the structure might be unknown, knowledge of the stacking sequence is a tool for solving a structural problem.

2.3.3 HEXAGONAL STRUCTURE OF ScN

In 2002, Farrer *et al.* predicted that ScN could be stabilized in a metastable hexagonal (h) structure.³² It is described as a layered hexagonal structure, which is nearly five-fold coordinated. The structure appears as an intermediate step during transformation from wurtzite to rocksalt structures. The same structure is also predicted to be metastable in MgO.⁷³

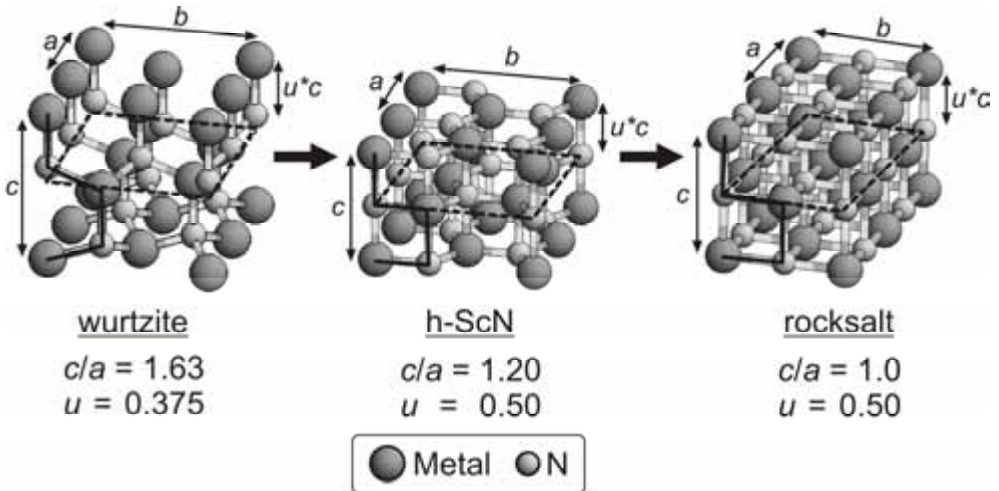


Figure 5: Two-step structural transformation from wurtzite to layered hexagonal to rocksalt. Redrawn from Reference 73.

In Figure 5 it is illustrated how a wurtzite structure could transform into a rocksalt structure, via the layered hexagonal structure. When the wurtzite structure is compressed, the c/a ratio decreases. For a c/a ratio of 1.20 and a u parameter of 0.5, an additional mirror plane appears at $0.5 \cdot c$ and the layered hexagonal structure is obtained. Each layer has a

hexagonal structure, with alternating metal and nitrogen atoms in the corners of the hexagon, as seen in the top view of the structure in Figure 6(a).⁷³

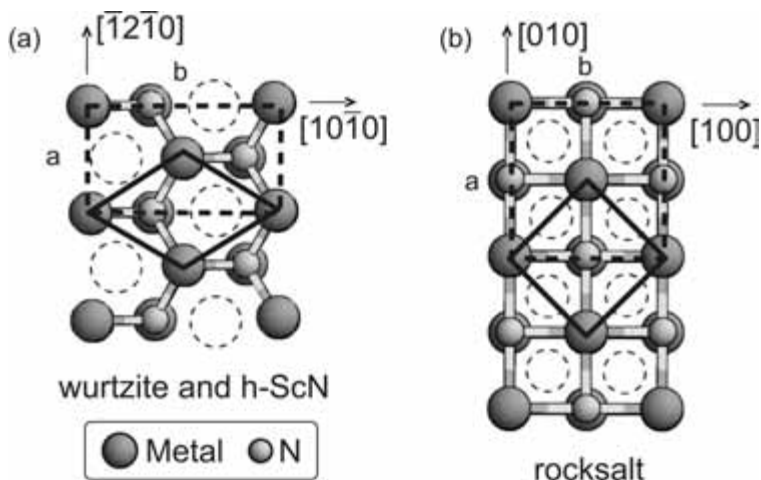


Figure 6: Top views of (a) wurtzite and hexagonal crystal structures and (b) rocksalt crystal structures. Redrawn from Reference 73.

The second transformation, from hexagonal to rocksalt structures, is illustrated in the right part of Figure 5 and is more easily seen in the top view in Figure 6. Compression along the $\langle 10\bar{1}0 \rangle$ direction changes the rhombic unit cell of a hexagonal plane into a square, while the nitrogen atom moves to the center, resulting in a rocksalt structure when all lattice parameters reveal $a = b = c$ and $u = 0.5$.⁷³

2.4 TERNARY PHASES

Already in the 1960s, Nowotny and co-workers put an effort into the synthesis of ternary transition metal phases and within a short period of time over 200 new carbides and nitrides were presented. Among them were several phases in which the metal sublattice was no longer close-packed or nearly close-packed, but the non-metal atoms occupied octahedral interstitial sites. The corresponding Nowotny octahedral phases have the general formula $Me_aM_bX_c$, where Me is a transition metal, M is a non-transition metal and X is a non-metal. They included more than 40 M_2AX phases (at that time known as *H*-phases), where A is an

A-group element. Among the discovered phases were also a few M_3AX_2 phases, and several (inverse) perovskites. Most of them were carbides.^{70,74} The nitrides remain less explored than the carbides, probably due to the higher difficulty to achieve stoichiometry.

This Thesis deals with ternary nitrides, especially $M_{n+1}AX_n$ phases, where $X = N$, and inverse perovskite phases. Metastable cubic and wurtzite structure pseudobinary alloys are also covered. Ternary crystal structures that are relevant for the Thesis are described below.

2.4.1 MAX PHASES

$M_{n+1}AX_n$ ($n = 1, 2, 3$) phases (MAX phases) consist of an early transition metal, M, an A-group element, A, and either carbon or nitrogen, X. The crystal structure is hexagonal and consists of twinned $M_{n+1}X_n$ blocks, with monolayers of A-elements in between. The thickness of the $M_{n+1}X_n$ blocks varies with n , yielding e. g., M_4AX_3 for $n = 3$.⁷⁵ The unit cells for M_2AX and M_4AX_3 are shown in Figure 7.

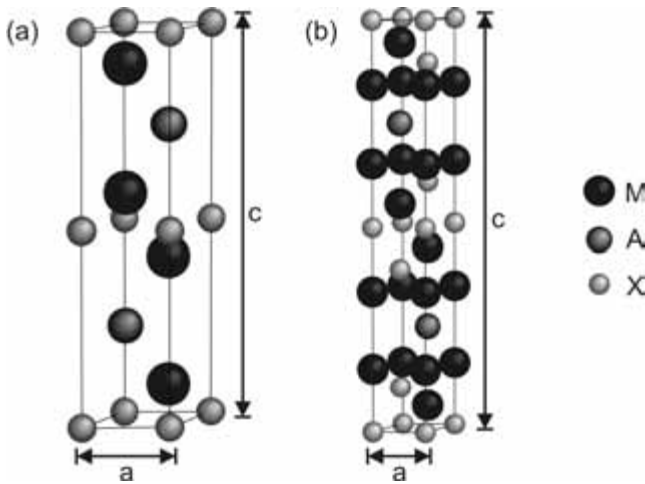


Figure 7: Unit cells of (a) M_2AX and (b) M_4AX_3 , consist of an early transition metal (M), an A-group element (A), and either C or N (X).

MAX phases have attracted considerable attention because they combine typical ceramic and metallic properties. Typical ceramic properties are high melting points and good

thermal stability, which for MAX phases originate from the strong covalent-ionic M-X bonds. The M-A bonding on the other hand is metallic and yields properties such as good electrical and thermal conductivity. In addition, the material shows high ductility and ease of machinability due to the alternation of strong and weak bonds leading to kink and shear band formation during mechanical deformation.⁷⁵

The first magnetron sputter deposited thin film MAX phase was Ti_3SiC_2 in 2001, around 40 years after its discovery.^{76,77,78} Soon after, the first and up to now only reported nitride MAX phase deposited as a thin film was Ti_2AlN , epitaxially grown onto $\text{MgO}(111)$.³

2.4.2 PEROVSKITE PHASES

The perovskites were described by Gustav Rose already in 1839. The first crystals came from the Ural Mountains and were named after the minister of principalities A. von Perowski from Petersburg, who was very interested in mineralogy and donated parts of his large mineral collection for research. Perovskites, with the *Strukturbericht* designation E2₁, comprise a large family of ternary phases, where oxygen occupies octahedral interstitials of a body centered cubic metal lattice, forming a face centered sublattice, as seen in Figure 8(a).⁷⁹ Since the 1940s research progressed incredibly and the perovskites have shown to have many extreme properties. The discovery of ferroelectricity in barium titanate⁸⁰ was followed by a large family of ferroelectric and piezoelectric oxides. The first superconducting perovskite $\text{BaPb}_{0.8}\text{Bi}_{0.2}\text{O}_3$ with a transition temperature $T_C = 11$ K was discovered in 1974⁸¹ and nowadays there are perovskite-like phases with a T_C up to 156 K at high pressures, e.g. $\text{HgBa}_2\text{CaCu}_2\text{O}_{6+\delta}$.⁸² Another property found in the 1990s was the colossal magnetoresistance (CMR).⁸³

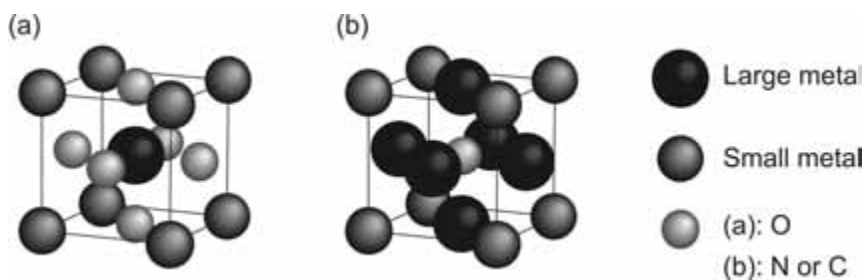


Figure 8: Unit cells of (a) a perovskite and (b) inverse perovskite.

The Sc_3AlN perovskite reported in *Paper 1* is of a type known as anti- or inverse perovskite, having a metallic face centered cubic structure with nitrogen atoms in body-centered position, see Figure 8(b). This type of perovskites was discovered much later than the oxide perovskites and is not as widely explored. They are interesting though, due to the possibility to design them as insulators, semiconductors, or conductors depending on their electronic nature.^{84,85} For some of the known perovskites (e.g. with Co or Ni), the radius ratio in Equation (2.1) is larger than 0.59 and it is therefore necessary to extend the Hägg rule to include these structures.⁷⁰

An inspiration to the work done in *Paper 1* is the existence of perovskite Sc_3AlN ,⁴⁴ Ti_3AlN ,⁶³ and Sc_3InN .⁸⁶ In Reference 44, J.C. Schuster *et al.* synthesized bulk Sc_3AlN by sintering cold-pressed molybdenum-foil wrapped mixtures of AlN with Sc at 1273 K. In this report the Sc_3AlN phase always co-existed with different binaries and the lattice parameter was measured to be somewhere between $a = 4.3496 - 4.435$ Å. *Paper 1* reports the first phase pure perovskite Sc_3AlN , and the first Sc_3AlN deposited as a thin film.

2.4.3 PSEUDO_BINARY PHASES

Pseudobinary structures are defined as solid solutions between two binary compounds (AC and BC), with one common element (C), forming $\text{A}_{1-x}\text{B}_x\text{C}$. In this Thesis, the C element is 50 at.% of the alloy, while x can be varied from 0 to 1. For a rocksalt crystal structure, the C atoms occupy one sublattice as in the binary case. The A and B atoms are usually randomly positioned within the second sublattice. Pseudobinaries can form in many different structures, like rocksalt, wurtzite, and zinc blende.

One advantage with pseudobinary alloys is that it is generally possible to tune their properties, by changing the ratio between the A and B elements. For semiconducting materials, the band gap can be tuned depending on application, with successful examples in $\text{Ga}_{1-x}\text{Al}_x\text{As}$ ⁸⁷ and $\text{Al}_{1-x}\text{In}_x\text{N}$.⁸⁸ In hard coatings for cutting tools the amount of B is chosen to match requirements regarding hardness, lifetime, and temperature stability.^{67,68,89} For growth of single-crystal thin films, it is often important to lattice-match epilayers, which means that the amount of element B is chosen to achieve the right lattice parameters. For the resulting lattice parameter, L. Vegard in 1921 came up with a simple rule. It says that the change in lattice parameter for a pseudobinary is linear between its binaries.⁹⁰ This can for most material systems be seen as a rule of thumb, but it has been proven that this rule can not be applied for all materials.⁹¹

In this Thesis the mutual solubility of AlN and ScN has been investigated. *Paper 2* and *Paper 3* deal with the cubic solid solution of $\text{Sc}_{1-x}\text{Al}_x\text{N}$, while *Paper 4* investigates the solubility of ScN in wurtzite AlN.

3. THEORETICAL MODELING

I appreciate the value in collaborating with people who use theoretical models as a tool for understanding my experimental results. After a short period of time I realized that exclusively experimental work cannot provide a satisfying understanding why some phases form and others do not. Experimentalists and theoreticians can learn a lot from each other, and a published research study is much stronger when based on independent experimental and theoretical work. I have not yet performed calculations myself, but I have taken an active part in the planning and discussions related to the calculations included in the papers.

Here, all calculations are based on first-principles techniques within the density functional theory formalism, which nowadays is the dominating method within materials modeling. In this chapter I explain some of the basic ideas behind the theory from an experimentalist's perspective. In the following paragraphs I describe calculation approaches of interest for my papers. These include how a ternary phase diagram can be determined by looking at competing phases, why lattice parameter calculations are important for experimental work, and finally spend a few words about mixing enthalpy calculations of competing crystal structures.

3.1 DENSITY FUNCTIONAL THEORY

Density functional theory (DFT) is based on quantum mechanics and considers the electronic structure of a material. In principle, the Schrödinger or the Dirac equation has to be solved. The atomic numbers of the included elements are the only necessary data input, and therefore DFT calculations are referred to as *ab initio* (meaning “from the beginning”) or first-principles calculations. Even though supercomputers are used for the computationally demanding calculations, only limited system sizes and time scales are possible to study.

The *Schrödinger equation* describes the non-relativistic motion of particles. For a many-body system, the wave function depends on the position in space of all n electrons, N nuclei, spins, and time. The Hamiltonian consists of the kinetic energies of the n electrons and N nuclei in the system, and the coulomb interactions between electron – nuclei, electrons – electrons and nuclei – nuclei. Due to the positional coupling of the three coulomb interactions it is impossible to solve the Hamiltonian for systems with more than a

few particles and therefore two clever simplifications and approximations are introduced. The *Born-Oppenheimer approximation* makes use of the condition that electrons have an extremely small mass in comparison to the nuclei. Therefore the nuclei are assumed to be stationary and only electrons are moving. *Bloch's theorem* utilizes the symmetry of a crystal leading to periodically repeated atomic positions. This implies that the problem has to be solved only for one unit cell, which for Sc_3AlN in *Paper 1* means for 5 atoms.

Despite the mentioned simplifications, the electron coupling term in the Hamiltonian still makes the calculations unmanageable for real-sized systems. To solve this, Hohenberg and Kohn came up with two fundamental theorems for DFT calculations. The first theorem says that for any system of interacting particles in an external potential, the full Hamiltonian is known if the ground state particle density is known. Following from this theorem, all ground state and excited state properties can also be determined. The second theorem says that there exists a general functional for the energy in any external potential, which has its ground state energy and ground state density at the global energy minima.⁹² Instead of having a wave function which depends on $3n$ variables, by introducing the electron density the number of variables is reduced to three.

The *Kohn-Sham equations* are a way of using the Hohenberg-Kohn theorems in practice, and they have turned out to be a great improvement from earlier DFT approaches.⁹³ The exchange-correlation energy (E_{xc}) term is the only term in these equations that can not exactly be calculated and includes the different explicit many-body quantum effects from the Schrödinger equation. Even though the contribution from the E_{xc} term is small as compared to e.g. the kinetic energy, it has to be approximated in a good way. Two approximations are mainly used, the *Local Density Approximation* (LDA) and the *Generalized Gradient Approximation* (GGA). In LDA the electron gas density is considered to be fully homogenous and can very accurately be calculated by quantum Monte Carlo simulations. Even though the charge density in general is far from homogenous, the assumption has for most cases shown to be correct when looking at a system average.⁹⁴ LDA has, however, shown to substantially underestimate volumes of 3d transition metals (e.g., Ti and Sc) and related alloys, because the electron density variation in these materials can not be neglected. To solve this, the reduced charge density around the electrons can manually be set, and for calculations in this Thesis this is done with the GGA functional by Perdew, Burke, and Enzerhof from 1996.⁹⁵ The GGA treats volumes of 3d transition metals in a more correct way and is therefore superior to LDA when calculating equilibrium volumes and lattice parameters, two of the most important output data for this work. In comparison to experiments, the GGA slightly overestimates lattice parameters, as for example can be seen in Figure 6 in *Paper 2*.

To solve the Kohn-Sham equations, the *projector augmented wave method* (PAW) is used. The electronic structure problem is solved numerically, using the periodicity of the lattice leading to periodic wave functions. Many plane waves are needed to treat the electron – nucleus interactions in core regions correctly. To reduce the computational costs arising from the large number of plane waves, a *frozen-core approximation* is introduced so that the properties of the core electrons have to be calculated only once. The approximation utilizes that core electrons are hardly affected by the chemical bonding and can be replaced by smooth wave functions from so called *pseudopotentials*.⁹⁶ The PAW method has been implemented in the *Vienna ab-initio simulation package* (VASP).^{97,98,99}

In a solid solution, like in *Paper 2*, *Paper 3*, and *Paper 4* it is important that the disordering of the atoms is treated stochastically, but still with the atoms connected to a fixed lattice. Atomic displacements due to, e.g., thermal vibrations are not taken into account (in this sense, all calculations are performed at 0 K), but would not change the results qualitatively. For the solid solutions in this work, the special quasi random structure (SQS) method, suggested by Zunger *et al.*¹⁰⁰ is used. It is based on a clever design of the atomic distribution in the lattice, which optimizes the short range pair interactions to mimic a real random situation, rather than random number generated supercells. The advantage is that rather reasonably sized supercells are enough to make the most important correlation functions to be random like. Yet for the SQS method, larger supercells would yield better accuracy, but the computational time sets the limit.

3.2 TERNARY PHASE DIAGRAMS FROM FIRST PRINCIPLES

For a ternary phase at a certain composition to be thermodynamically stable, it is required that its free energy is lower than that of each combination of ternaries, binaries or single elements with the same global composition, at a given temperature and pressure. A first approximation for the free energy can be given by the enthalpy, simply neglecting the effect of entropy. Thus, DFT enthalpy calculations can predict the stabilities of new phases. Obviously, a theory is not always representative for what can be done experimentally, but it can inspire the search for phases that might have been overlooked or can be thermodynamically metastable. Dahlqvist *et al.* have recently illustrated a systematic way to perform comparisons between competing multinary phases in terms of solving a linear optimization problem.¹⁰¹ The same approach is used in the following sections, which contain examples for how the Ti-Al-N and Sc-Al-N phase diagrams can be explored.

3.2.1 Ti-Al-N SYSTEM

Table 1 lists the known phases in the Ti-Al-N system and their ground state total energies E_0 .¹⁰² These energies are used in the following examples.

Table 1: Ground state total energies for known phases in the Ti-Al-N system, expressed in energy per formula unit.¹⁰²

Element	E_0 [eV]	Nitride	E_0 [eV]	Intermetallic	E_0 [eV]	Ternary	E_0 [eV]
Ti	-7.764	TiN	-19.449	Ti ₃ Al	-28.151	Ti ₂ AlN	-32.217
Al	-3.739	w-AlN	-14.890	TiAl	-12.309	Ti ₃ AlN	-40.017
N	-8.303	Ti ₂ N	-27.739	TiAl ₂	-16.538	Ti ₄ AlN ₃	-71.315
		c-AlN	-14.552	TiAl ₃	-20.560	Ti ₃ AlN ₂	-51.674

To illustrate a way of thinking when predicting a phase, the stability of Ti₂AlN is presented in a few steps. A large number of phase combinations can be found in the Ti-Al-N system. Here, however, I only present a few of them, namely the ones that are lowest in energy.

Step 1: Check which nitride is the thermodynamically most stable:

$$E(\text{TiN}) + E(\text{Al}) = -23.188 \text{ eV}$$

$$E(\text{AlN}) + E(\text{Ti}) = -22.656 \text{ eV}$$

⇒ TiN and Al is more stable than AlN and Ti, i.e. N prefers to bond to Ti.

Step 2: Check if Ti₂AlN is thermodynamically more stable than binary compounds with the same global concentration (the two most probable cases):

$$E(\text{Ti}_2\text{AlN}) - \frac{E(\text{TiAl}_2) + E(\text{TiN}) + E(\text{Ti}_2\text{N})}{2} = -0.354 \text{ eV}$$

$$E(\text{Ti}_2\text{AlN}) - E(\text{TiN}) - E(\text{TiAl}) = -0.459 \text{ eV}$$

⇒ Ti₂AlN is more stable than a combination of those binary compounds.

The two last steps compare Ti_2AlN with other stable ternaries.

Step 3: Check if Ti_2AlN is thermodynamically more stable than Ti_3AlN and some compounds with the same global concentration (the most probable case):

$$E(Ti_2AlN) - \frac{E(Ti_3AlN) + 2E(TiN) + E(TiAl_2)}{3} = -0.3993 \text{ eV}$$

$\Rightarrow Ti_2AlN$ is more stable than Ti_3AlN with a combination of other compounds.

Step 4: Check if Ti_2AlN is thermodynamically more stable than Ti_4AlN_3 and some compounds with the same global concentration (the most probable case):

$$E(Ti_2AlN) - \frac{E(Ti_4AlN_3) + 2E(TiAl)}{3} = -0.2393 \text{ eV}$$

$\Rightarrow Ti_2AlN$ is more stable than Ti_4AlN_3 with a combination of other compounds.

These calculations agree with the fact that Ti_2AlN exists as a thermodynamically stable phase!

To check whether it is possible to synthesize Ti_3AlN_2 , similar calculations can be performed. The most important step is to compare Ti_3AlN_2 with a mixture of Ti_4AlN_3 and Ti_2AlN .

$$E(Ti_3AlN_2) - \frac{E(Ti_4AlN_3) + E(Ti_2AlN)}{2} = 0.092 \text{ eV}$$

The numerically positive result shows that it is energetically more favorable to form a mixture of Ti_4AlN_3 and Ti_2AlN instead of Ti_3AlN_2 . From this I conclude that Ti_3AlN_2 is not thermodynamically stable. However, it might still be metastable as predicted in Reference 65.

Only Ti_2AlN ,^{3,4} sometimes with inclusions of Ti_3AlN ,⁵ has been synthesized as thin films. *Paper 7* is about the attempts to synthesize Ti_4AlN_3 (known from bulk) as a thin film, but both this and at least two more attempts have not succeeded. It is, though, a good example showing that things can well be predicted with calculations. Synthesis, however, may eventually not be feasible because of experimental conditions, like temperature (which affects the ad-atom mobility and thereby kinetics of the thin film growth), film-template interactions, or the formation of competing phases.

3.2.2 Sc-Al-N SYSTEM

The research leading to *Paper 1* was intended to explore the ternary Sc-Al-N phase diagram. As is shown in the paper, the perovskite Sc_3AlN is in fact thermodynamically stable at the global concentration of Sc:Al:N=3:1:1 according to enthalpy calculations analog to the ones above. The depositions of Sc_3AlN succeeded and all characterizations agree with the prediction. Further calculations also show that the calculated lattice parameter of 4.42 Å agrees with the experimentally observed 4.40 Å.

A hypothetical MAX phase Sc_2AlN is, however, not thermodynamically stable according to

$$E(\text{Sc}_2\text{AlN}) - \frac{2E(\text{Sc}_3\text{AlN}) + 3E(\text{ScN}) + E(\text{Al}_3\text{Sc})}{5} = 0.3347 \text{ eV}$$

$$E(\text{Sc}_2\text{AlN}) - \frac{E(\text{Sc}_3\text{AlN}) + 2E(\text{ScN}) + E(\text{Al}_2\text{Sc})}{3} = 0.3509 \text{ eV}$$

yielding positive values. Correspondingly, my thin film deposition experiments with a global concentration of approximately Sc:Al:N = 2:1:1 yields a phase mixture of Sc_3AlN , ScN, and Al_3Sc .

3.3 LATTICE PARAMETER CALCULATIONS

In my work so far, the calculated lattice parameters have always shown to be in agreement with experimental values, besides the slight systematic overestimation from the applied GGA. Therefore, the calculated values can be seen as a trustable tool for verifying the experiments.

Experimentally it can be really tricky to establish if a solid solution between two binary phases has actually formed or if phase separation on a nanometer scale has occurred. After using all kinds of available equipment during the work leading to *Paper 4*, I was for a while led to believe that at least 50% ScN could be dissolved into w-AlN. The calculated lattice parameters, however, did not agree with the experimental observations. After a lengthy and more detailed further microstructural investigation, I have finally been able to conclude that only about 22% ScN can be dissolved into w-AlN under my experimental conditions, and that the films at higher ScN concentrations phase separate into few-nanometer-sized ScN- and AlN-rich domains.

In *Paper 2*, the lattice parameter calculations were a helpful tool when drawing conclusions of the solid solubility of AlN in c-ScN. Unlike in the example above, it was clear already from the electron diffraction patterns of $\text{Sc}_{0.27}\text{Al}_{0.73}\text{N}$ that the film had phase separated. A combination of X-ray diffraction, transmission electron microscopy, Rutherford backscattering spectroscopy and lattice parameter calculations was used to draw the conclusion that 60% AlN can be dissolved in ScN. In this particular case the calculated results were not far from Vegard's rule⁹⁰ and similar conclusions could have been drawn without calculations, however, with a lower confidence.

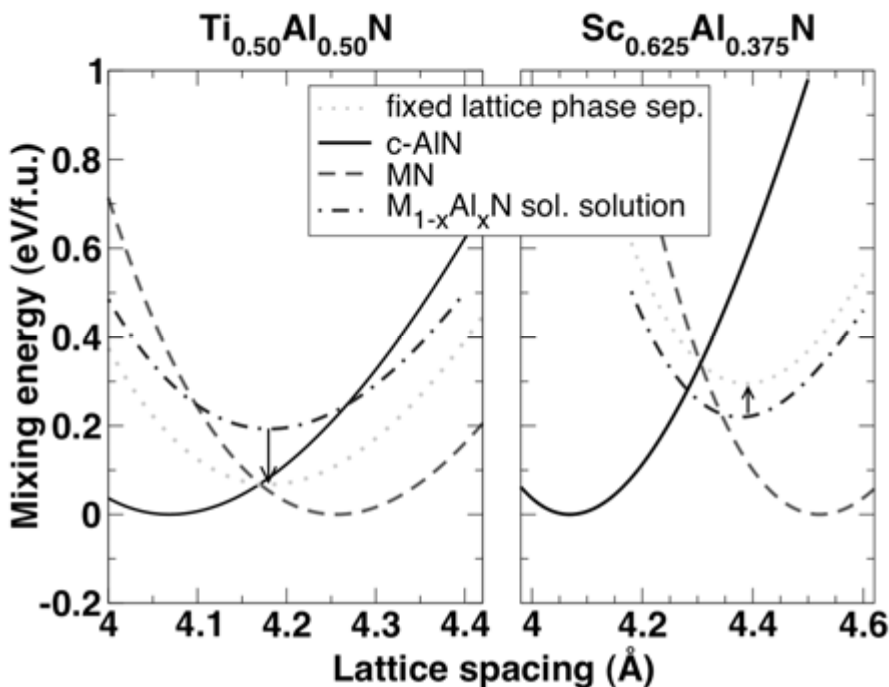


Figure 9: Calculated and normalized energy-lattice spacing curves for $\text{Ti}_{0.50}\text{Al}_{0.50}\text{N}$ (left) and $\text{Sc}_{0.625}\text{Al}_{0.375}\text{N}$ (right). The curves of the solid solutions are shown with dashed-dotted lines, while the dotted lines show hypothetical phase separations, for which the resulting lattice spacing is forced to be the same for both components.

According to the discussion in Reference 103, a systematic positive deviation from Vegard's rule for cubic $\text{M}_{1-x}\text{Al}_x\text{N}$ solid solutions (with $\text{M} = \text{Ti}, \text{Sc}, \text{Cr}, \text{Hf}$) is likely to originate from that all nearest neighbor bonds are between metal and nitrogen atoms. No

metal-to-metal or nitrogen-to-nitrogen bonds exist, so the solid solution does not have the average bond length expected from fully randomly ordered atoms in the structure. In addition, the Al-N and Ti-N (or Sc-N) bonds differ, and it is easier to extend AlN than to compress TiN.¹⁰³ In Figure 9, the mixing energy versus lattice spacing for c-Ti_{0.5}Al_{0.5}N and c-Sc_{0.625}Al_{0.375}N is redrawn from *Paper 3*. Just by taking the mixing energy averages between the binaries (normalized to zero), for each corresponding lattice spacing, the dotted curves are obtained. As expected from the systematic positive deviation from Vegard's rule, the minima of the dotted curves are at slightly higher lattice constants than what Vegard's rule would yield. Compared to mixing energy calculations of cubic solid solutions (dash dotted curve), the lattice parameter positions of the minima are close to identical. A significant difference is, however, seen in the position of the minima on the energy scale. For c-Ti_{0.5}Al_{0.5}N, the solid solution curve is seen above the phase separated energy averages, showing that there is a strong driving force for isostructural phase separation, which is explained by electronic structure mismatch effects.⁴⁸ In contrast, the solid solution curve for c-Sc_{0.625}Al_{0.375}N appears below the phase separated energy average, meaning that there is no driving force for isostructural phase separation in this system. The main purpose of the experiments in *Paper 3* was to explore how this absence of an electronic structure caused driving force influences the phase separation of c-Sc_{1-x}Al_xN during annealing.

3.4 MIXING ENTHALPIES OF COMPETING CRYSTAL STRUCTURES

The Sc_{1-x}Al_xN and Ti_{1-x}Al_xN systems have a positive mixing enthalpy from $0 < x < 1$, meaning that they have a miscibility gap of composition in which their solid solutions are metastable or, possibly, completely unstable. Thin films are often grown far from thermodynamic equilibrium, which makes synthesis of metastable solid solutions possible. Slow kinetics during film growth prohibits long range diffusion needed to form phase separated domains, and for systems where the binaries have different ground state structures, solid solutions of both structures (or even other structures) are possible.¹⁰⁴ The relative energies between solid solutions with different structures affect the formation probability for each structure. Figure 6 in *Paper 4*, shows mixing enthalpy calculations of possible crystal structures in the Sc_{1-x}Al_xN system. It can be seen that the crossover between cubic (ScN ground state) and wurtzite (AlN ground state) structures is at $x \approx 0.45$. The hexagonal ScN structure is also included, but it has never the lowest mixing enthalpy. Close to $x = 0.45$, the mixing enthalpies for all three structures are close and it is in this

area where one could expect different crystal structures depending on deposition conditions. The result in *Paper 2* (that 60% AlN can be dissolved into ScN) is a good example that the crossover point in mixing enthalpy calculations can not directly be translated to experimental changes in structure, but can be seen as a rule of thumb. The calculations assume bulk material, equilibrium volumes and a temperature of 0 K, while the thin films in the mentioned paper are epitaxially grown onto a ScN(111) seed layer, at a substrate temperature of 600 °C. Good conditions for rocksalt ScN growth obviously extend the limits for rocksalt $\text{Sc}_{1-x}\text{Al}_x\text{N}$ growth, clearly demonstrating the importance of kinetics beside the energetics during synthesis of the solid solution phases.

4. PHASE FORMATION AND TRANSFORMATION

Many of the papers in this Thesis deal with phase formation and phase transformations in one way or another. In this chapter I describe some fundamental concept that have been useful for me in my experimental work and are related to the topic. I look upon basic crystallography, epitaxy including lattice match and how to determine epitaxial relations, and finally I write a few words about phase transformation mechanisms.

4.1 CRYSTALLOGRAPHY

Crystallography is an experimental science, where the arrangement of atoms in solids is studied. A full description of crystallography is beyond the scope of this Thesis. Here, I provide a summary of useful concepts that can not be circumvented, and can make life a bit easier.

To be able to distinguish between planes and directions, the following notation is used:

- $(h\ k\ l)$ \Rightarrow One particular plane
- $[u\ v\ w]$ \Rightarrow One particular direction
- $\{h\ k\ l\}$ \Rightarrow Crystallographically equivalent planes
- $\langle u\ v\ w \rangle$ \Rightarrow Crystallographically equivalent directions

For any structure, except for hexagonal and rhombohedral, it is a convention to use a 3-index *Miller notation*. Hexagonal structures can also be described in 3 indices, but they are more easily described with 4, $(h\ k\ i\ l)$ and $[u\ v\ t\ w]$, where the three first indices add up to zero, by using the *Miller-Bravais notation*. Why the 4-index notation is convenient and how to convert between the 3- and 4-index notations is described in the next section. Throughout the Thesis I have used 3 indices for cubic structures and 4 indices for hexagonal structures, often next to each other. In addition to facilitating the identification of equivalent directions and planes in hexagonal structures, this convention eliminates the need to state explicitly whether a given zone or plane symbol refers to a hexagonal or cubic description.

4.1.1 MILLER (3-) AND MILLER-BRAVAIS (4-) INDICIES

Already in 1922, L. Weber invented the four-index notation for planes and directions in hexagonal, rhombohedral, and orthorhombic structures. The close packed basal planes in hexagonal structures get a cubic representation, which is useful for calculating distances and angles in such structures, and for identifying directions and planes by simple permutations of the first three indices.

Figure 10, shows the basal plane of a hexagonal structure, with the main directions in 3-index-notation in (a) and 4-index-notation in (b). In Figure 10(a), the basal plane of a hexagonal structure is described with 2 crystallographic axes, where the basis vectors \mathbf{a}_1 and \mathbf{a}_2 represent the directions along $[10]$ and $[01]$, and subtend a 120° angle. Figure 10(b) shows the hexagonal basal plane when described with respect to 3 crystallographic axes. The basis vectors \mathbf{a}_1 , \mathbf{a}_2 , \mathbf{a}_3 , with the directions $[2\bar{1}\bar{1}]$, $[\bar{1}2\bar{1}]$, $[\bar{1}\bar{1}2]$, respectively, form a 120° angle between each two. In both cases, \mathbf{c} corresponds to the z-axis, which is perpendicular to \mathbf{a}_i (all of them) and points out of the paper. The c -axis is along the $[001]$ or $[0001]$ direction, for 3- or 4-index notation, respectively.

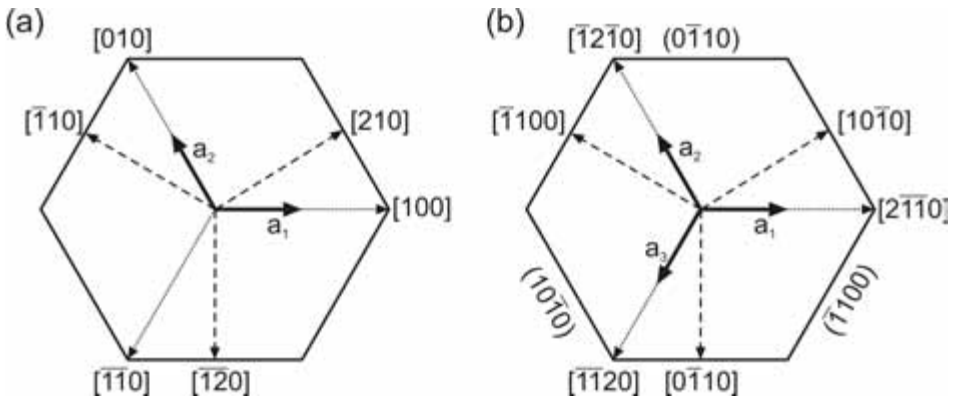


Figure 10: Overview of the basal plane of a hexagonal structure, including crystallographic axes and directions using (a) 3-index and (b) 4-index notations.

The basis vectors \mathbf{a}_1 , \mathbf{a}_2 , and \mathbf{c} in the 3-index notation are indexed like we are used to from cubic structures, except for the 120° angle between \mathbf{a}_1 and \mathbf{a}_2 . One problem with this indexing is that planes and directions with the same index in general are not orthogonal to

each other. Another important detail is that permutations of indices do not correspond to equivalent directions. This can clearly be seen in Figure 10(a), where $[\bar{1}10]$ and $[\bar{1}\bar{1}0]$ correspond to two non-equivalent directions, respectively.

In 4-index notation, the hexagonal basal plane is treated like a (111)-oriented cubic plane. The choice of basis vectors is on first sight inconvenient, but stems from the equivalency of $\langle 2\bar{1}\bar{1} \rangle$ directions in cubic (111). The advantage is that all \mathbf{a}_i directions are permutations of indices $\{[\bar{2}\bar{1}\bar{1}], [\bar{1}\bar{2}\bar{1}], [\bar{1}\bar{1}\bar{2}]\}$ instead of $\{[10], [01], [\bar{1}\bar{1}]\}$, which is illustrated with dotted lines in Figure 10(b) and (a), respectively. Another example is seen with dashed lines in Figure 10, with the 4-index basal plane vectors $\{[10\bar{1}], [\bar{1}10], [0\bar{1}1]\}$ in comparison to the 3-index vectors $\{[21], [\bar{1}\bar{1}], [\bar{1}\bar{2}]\}$. When using the 4-index notation $[h k i 0]$ is perpendicular to $(h k i 0)$ and $[0001]$ is perpendicular to (0001) , as can be seen in Figure 10(b). This is useful when calculating angles between planes and directions. Additionally, it allows a much simpler way of visualizing relations between general directions and planes by decomposing them into their basal (first three indices) and vertical (c) components.^{105,106}

To convert 3-index notation to 4-index notation:

$$\text{Directions } [u \ v \ w] \Rightarrow \text{Directions } [(2u - v) \ (2v - u) \ (-u - v) \ 3w]$$

$$\text{Planes } (h \ k \ l) \Rightarrow \text{Directions } [h \ k \ (-h - k) \ l]$$

To convert 4-index notation to 3-index notation:

$$\text{Directions } [u \ v \ t \ w] \Rightarrow \text{Directions } [(u - t) \ (v - t) \ w]$$

$$\text{Planes } (h \ k \ i \ l) \Rightarrow \text{Planes } (h \ k \ l)$$

I use the $[111]$ direction as an example: $[111] \Rightarrow [(2-1) \ (2-1) \ (-1-1) \ (3*1)] = [1 \ 1 \ -2 \ 3] \Rightarrow [(1-(-2)) \ (1-(-2)) \ (3)] = [333]$, which is parallel to $[111]$.

From these descriptions the question arises, why do we not use the 4-index notation for all crystal structures? Cubic crystals have hexagonal (111) planes, within which hexagonally symmetric directions can be defined. The difference to hexagonal crystals is, though, that the cubic crystals have 3-fold symmetry around (111), instead of 6-fold. This means that the equivalent directions $[\bar{2}\bar{1}\bar{1}0]$ and $[\bar{2}\bar{1}\bar{1}0]$ in hexagonal crystals are not equivalent in cubic crystals. Using 4 indices for cubic crystals would be as problematic to deal with, as when using 3 indices for hexagonal crystals. However, it can be convenient in some cases (e.g. changes of phase and topotaxial reactions) when a common description is desired for different structures.

4.1.2 DIFFRACTION PATTERNS AND POLE FIGURES

In this Thesis, the main techniques to identify crystal structures and their relative orientation are diffraction patterns and pole figures. The information obtained from the techniques is similar, which means that they in many cases are complementary.

Diffraction patterns are recorded in the transmission electron microscope. Each spot in the pattern corresponds to a set of (h k l) planes in the crystal. Before recording diffraction patterns it is practically important to align the sample so that low index planes are perpendicular to the incident electron beam direction, named the *zone axis*.¹⁰⁷ The diffraction pattern stems from reciprocal lattice points which intercept with the Ewald sphere determined by the chosen zone axis. Solving the crystal structure can be done in several ways. For common structures, like the face centered cubic, there are standard diffraction patterns available for some zone axes, and they show spot distance ratios and angles between plane normals.¹⁰⁷ For more complicated structures, computer programs like the CaRIne Crystallography¹⁰⁸ or WebEMAPS¹⁰⁹ are available. In these programs the reciprocal lattice for any crystal structure can easily be plotted along arbitrary zone axes.

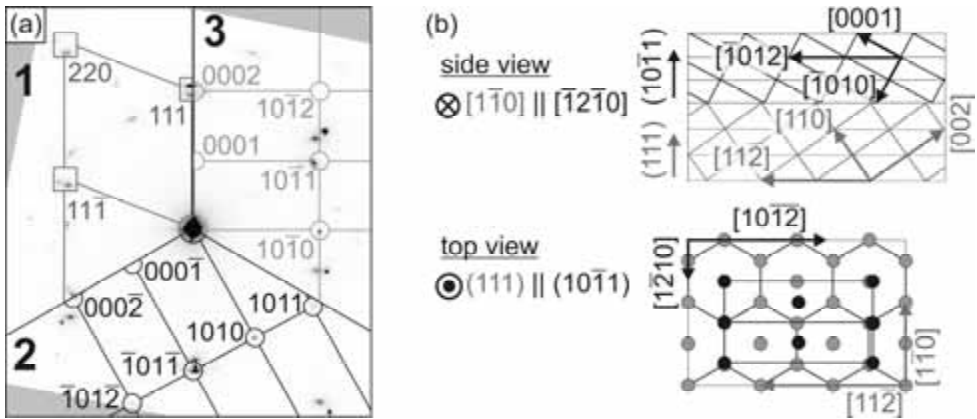


Figure 11: (a) shows a typical indexed selected area electron diffraction pattern. It stems from the $x = 0.90$ sample in *Paper 2*. (b) shows an original epitaxial relationship between the ScN seed layer (grey) and the w-(Sc)AlN film (black), both as side- and top views, corresponding to the indexing in the second section in (a).

An example from *Paper 2* is shown in Figure 11. The diffraction pattern in Figure 11(a) contains contributions from two epitaxial relationships between the ScN(111) seed layer and w-Sc_{1-x}Al_xN film. The first section corresponds to the cubic seed layer. The second and third sections correspond to wurtzite film structures. A tilted basal plane growth is seen in the second section and is illustrated schematically in Figure 11(b), both from the side and as a top view. The epitaxial relationship is w-Sc_{1-x}Al_xN(10 $\bar{1}$ 1) \parallel ScN(111) and w-Sc_{1-x}Al_xN($\bar{1}$ 2 $\bar{1}$ 0) \parallel ScN[1 $\bar{1}$ 0] with an in-plane lattice mismatch of 1.95% and 2.19% along [$\bar{1}$ 2 $\bar{1}$ 0] and [10 $\bar{1}$ 2], respectively. The third section in Figure 11(a) corresponds to a (0001)-orientation of the wurtzite-structure film.

X-ray pole figures is an alternative (or complementary) technique for identifying crystals and determining their orientation, and is for example used in *Paper 3* and *Paper 7*. For a certain plane spacing in the crystal lattice, a *stereographic projection* is recorded, by tilting the sample $0 \leq \Psi \leq 90^\circ$ and $0 \leq \varphi \leq 360^\circ$ (pole figures are further described in Section 6.2.2). The stereographic projection is a way to display the three dimensional angular relationships between lattice planes and directions in two dimensions. Every plane in the crystal is represented by a set of plane normals, radiating from one point within the crystal. When placing a reference point in the center of a sphere, the plane normals intersect the surface of the sphere at a set of points, called poles. These poles are then projected within a circle so that angles are preserved.¹¹⁰ Usually, the poles from planes that are parallel to the surface are positioned in the center of the projection. Poles from planes that are perpendicular to the central plane are then positioned at the border of the projection. This means that for one lattice spacing a “half sphere of planes” from the sample can be recorded in one pole figure measurement. Figure 4 in *Paper 3* shows two pole figures, together with a stereographic projection as the interpretation. The topotaxial relations between c-ScN and w-AlN, in real space, are also illustrated in this figure.

4.2 EPITAXY

4.2.1 EPITAXIAL GROWTH

Epitaxial thin film growth means that the film which is grown is influenced by the structurally-ordered fashion of the material that it is deposited on. Epitaxy arises when the system lowers its interfacial energy to align the lattice of the film with that of the substrate. There are two types of epitaxy, *homoepitaxy* where the film and the substrate are of the same material (e.g. Si on Si), and *heteroepitaxy* where the film and substrate are composed

of different materials like in this Thesis. In homoepitaxy there will be no strain between the film and the substrate as long as the concentration of vacancies is constant and consequently the lattice parameters are perfectly matched. In most of the cases of heteroepitaxy the lattices are not matched. Hence, the deposited film can either be strained to match the substrate coherently or relaxed by introducing dislocations, possibly in a semi-coherent manner.¹¹¹

All films in this Thesis are epitaxially grown on nearly lattice-matched seed layers and substrates. Growth on amorphous or non-lattice-matched substrates typically yields incoherent interfaces, and (albeit possibly crystallographically oriented) polycrystalline or amorphous films.

For crystallographic orientation relations between layers or crystallites I have tried to use the same convention. First the two parallel planes at the interface are described as $(h_1 k_1 l_1) \parallel (h_2 k_2 l_2)$. To fully define the rotation relation, also the in-plane orientation is needed. It is described by two directions which are parallel, as $[u_1 v_1 w_1] \parallel [u_2 v_2 w_2]$.

4.2.2 LATTICE MATCH

Some crystal structures can not be grown on arbitrary oriented materials. The reason could be that a phase is metastable and even though the global composition is correct, the material phase separates. Epitaxial forces can help some materials to grow, especially if the lattice mismatch between the underlying material and the film is small.

Table 2 shows a summary of lattice mismatches between phases and corresponding orientations that are relevant to the Thesis. I define lattice mismatch as

$$\Delta_d = \frac{d_B - d_A}{d_A}, \quad (4.1)$$

where d_A and d_B correspond to plane spacings from phase A and B, and where phase B is positioned to the right of phase A in the top of the table.

The table lists both substrate and film materials. At the top, the *Strukturbericht* designation for each structure is given, together with the lattice parameters. The table is then divided into two halves.

The upper right half table (light grey) shows the *in-plane lattice mismatch*, which I define as the difference in average atomic distances (d_{atom}) in the interface planes of the two

Table 2: *In-plane lattice mismatch* (upper right) and *out-of-plane d-spacing difference* (lower left) for relevant phases and corresponding planes. The *Strukturbericht* designation and lattice parameters for each phase are also listed. Lattice parameter data are collected from *Paper 1*, Reference 112, 62, 74, 18, and ICDD PDF 46-1212, 21-1152, 44-1294, 45-0946, 38-1420, 25-1133.

		In-plane lattice mismatch (%)										
Phase	Plane	Al ₂ O ₃	c-AIN	MgAl ₂ O ₄	Ti ₃ AlN	Ti	MgO	Ti ₂ AlN	TiN	w-AIN	Sc ₃ AlN	ScN
	Structure	D5 ₁	B1	H1 ₁	E2 ₁	A3	B1	-	B1	B4	E2 ₁	B1
	a [Å]	4.76	4.05	8.08	4.11	2.95	4.21	2.99	4.24	3.11	4.40	4.50
	c [Å]	12.99	-	-	-	4.68	-	13.61	-	4.98	-	-
	Plane	(0001)	(111)	(222)	(111)	(0001)	(111)	(0001)	(111)	(0001)	(111)	(111)
	d_{atom}	2.71	2.86	2.86	2.91	2.95	2.98	2.99	3.00	3.11	3.11	3.18
	d_{plane}	2.17	5.53	5.53	7.38	8.86	9.96	10.33	10.7	14.76	14.76	17.34
Al ₂ O ₃	(0006)	-	-	0.00	1.75	3.14	4.20	4.54	4.90	8.74	8.74	11.19
c-AIN	(111)	7.83	-	0.00	1.75	3.14	4.20	4.54	4.90	8.74	8.74	11.19
MgAl ₂ O ₄	(222)	7.74	-0.43	-	1.75	3.14	4.20	4.54	4.90	8.74	8.74	11.19
Ti ₃ AlN	(111)	9.21	1.28	1.72	-	1.37	2.41	2.75	3.09	6.87	6.87	9.28
Ti	(0002)	7.83	0.00	0.43	-1.27	-	1.02	1.36	1.69	5.42	5.42	7.80
MgO	(111)	11.98	3.85	4.29	2.53	3.85	-	0.34	0.67	4.36	4.36	6.71
Ti ₂ AlN	(0006)	4.61	-2.99	-2.58	-4.22	-2.99	-6.58	-	0.33	4.01	4.01	6.35
TiN	(111)	12.90	4.70	5.15	3.38	4.70	0.82	7.93	-	3.67	3.67	6.00
w-AIN	(0002)	14.75	6.41	6.87	5.06	6.41	2.47	9.69	1.63	-	0.00	2.25
Sc ₃ AlN	(111)	17.05	8.55	9.01	7.17	8.55	4.53	11.89	3.67	2.00	-	2.25
ScN	(111)	19.82	11.11	11.59	9.70	11.11	7.00	14.54	6.12	4.42	2.36	-
Out-of-plane lattice mismatch (%)												

involved phases, respectively. This mismatch tells about the epitaxial fit of two materials, or how far from homoepitaxial the materials are. The lower left half of the table (dark grey) shows the *out-of-plane d-spacing difference* (d_{plane}). By this I mean the difference in d -spacing between two particular diffraction planes that (for most films in this Thesis) are parallel to the film surface and therefore yield peaks in X-ray diffraction. The tabulated values are calculated in the same way as the lattice mismatch and tell about how close two material peaks appear in a symmetric $\theta - 2\theta$ X-ray diffraction scan.

A check for expected peak positions and peak separations is an important part when planning an experiment, to avoid overlaps between substrates, seed layers and films. For *in situ* annealing studies, like in *Paper 3* and *Paper 5*, it is also important to check for peaks that possibly appear during annealing. As can be seen in Table 2, a small in-plane lattice mismatch between two phases does not always mean that the phases can not be separated in symmetric X-ray diffraction scans, and vice versa. As an example, the in-plane mismatch between $\text{Ti}_2\text{AlN}(0001)$ and $\text{MgO}(111)$ is 0.34%, while the out-of-plane mismatch is -6.58%. This means that even though the epitaxial fit is close to perfect, the Ti_2AlN 0006 and MgO 111 peaks can clearly be separated in X-ray diffraction.

4.3 THE SUBSTRATE AND ROLE OF SEED LAYERS

The main substrate materials that I have used are single-crystal $\text{MgO}(111)$ or $\text{Al}_2\text{O}_3(0001)$. The motivation for this is that I aim for single-crystal films, which can be used for determining the material's fundamental properties. The growth of high quality epitaxial films of MAX phase or perovskite material requires a template. A good template is given if the lattice mismatch between the film and the substrate is small, which is the case for these materials. Another important requirement is that the substrate must be stable at temperatures up to $\sim 1000^\circ\text{C}$ to avoid any negative influences from the substrate at the employed deposition temperatures or interdiffusion between the substrate and film. The advantage of Al_2O_3 is that the (0001)-surface can be polished very smooth, while the (111) surface of MgO in comparison is rough. MgO , however, has the advantage of the smallest lattice mismatch to the films deposited in this Thesis. The nominal in-plane lattice mismatch, according to Table 2, between $\text{Ti}_2\text{AlN}(0001)$ and the substrates $\text{MgO}(111)$ and $\text{Al}_2\text{O}_3(0001)$ are 0.33% and 10.33%, respectively.

Unfortunately, both MgO and Al_2O_3 have shown not to be stable enough when judged on a nanometer level for film-substrate reactions. Even at rather low temperatures (690°C and 900°C for MgO and Al_2O_3 , respectively) interdiffusion is observed between the substrates

and films.^{113,114} In *Paper 6*, we observe that the Al_2O_3 substrate reacts with a TiN_x film at an even lower temperature, namely 800°C . To avoid such reactions, a so called seed or buffer layer is deposited onto the substrate before growing the actual film on top. The seed layers chosen were the nitrides ScN in *Paper 1*, *Paper 2*, and *Paper 3*; AlN in *Paper 4* and *Paper 5*; and Ti_2AlN in *Paper 7*. The motivation for the choice is that these seed layers contain the same elements as the films and have a good lattice match to them.

In Figure 12, X-ray diffraction data from films deposited onto three different substrates are shown. This is an example from the work leading to *Paper 2*, where $\text{Sc}_{1-x}\text{Al}_x\text{N}(111)$ films with relatively high Al-contents are deposited onto $\text{ScN}(111)$ seed layers. The used substrates are $\text{MgO}(111)$, $\text{MgAl}_2\text{O}_4(111)$, and $\text{Al}_2\text{O}_3(0001)$, with in-plane lattice mismatch to $\text{ScN}(111)$ of 6.71%, 11.19%, and 17.34%, respectively. The spectra clearly show that the crystalline quality of $\text{ScN}(111)$ decreases with increasing lattice mismatch to the substrate, and hence $\text{MgO}(111)$ should be the preferred substrate choice. Unfortunately, the $\text{Sc}_{1-x}\text{Al}_x\text{N}$ film has a lattice parameter which is very similar to MgO , leading to a severe peak overlap between film and substrate. To be able to determine the lattice parameter of the film the slightly worse seed layer quality when deposited onto $\text{MgAl}_2\text{O}_4(111)$ had to be accepted.

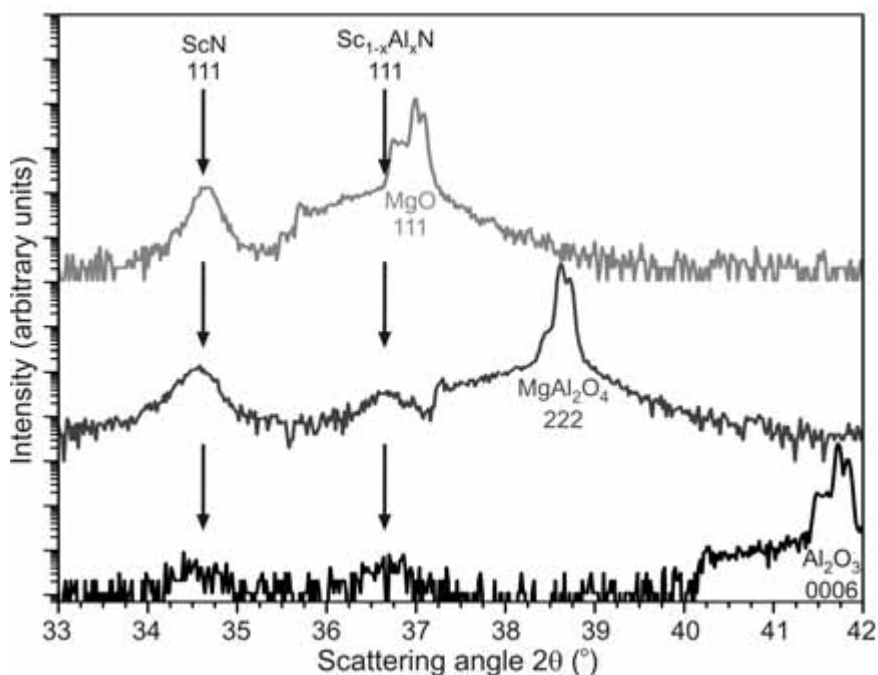


Figure 12: X-ray diffractogram, showing the changing crystalline quality of $\text{ScN}(111)$ seed layers and $\text{Sc}_{1-x}\text{Al}_x\text{N}$ film peak overlaps when deposited onto $\text{Al}_2\text{O}_3(0001)$, $\text{MgAl}_2\text{O}_4(111)$, and $\text{MgO}(111)$ substrates.

4.4 PHASE TRANSFORMATION

Most phases considered in this Thesis are formed already during the thin film sputtering process. There are, though, a few examples where diffusion between layers and phase transformations within layers can result in new phases that can be desirable or not. *Paper 3* deals with spinodal decomposition (described below), which is a desirable process in cutting tool industry, due to the segregation tendency of $Ti_{1-x}Al_xN$ at elevated temperatures, followed by an increase in hardness, so called age hardening. Even the results from solid state reactions in *Paper 5* and *Paper 6* are desirable. Nitrogen understoichiometric (ternary) nitrides are usually tricky to synthesize with reactive magnetron sputtering, due to the influence of the nitrogen gas on the sputter yield of the metallic targets. With the methods used in the mentioned papers this problem can be circumvented. *Paper 7* features an example of a case where diffusion is unintentional. The deposition parameters were calibrated at room temperature for the formation of stoichiometric Ti_4AlN_3 . At optimal deposition temperatures (above 600 °C), however, Al was lost into the vacuum, resulting in a phase mixture of Ti_2AlN and $Ti_{1-x}Al_xN$.

4.4.1 SPINODAL DECOMPOSITION

Spinodal decomposition is a mechanism by which phase transformation proceeds without overcoming an activation energy barrier for nucleation. When a metastable homogenous phase is annealed, to overcome kinetic barriers, spontaneous compositional fluctuations appear. The phase becomes unstable and separates into two phases with different compositions. Since these phases form by a continuous process, the interfaces remain coherent or at least semicoherent during the whole process.¹¹⁵

Spinodal decomposition has been shown several times for $Ti_{1-x}Al_xN$ films.^{40,41,42} At a temperature of ~1000 °C, $Ti_{1-x}Al_xN$ decomposes to form c-TiN and metastable c-AlN. At the same time the hardness of the material increases. The reason for the hardness increase is that the phase transformation induces a coherency strain between the matrix and the small domains that form. When increasing the temperature to ~1400 °C, the decomposition process is completed by the formation of c-TiN and stable w-AlN. At this point the hardness of the material decreases again.⁴⁰

Theoretical studies have shown that the driving force for phase separation of $Ti_{1-x}Al_xN$ is due to the positive isostructural mixing enthalpy. In *Paper 3* we show that a positive mixing enthalpy is not the only requirement for spinodal decomposition. $Sc_{1-x}Al_xN$ has a very

similar mixing enthalpy curve as $Ti_{1-x}Al_xN$, but the origin of the shape of curves is different. $Ti_{1-x}Al_xN$ is affected by an electron band structure effect, which forces the material to phase separate at elevated temperatures. $Sc_{1-x}Al_xN$ does not have this driving force for decomposition. Anyhow, the latter material phase separates at high enough temperature, which is explained by the large lattice spacing mismatch between the binaries.⁴⁸

4.4.2 TOPOTAXIAL PHASE FORMATION

Paper 5 is about topotaxial growth of Ti_2AlN thin films from multilayers. While epitaxy is a lattice match in two dimensions of one material deposited on another, topotaxial phase formation is when growth occurs within the solid state in two or three lattice-matched dimensions.

An example of topotaxy is when Ti_2AlN is formed by solid state reaction between AlN and Ti in a diffusion couple. A discussion about how this phase formation possibly happens is sketched in Figure 13. For each step, the upper image corresponds to a top-view and the lower to a side-view along a given $[u\ v\ t\ w]$ zone axis of the structure, respectively. The starting point is deposition of epitaxial $w-AlN(0001)$ and $hcp-Ti(0001)$ layers. Both layers have a hexagonal structure and the in-plane lattice mismatch between them is only 5.4%, yielding good conditions for high quality layers. When the sample is annealed at 400 °C, AlN slowly decomposes into Al and N atoms that are free to diffuse into the Ti matrix. This temperature together with a Ti -to- AlN ratio of 3:1 is enough for epitaxial $Ti_3AlN(111)$ formation. When the temperature is increased to 500 °C even more Al and N can diffuse, this time into the Ti_3AlN matrix. Less than 5 min is needed before $Ti_3AlN(111)$ with additional Al and N has transformed into the $Ti_2AlN(0001)$ MAX phase.

In Figure 14 and Figure 15 transmission electron microscopy images from the mentioned samples, before and after annealing, respectively, together with a sketch of layers are shown. It can be seen that the individual layer thicknesses changed during the solid state reaction when Ti_2AlN formed. The high resolution images in Figure 15(c) confirms that the layers between AlN in Figure 15(b) indeed are Ti_2AlN , which is seen from the characteristic layered stacking in a MAX phase. This way of forming Ti_2AlN lowered the deposition temperature for basal plane growth by 175 °C to 500 °C.

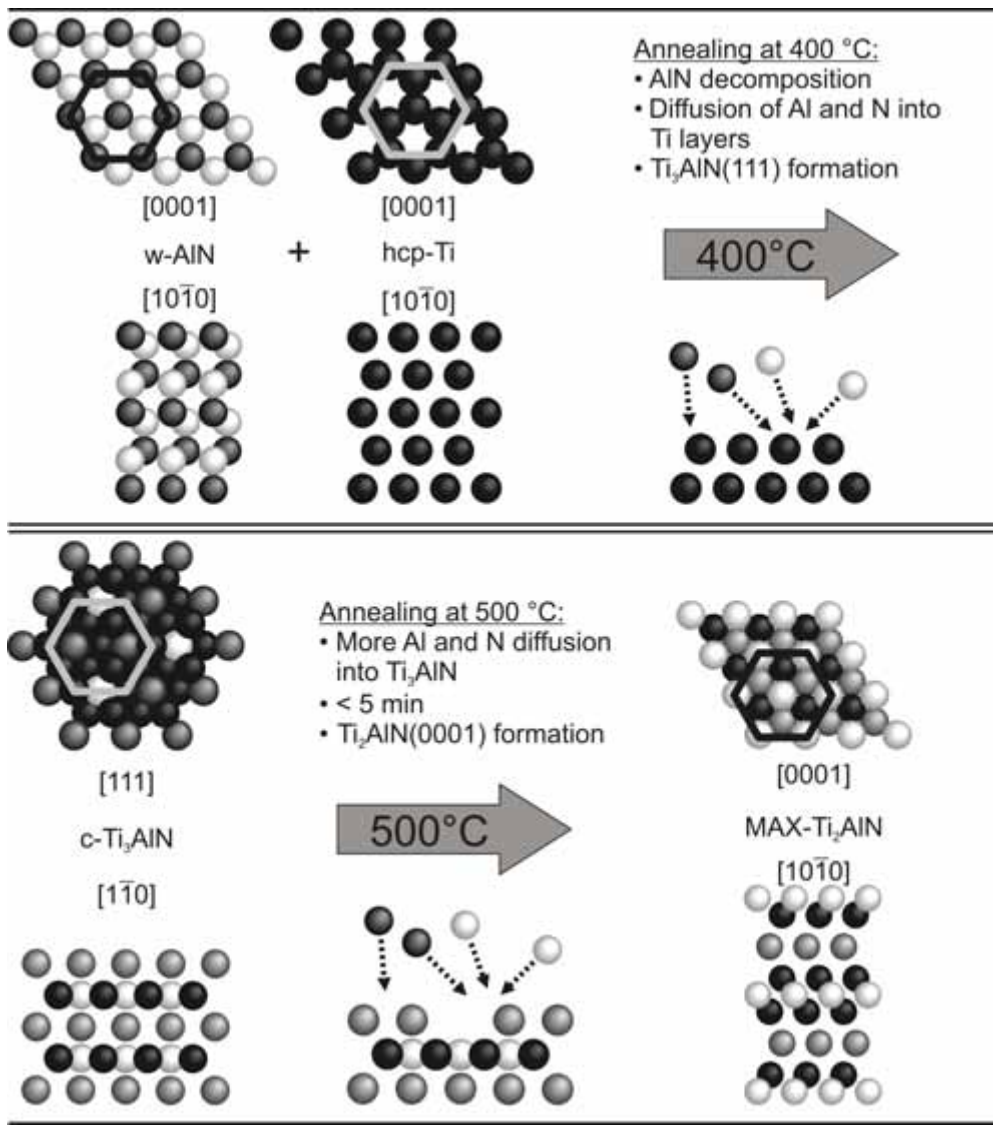


Figure 13: Suggestion for diffusion steps in the formation of Ti_2AlN during solid state reactions in AlN / Ti multilayers.

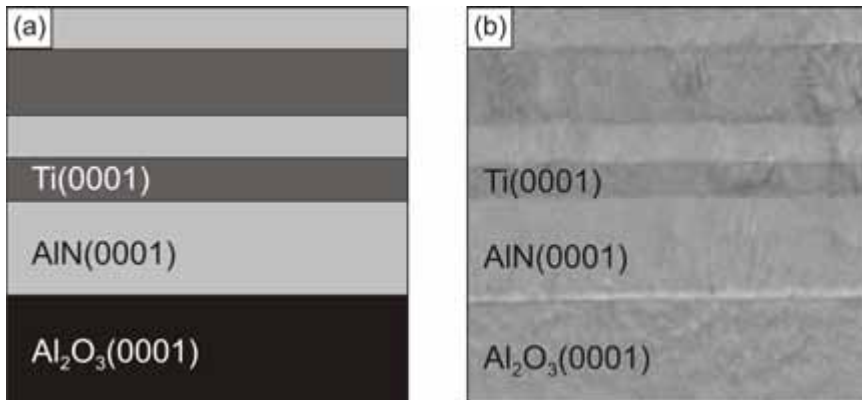


Figure 14: AlN / Ti multilayers before annealing, showing (a) a sketch of the individual layers and (b) an overview cross-sectional transmission electron microscopy image.

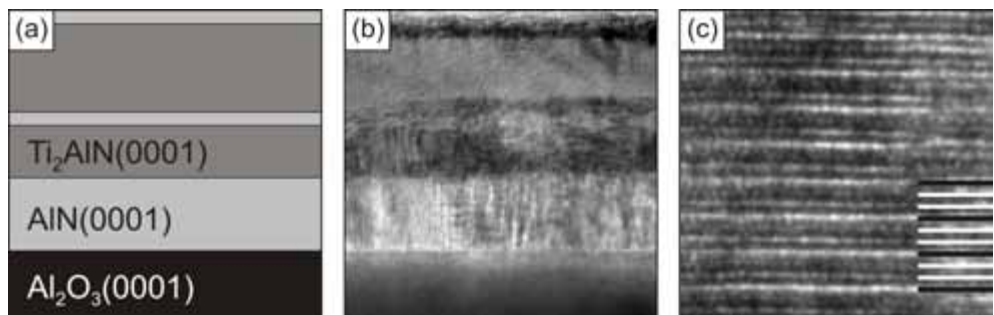


Figure 15: AlN / Ti multilayers after annealing at 500 °C, showing (a) a sketch of the individual layers, (b) an overview cross-sectional transmission electron microscopy image, and (c) a high resolution image showing the typical layered MAX phase structure.

Similar experiments have been performed with diffusion couples of TiN / Al. When annealing epitaxial layers of TiN(111) / Al(111), no phase change is observed. As could be seen in “Step 1” in Chapter 3.2.1, TiN is an energetically more stable nitride than AlN. This means that once TiN has formed, it will not decompose to form AlN, no matter how much Al is accessible or how high the annealing temperature is.

Other combinations of layers that I (and my colleagues) have tried are AlN / M and $M\text{N} / \text{Al}$, where M is Sc, V, or Cr, again with the aim for $M_{1-x}\text{Al}_x\text{N}_x$ phase formation. None of the diffusion couples of $\text{AlN}(0001) / \text{Cr}(110)$, $\text{AlN}(0001) / \text{V}(110)$, $\text{ScN}(111) / \text{Al}(111)$, $\text{VN}(111) / \text{Al}(111)$ or $\text{CrN}(111) / \text{Al}(111)$ show any reaction between the layers during annealing. Both CrN and VN are not very stable nitrides and decompose at relatively low temperatures into Cr_2N and V_2N , respectively. Therefore, there is no driving force for Cr or V to take up N. The employed temperatures during annealing are high enough for CrN to decompose into $\text{Cr}_2\text{N}(0001)$ followed by $\text{Cr}(110)$, but the temperatures are too low for ScN and VN to decompose, meaning that none of the systems can form a $M_{1-x}\text{Al}_x\text{N}_x$ phase even though enough Al is accessible.¹¹⁶

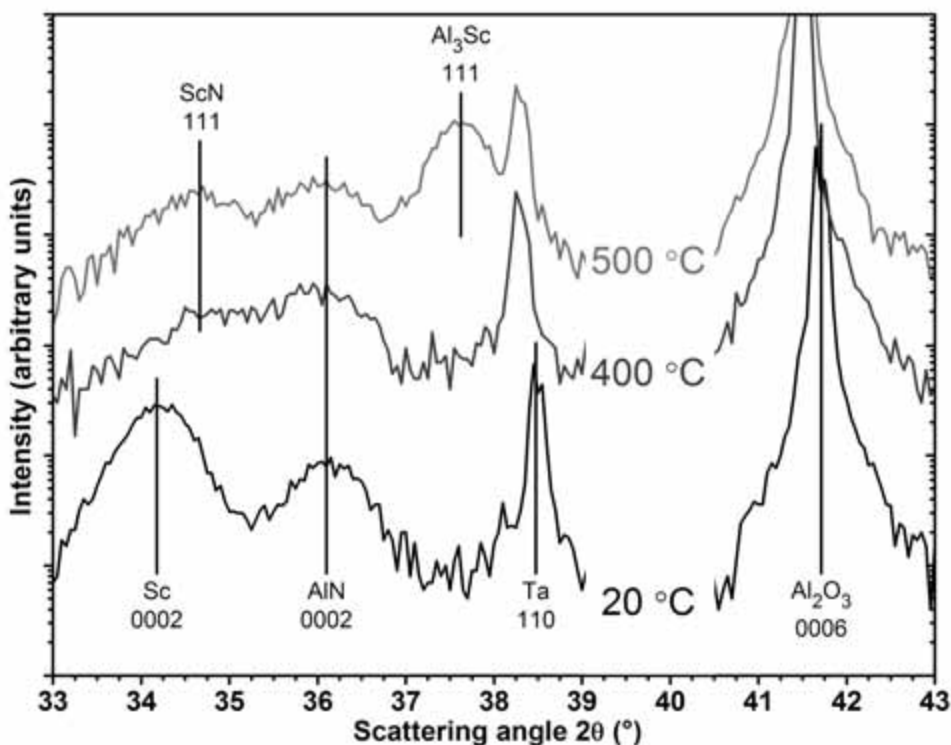


Figure 16: In situ X-ray diffraction data from annealing of $\text{Sc}(0001) / \text{AlN}(0001)$ multilayers.

$\text{Sc}(0001)$ and $\text{AlN}(0001)$ make up the only multilayer couple where a reaction actually occurs during annealing. The *in situ* X-ray diffraction data are shown in Figure 16, with the

spectrum from the as-deposited sample below the annealed ones. The graph for the as-deposited case shows AlN(0001) and Sc(0001) deposited onto a Al₂O₃(0001) substrate and a sharp Ta-peak from the sample holder. When annealing the sample to 400 °C the Sc 0002 peak vanishes, while the AlN 0002 peak widens and ScN(111) starts to form. A temperature of 500 °C is needed to see a clear contribution from ScN(111). This temperature is also high enough to form the intermetallic Al₃Sc(111). As seen in Reference 1, Al₃Sc is the phase that forms when annealing alloys of Al and Sc, which means that it is probably the most stable of the Al-Sc-intermetallic phases. Most likely, the starting layers AlN / Sc / AlN have transformed to an end state with layers AlN / Al₃Sc / ScN / Al₃Sc / AlN. From this state it will be impossible to form a MAX phase through further annealing. This is confirmed by calculations, which indicate that there is no thermodynamically stable Sc_{1-x}AlN_x phase.

Another example for topotaxial phase formation is seen in *Paper 3*, which is an annealing study starting with epitaxial Sc_{1-x}Al_xN(111), deposited onto ScN(111). At temperatures ~1000 °C the phase starts to separate into a matrix of c-ScN(111) together with small domains of w-AlN. When annealing at 1100 °C for more than 1 h, these AlN domains orient themselves in relation to the surrounding ScN as ScN(001) || AlN(0001) and ScN<110> || AlN<10 $\bar{1}$ 0>.

Even in *Paper 6*, topotaxial growth is the reason why Ti₂AlN can form from TiN_x deposited onto Al₂O₃(0001). The nitrogen understoichiometric TiN_x is very apt to react to become a stoichiometric nitride. Due to that this experiment is done in vacuum, there is nothing else than the Al₂O₃ substrate to react with. A temperature of 800 °C is enough for Al₂O₃ to decompose and to grow basal plane Ti₂AlN (and Ti₂O) through interdiffusion between TiN_x and Al₂O₃.

5. THIN FILM DEPOSITION AND GROWTH

This chapter deals with the thin film deposition techniques that I have used in this Thesis. Epitaxial films have been deposited under different conditions using reactive magnetron sputtering. The importance of good vacuum is clarified, while the modes in which the films grow are discussed.

5.1 DC MAGNETRON SPUTTERING

Physical vapor deposition (PVD) is a widely used family of techniques for thin film synthesis under vacuum conditions, where a solid or liquid deposition material is vaporized and condensates on a substrate forming a film. Chemical reactions are usually absent in the gas phase, due to the small probability for collisions of the vapor species under the applied pressures. The usual physical mechanisms for source atoms to enter the gas phase are high temperature evaporation or sputtering. As a comparison, in a chemical vapor deposition (CVD) process gaseous precursors are used and it does not require vacuum conditions.¹¹¹

In this Thesis all films were grown in (ultra) high vacuum chambers by reactive magnetron sputter deposition, in a form that is described below. This technique has the advantage of allowing control of the growth of pure and dense films, which are well suited for materials characterization. Another benefit is that the films are grown far from thermodynamic equilibrium, which makes it possible to form metastable crystalline phases, like solid solutions of $\text{Sc}_{1-x}\text{Al}_x\text{N}$.

5.1.1 VACUUM CONDITIONS

To minimize the amount of impurities in the films it is necessary to have good vacuum conditions in the deposition chamber. All films in this Thesis are deposited or heat treated at base pressures of $\sim 10^{-6}$ Torr or less. Background pressures in the approximate range between 10^{-3} and 10^{-7} Torr correspond to high vacuum (HV), while lower pressures are ultra high vacuum (UHV).¹¹¹

The mean free path (λ) tells, in average, how far an atom can move between two collisions and is (for pressures measured in Torr) described by

$$\lambda = \frac{5 \times 10^{-5}}{P} \text{ [m]}.^{117} \quad (5.1)$$

For the worst applied vacuum of $\sim 10^{-6}$ Torr, the mean free path for atoms is ~ 50 m, while the best employed vacuum conditions of $\sim 10^{-9}$ Torr yield a mean free path of $\sim 50\,000$ m. The difference is large, but in all cases the mean free path is at least considerably larger than the deposition chamber dimensions.

Another important pressure aspect for thin film deposition is the monolayer formation time, τ , which is described by

$$\tau = \frac{2.25 \times 10^{-6}}{P} \text{ [s]}.^{118} \quad (5.2)$$

For pressures of $\sim 10^{-6}$ Torr, the monolayer formation time is ~ 2 s, assuming a sticking coefficient of unity. As an example, the deposition rate for $\text{Sc}_{1-x}\text{Al}_x\text{N}$ films in *Paper 3* is ~ 1.5 Å/s at a background pressure of 4×10^{-6} Torr, meaning that a large proportion of the film could consist of impurities from the ambient. The best best employed vacuum conditions in this Thesis were $\sim 10^{-9}$ Torr, though, and yield a monolayer formation time of 37.5 min. In films grown under such conditions the influence from impurities can in principle be neglected.

5.1.2 THE MAGNETRON SPUTTERING PROCESS

Sputtering is a thin film deposition technique, where atoms are ejected from the source material, a sputtering target, by bombarding the surface with energetic ions. An inert gas, in this case Ar, is added to the deposition chamber as the working gas for the sputtering process. The sputtering target is a solid (or liquid) piece of material, containing elements that are desired in the film. The target is mounted on a magnetron, is negatively charged and acts as the *cathode* in the deposition chamber. Figure 17 presents a schematic drawing of a magnetron. When a high voltage is applied to the target an electrical discharge is produced, which ionizes the gas. The target is then bombarded with the highly energetic gas ions and if the incoming ions are higher in energy than the binding energy of the atoms on the target surface, atoms are ejected (so called *sputtered*). The sputtered atoms and the inert gas (i.e. Ar) form a plasma, and the permanent magnets in the magnetron are used to confine the plasma close to the target surface. Also other particles, like secondary electrons and energetic neutrals, will be ejected from the target. The secondary electrons maintain the

process by colliding with atoms and ions in the plasma, and ionizing them. The magnetic fields from the permanent magnets force the electrons to gyrate close to the target and increase the probability for collisions yielding a plasma ionized to a higher degree. The sputtered atoms traverse the chamber and condensate atomistically on the chamber walls and substrate (*anodes*), forming a film. Depending on the power of each magnetron, the substrate temperature and potential, and the nature of the substrate, the film will contain one or more phases.¹¹¹

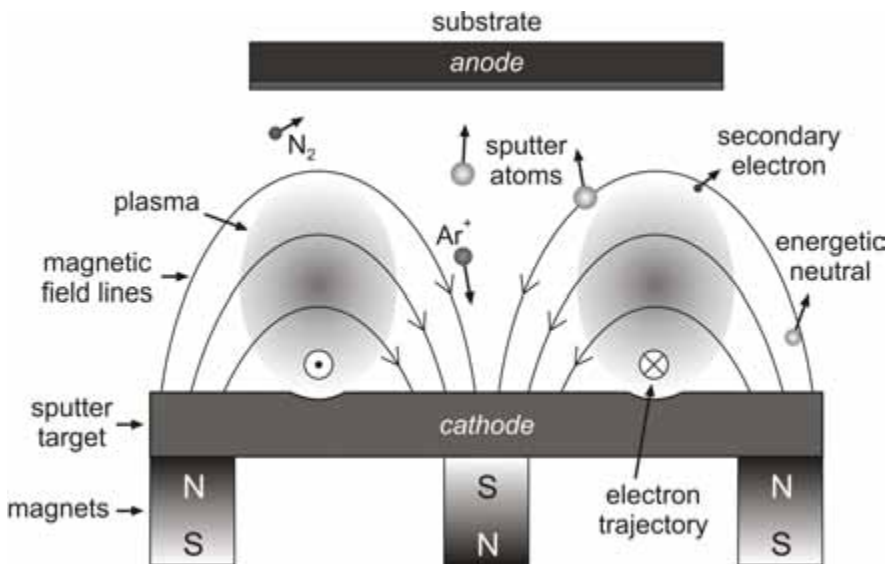


Figure 17: A schematic drawing of a magnetron, facing a substrate.

Three standard types of magnetron configurations are available, namely balanced or unbalanced type I or type II. In a balanced magnetron, the inner and outer magnets have the same strength, which confines the plasma and electrons close to the target. It is though often desirable to have the plasma closer to the substrate to activate reactive gases or to support ion bombardment of the substrate surface. The type II magnetron has stronger outer magnets, and lets some secondary electrons escape towards the substrate. In opposite, the inner magnet is the strongest in a type I magnetron configuration.¹¹¹

5.1.3 REACTIVE MAGNETRON SPUTTERING

The films in this Thesis are grown by reactive magnetron sputtering, with pure N₂ introduced into the chamber as a reactive gas. The N-N bonds are cracked by the energy of the plasma. The metal atoms on the substrate surface have a high affinity for atomic N and react with it to form a metal nitride. No reaction will occur in the gas phase due to the fact that three body collisions are required for conservation of momentum and kinetic energy. This is very unlikely at sputtering pressures of the order of mTorr, as used in this Thesis.

One difficulty when doing reactive sputtering of nitrogen understoichiometric thin films, like Sc₃AlN in *Paper 1*, TiN_x in *Paper 6*, or Ti₄AlN₃ in *Paper 7*, is that low N partial pressures are hard to regulate. Different metals have different reactivity to nitrogen, meaning that a slight change in the nitrogen partial pressure does not only change the metal-to-nitrogen ratio in the film, but can also change the metal-to-metal ratio. I encountered this problem in my attempts to grow the inverse perovskite Sc₃InN. It has a melting point of 157 °C, meaning that applying high magnetron powers results in a molten In target. Therefore, to get the right In-to-N ratio the N flow had to be extremely low. Even though I have used a very sensitive nitrogen mass flow controller, the process was practically impossible to calibrate to get the right film composition.

When doing reactive sputtering, target poisoning has also to be taken into account. The sputtering can be done in *metallic mode*, *transition regime*, or *poisoned mode*. As long as the amount of N that is consumed in the process is larger than the available N₂ gas, the sputtering takes place in a metallic mode and the resulting films contain a low amount of N. The understoichiometric films in *Paper 1*, *Paper 6*, and *Paper 7* are deposited in this mode.

The sputtering yield of nitrides is typically lower than that of metals,¹¹⁹ which means that sputtering from a nitride target (or a nitrated metallic target) results in low deposition rates. The sputtering is said to be done in the poisoned mode. When depositing stoichiometric nitrides it is desirable to be in the transition regime, where a fully poisoned target is avoided and the deposition rate is kept high. The N₂ gas flow has to be *high* enough to get the right N-composition in the film, but *low* enough to keep the deposition rate at an acceptable level.

Unfortunately, I have observed that the deposition process for Sc containing nitrides can be quite unstable when running in the transition regime. The reason could be that ScN is formed on the target surface during the process. ScN is a semiconductor and the employed magnetron configuration requires a metallic target. The problem can be solved by sputtering in pure N₂, but even though the magnetron power was increased from 56 W to

80 W, the deposition rate for ScN films in *Paper 3* was lowered from 0.8 Å/s to 0.3 Å/s. There are several reasons for why even more N₂ and/or the absence of Ar can make the process more stable. I have not focused on finding out the reasons, but one hypothesis is that the plasma changes its ionization, due to the different secondary electron yield of Ar and N, which changes the plasma density and influence the process. Another reason could be the mass difference between Ar and N atoms, yielding different penetration depth of the working gas into the sputtering target. The energy of the ions is the same (set by the plasma potential) but the energy transfer is more efficient from heavy ions.

In the late eighties Berg *et al.* presented a model for reactive sputtering, which since then has been continuously extended. As many parameters as possible were considered in this extremely complex system. They offered mathematical relationships to minimize the number of necessary experiments. For example, they explain the observed hysteresis behavior on sputtering rate and gas pressure as functions of gas flow, and how to avoid target poisoning to increase the deposition rate while getting stoichiometric films. But they also recognize that many physical parameters, like pressure, pumping speed, and current density must be known and changing one parameter affects the whole process.^{120,121,122} In the end, there are many sources of error when applying the model in reality, and as the experimentalist I am, it is acceptable to fail with a few experiments on the way to optimized deposition parameters.

5.1.4 MAGNETRON SPUTTER EPITAXY

With magnetron sputter epitaxy (MSE) is meant that epitaxial thin films are deposited with magnetron sputtering, under strict requirements regarding vacuum conditions and sample handling. The conditions are compared with what is practice in molecular beam epitaxy (MBE).¹²³ The method requires for example ultra high vacuum background pressures, very pure working and reactive gases, and high sputtering target purities. The films in *Paper 1*, *Paper 2*, *Paper 4*, and *Paper 6* were grown by MSE. From compositional analysis it is clear that the resulting amount of impurities, like H, C, and O, in these films is much lower than in the other films.

5.2 NUCLEATION AND GROWTH

When the vapor atoms impinge on the substrate, ad-atoms assemble and nucleate to form two or three dimensional islands on the substrate surface. The islands grow larger and finally coalesce to form a continuous film. How the coalescence and continuous growth will occur depends on the mobility of atoms on the surface and the higher the mobility, the more liquid-like coalescence. The growth continues and forms a closed network of islands. The empty areas slowly fill up, leaving voids here and there.^{111,124}

There are three different initial growth modes observed, illustrated in Figure 18.¹¹¹ These are:

2D-layer growth: The growth is in two dimensions, filling up one atomic layer before the next layer starts to form. The deposited atoms are more strongly bound to the substrate than to each other. Epitaxial semiconductor films are known to grow in 2D-layers.¹¹¹

3D-island growth: Clusters of atoms nucleate on the substrate and grow in three dimensions to form islands. This happens when the deposited atoms are stronger bonded to each other than to the substrate. Metals and semiconductors grown onto oxides form such islands.¹¹¹

Stranski-Krastanov growth: This is a combination of layer and island growth, which starts with the formation of a few layers and continues with island formation. It is a common growth mode and is for example known to form in metal-metal and metal-semiconductor systems.¹¹¹

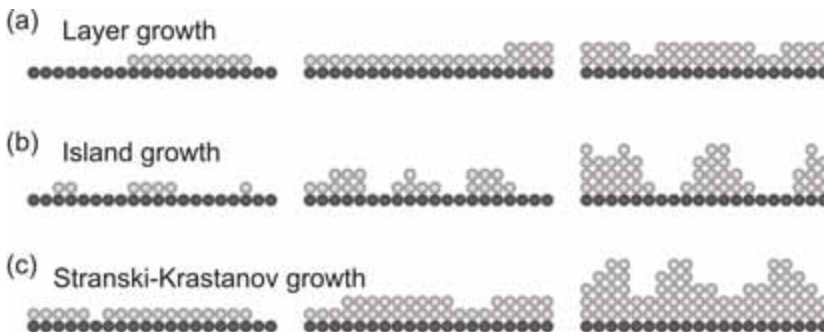


Figure 18: Basic modes of thin film growth with (a) 2D-layer growth, (b) 3D-island growth, and (c) Stranski-Krastanov growth [From Reference 111].

How the microstructure evolves during growth depends on the ratio between deposition temperature and melting point of the material.¹²⁴ The texture evolution of polycrystalline TiN layers has with *ab initio* methods been shown to depend on the N₂ partial pressure or the flux ratio between N₂⁺ and Ti, with preferred 111-oriented grains in typical reactive sputter deposited films.¹²⁵ Wall *et al.* have varied the N₂/Ar flux ratios and temperatures during homoepitaxial growth of TiN(001). Low flux ratios yield a 2D-layer growth process, while higher flux ratios result in 3D-island formation. High flux ratios, combined with higher temperatures lead to flatter and larger 3D-islands.¹²⁶ The roughness evolution during growth was in *Paper 3*, *Paper 5*, and *Paper 7* followed with time resolved X-ray interference (described in Section 6.2.5), and gives a hint about the growth modes and microstructural evolution of the films. When the surface roughness during growth increases rapidly, it is likely due to 3D-island formation. Following this argument, the rapid roughening of the AlN layers in *Paper 5* are an indication for 3D-island growth, while the smoothing of the Ti layers can be attributed to 2D-layer growth.

The growth models are just a simplification and do not fully explain how a structure like a MAX phase forms. Growth of this relatively complicated structure requires step flow or a high mobility of the atoms in the uppermost atomic layers. It seems that the attempts to grow Ti₄AlN₃ in *Paper 7* did not succeed because the structure requires 4 layers of Ti and 3 layers of N between every Al layer (see Figure 7(b)), and the temperature was too low for a high enough mobility to achieve the correct partitioning and positioning of the different atoms over the depth of a unit cell. An increase in temperature, however, led to Al diffusion out of the film and to a phase mixture of Ti₂AlN and Ti_{1-x}Al_xN.

5.3 THE DEPOSITION SYSTEMS

Two different deposition systems have been used for this Thesis. In Linköping, a UHV system is used for MSE depositions, and at the synchrotron in Grenoble a HV system is mounted onto a goniometer and used for *in situ* X-ray studies during deposition and annealing. The deposition systems including some comparisons between them are presented below.

5.3.1 MAGNETRON SPUTTER EPITAXY IN RAGNARÖK

The thin films that were grown in Linköping, were deposited by reactive MSE in the UHV deposition system named *Ragnarök*, seen in Figure 19. A base pressure of $\sim 10^{-9}$ Torr is achieved after baking the chamber at 180 °C for 48 h and running a large turbo molecular pump at full speed. Even better vacuum can be reached by using a Ti-sublimation pump, but I have never found it necessary due to the already low amounts of impurities in the films. Ragnarök features up to four magnetrons, tilted 30° from the vertical axis, with two 50 mm diameter and two 75 mm diameter sputtering targets. The magnetrons have a strong type II configuration, so that the plasma density is increased close to the substrate. I have mainly used 75 mm diameter targets for all elements except for Sc. The attempts to upscale even the Sc source resulted in films with very high amounts of F, a problem that remains to be solved. In Ragnarök, the working gas Ar and the reactive gas N₂ both have a purity of 99.999999%. The chamber enables substrate rotation with variable speed, to ensure that the films are deposited uniformly both in thickness and composition. The substrate is indirectly heated up to a maximum temperature of ~ 1300 °C by a BN-covered graphite heater, which is mounted ~ 1 cm behind the substrate. The temperature is controlled by a thermocouple positioned behind the substrate and calibrated with a pyrometer. An electrical substrate bias can also be applied to increase or decrease the ion-assisted growth.

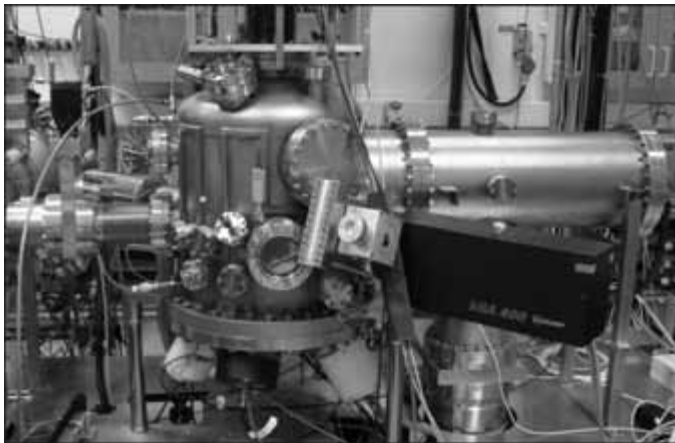


Figure 19: The UHV deposition chamber named Ragnarök, which is used for reactive MSE depositions in *Paper 1*, *Paper 2*, *Paper 4*, and *Paper 6*. The volume of the main chamber is ~ 35 dm³.

5.3.2 *IN SITU* X-RAY DIFFRACTION AT THE ESRF

To be able to *in situ* follow growth and annealing of the films in *Paper 3*, *Paper 5*, and *Paper 7*, I have visited the European Synchrotron Radiation Facility (ESRF) for altogether five weeks of beam times. A schematic and 3D-model of the HV deposition chamber, which is mounted onto a goniometer of the ROBL beamline (BM20), is shown in Figure 20. The chamber has Be-windows, which are close to transparent for X-rays. The standard measurement during deposition is time resolved X-ray interference. After each deposition or annealing step, X-ray diffraction and X-ray reflectivity scans were recorded. The techniques are further described in Section 6.2. The base pressure reaches $\sim 10^{-6}$ Torr after a few hours of pumping. Two magnetrons with 25 mm diameter targets are facing the substrate with a 30° angle. The sample holder is mounted in the rotation center of the goniometer and enables electrical biasing and heating of the substrate to $\sim 1100^\circ\text{C}$. The temperature is measured with a *K*-type thermocouple and the temperature has been calibrated both with a pyrometer and by melting different metal pieces.

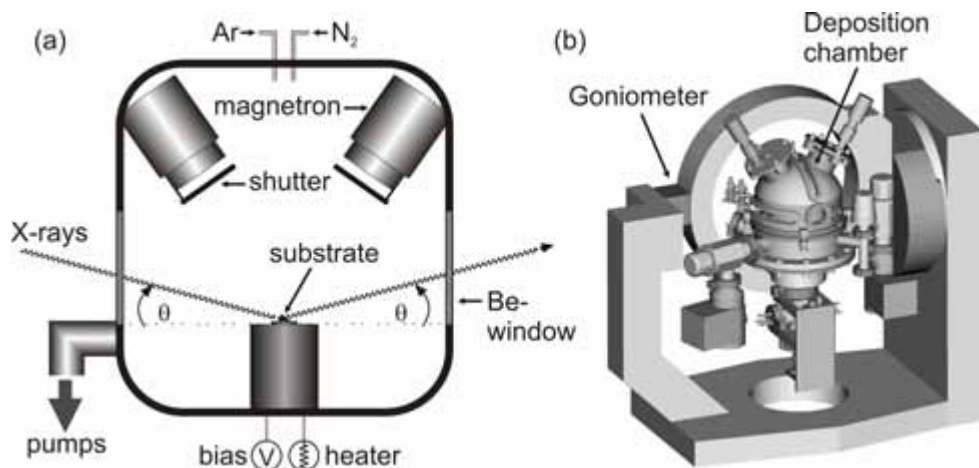


Figure 20: A (a) schematic and (b) 3D-model of the magnetron sputter deposition chamber at the ESRF, ROBL beamline (BM20) with the possibility to do *in situ* X-ray diffraction measurements. The volume of the chamber is $\sim 4\text{ dm}^3$.

Even though the heater temperatures in the two deposition chambers are calibrated in a standard way, the temperatures seem to differ between them. For unknown reason, the solid

state reactions in *Paper 5* occurs at 500 °C in the ROBL chamber and at 650 °C in Ragnarök. A similar situation occurs for Ti₂AlN growth. At Linköping University a temperature of 830 °C is needed for Ti₂AlN(0001) growth,⁵ at the ESRF in Grenoble the required temperature is 675 °C,⁶ and at the University of Illinois, USA, it is 1050 °C.¹²⁷ Of course, there are many differences between the deposition conditions in the three experiments, but an as-measured temperature variation of 375 °C is remarkable. Even though proper temperature calibrations have been performed for all three deposition systems, only heater temperatures within the same system are reasonable to compare.

6. ANALYSIS TECHNIQUES FOR THIN FILMS

The films in this Thesis are mainly subject of structural and compositional characterization, to get a fundamental understanding of the materials, and less for measurements of i.e. electrical and mechanical properties. The main techniques are based on ion beam analysis, X-ray diffraction, and transmission electron microscopy, which are described below.

6.1 ION BEAM ANALYSIS TECHNIQUES

Ion beam analysis is used for determination of the concentration of specific elements in a sample. Thickness, compositional gradients and depth positions of different elements can also be determined.

Ion beam analysis consists mainly of four techniques, which are illustrated in Figure 21. Rutherford backscattering spectroscopy (RBS) and elastic recoil detection analysis (ERDA) are based on elastic scattering of incoming ions. The ions lose a specific amount of energy and in RBS the energies of the scattered incoming ions are detected, while in ERDA the energy of the sputtered target atoms is detected. RBS is suitable for depth profiling and analysis of thin films (up to ~500 nm) containing medium to heavy elements on light substrates. ERDA is good for depth profiling and analysis of elements with a mass smaller than the mass of the incoming heavy ions. Nuclear reaction analysis (NRA) makes use of excitation of nuclei by the incoming beam, followed by relaxation and emission of γ -rays or particles. NRA is used for depth profiling of light elements, like H, in heavier substrates. In particle induced X-ray emission (PIXE) the target atoms are excited by the incoming beam and when they return to their ground state element characteristic X-rays are emitted. PIXE is used for determination of trace elements in a matrix of light elements.^{128,129}

The elemental sensitivity clearly varies between the techniques, but the sensitivity also differs between elements within the same technique. In RBS, elements with $Z < 70$ can be detected within ~0.1 at.%, while the sensitivity is better for heavier elements. For ERDA the sensitivity is ~0.1 at.%, but slightly higher for H. Both for NRA and PIXE the sensitivity is between ppm and percent, depending on elements. In the present setup we measure the relative concentrations of elements, and the estimated error is ~1% in RBS and ~2% in ERDA.

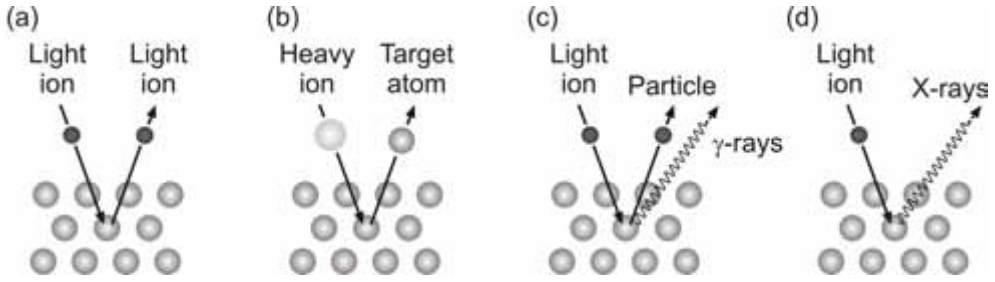


Figure 21: Schematic figure showing the difference between (a) RBS, (b) ERDA, (c) NRA, and (d) PIXE.

All the mentioned techniques are nondestructive, fast, quantitative, have a high sensitivity and no sample preparation or material specific reference samples are needed. Disadvantages include the need for an accelerator and special detectors, and lengthy evaluation.

6.1.1 ION-SOLID INTERACTIONS

ERDA and RBS are the techniques usually used for thin film analysis of samples like the ones in this Thesis. They are both based on the elastic scattering that occurs when an incoming light ion (RBS) or heavy ion (ERDA) primary beam hits a sample, see Figure 22. In both cases classical two-particle scattering theory is valid, which means that the momentum and the energy must be conserved during a collision. The incoming atom of mass m_0 , energy E_0 and velocity v_0 hits a sample atom of mass m_2 that is scattered with the angle φ and obtains the energy E_2 and velocity v_2 . The incoming atom is scattered with the angle θ and has the energy E_1 and velocity v_1 after the collision. It is a sufficient approximation to assume that all the scattering processes are binary and completely elastic.^{129,130,131}

The momentum conservation of the collision can then be described with

$$m_0 v_0 = m_0 v_1 \cos \theta + m_2 v_2 \cos \varphi, \text{ and} \quad (6.1)$$

$$0 = m_2 v_2 \sin \varphi - m_0 v_1 \sin \theta. \quad (6.2)$$

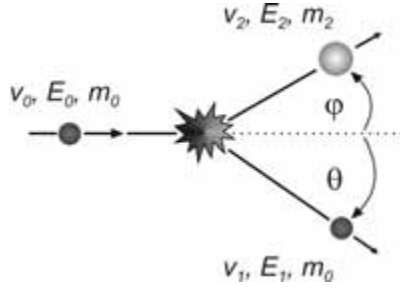


Figure 22: Collision kinematics: Classical two-particle scattering when an atom with mass m_0 collides with an atom of mass m_2 .

The energy is also conserved, yielding

$$E_0 = E_1 + E_2, \text{ and} \quad (6.3)$$

$$\frac{m_0 v_0^2}{2} = \frac{m_2 v_2^2}{2} + \frac{m_0 v_1^2}{2}. \quad (6.4)$$

These formulas can be used for deriving the kinematic factor K in RBS, which is the energy fraction of the incoming ion after a collision. The fraction $1-K$ is the energy transferred to the target atom.¹²⁹ K is given by

$$K_{proj} = \frac{E_1}{E_0} = \left[\frac{\sqrt{m_2^2 - m_0^2 \sin^2(\theta)} + m_0 \cos(\theta)}{m_0 + m_2} \right]^2, \quad (6.5)$$

where $\frac{m_2}{m_1} \geq 1$.

The kinematic factor k for the recoil atoms in ERDA can be derived in a similar way, yielding

$$k_{recoil} = \frac{E_2}{E_0} = \frac{4m_0 m_2}{(m_0 + m_2)^2} \cos^2(\varphi). \quad (6.6)$$

6.1.2 RUTHERFORD BACKSCATTERING SPECTROSCOPY

RBS is a method which is widely used for composition analysis and profiling of thin films to a depth of ~ 500 nm. Light ions, usually He^+ or H^+ , are elastically backscattered from the target atoms in the sample. Elements between Be and U can be detected, but the possibility to quantify each element depends on the combination of elements in the film and substrate. In Figure 23 a typical RBS setup together with the definition of angles and energies is shown.

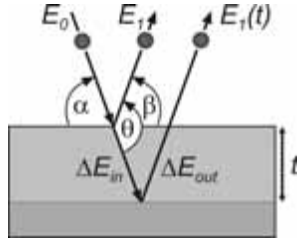


Figure 23: The RBS setup, including a definition of angles and energies.

The ions with highest energy have been backscattered by the heaviest element on the film surface. The energy is given by

$$E_1 = K_{proj} E_0. \quad (6.7)$$

The energy from an ion scattered by an atom deeper in the film also loses energy by interaction with electrons before and after scattering. This energy can be calculated by

$$E_2 = K_{proj}(E_0 - \Delta E_{in}) - \Delta E_{out}, \quad (6.8)$$

where ΔE_{in} and ΔE_{out} denote the energies that the incoming ions lose when traveling in and out a depth t of the sample, respectively, see Figure 23. These calculations are usually not trivial since ΔE depends on the element and its energy-specific stopping power.¹²⁹

While the kinetic factor determines the energy, the backscattering yield of an element determines its detected intensity or signal height in the full spectrum. A relative height of a spectrum, σ_{rel} , can be calculated for a known atomic number of element x . If the atomic number of the heaviest element in the film Z_{max} is known, then

$$\sigma_{rel} = \left[\frac{Z_x}{Z_{max}} \right]^2. \quad (6.9)$$

With more than one element in the film the backscattering yield $Y_{rel,x}$ scales with the amount of each element (x_{rel} , between 0 and 1) as

$$Y_{rel,x} = \sigma_{rel} x_{rel}. \quad (6.10)$$

A typical RBS spectrum (2.0 MeV He⁺ beam, $\alpha = 6^\circ$, $\beta = 7^\circ$, $\theta = 167^\circ$) is presented in Figure 24. The detector channel number is via the energy calibration related to energy, and plotted versus the number of He⁺ ions counted in the detector. The shown RBS spectrum stems from a Sc_{0.46}Al_{0.32}N_{0.22} film and ScN seed layer on an MgO substrate. The edge **1** arises from Sc at the surface of Sc-Al-N because Sc is the heaviest element in the film. The deeper in the film the ions are scattered by Sc, the lower is the energy they have. The spectrum thus goes to **2**, where the interface to ScN can be seen. A higher Sc signal at **3** indicates that ScN has a higher Sc-concentration than Sc-Al-N. Edge **4** and **5** originate from the Al at the film surface and interface to ScN, respectively, due to Al being the second heaviest element in the film. Due to that Mg from the substrate is heavier than N in the ScAlN film and ScN seed layer, their signals are overlapping and the Mg from the interface is seen at **6** while the N appears at **7**.

The evaluation of the RBS spectrum was usually done with the SIMNRA software.¹³² After energy calibration for the surface edge of some atoms of different mass in the surface layer the film spectrum can be simulated. This can be more or less time consuming depending on the atomic distribution in the film. It typically takes one day to evaluate a standard batch of 20 samples.

The simulated spectrum deviates from the measured one at low energies, see **8** in Figure 24, because multiple scattering occurs and the simulation program SIMNRA uses a binary collision approximation, as was introduced in Figure 22.

The output from simulations of RBS spectra are areal densities of each element. However, the thickness of a film can be obtained from ion beam analysis if the gravimetric density ρ is known (often the bulk density is more or less correct). The thickness t in meters can be calculated by inserting the areal density given in atoms/cm² as x , the relative mass M , and Avogadro's number N_a into

$$t = \frac{x \cdot M}{\rho \cdot N_a}. \quad (6.11)$$

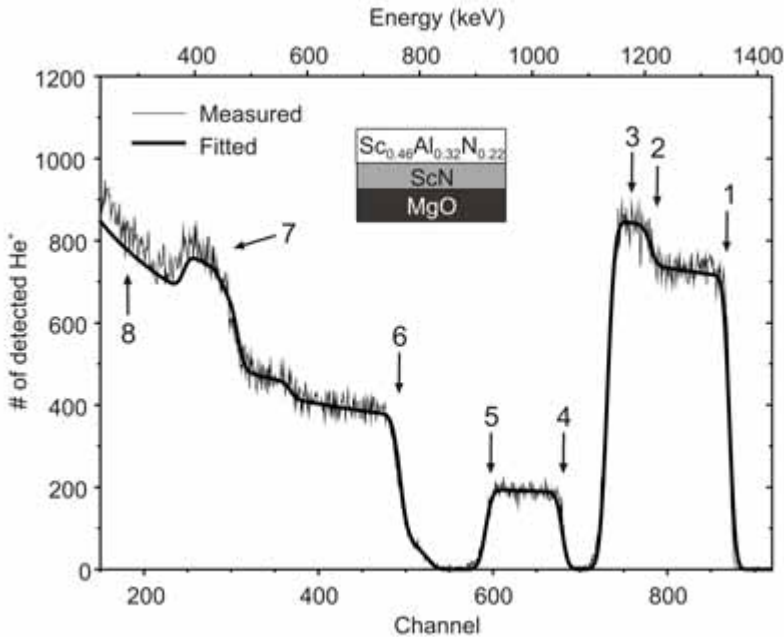


Figure 24: RBS spectrum from a Sc-Al-N film on MgO capped with a ScN seed layer.

To achieve a better separation of elements in, e.g., multilayers, the angle or the mass of the incoming beam can be increased, usually resulting in a lower count rate and noisier spectrum.

I have used the RBS technique regularly in my research. All the rate calibrations leading to right stoichiometries were done with RBS. In *Paper 5* RBS was used to confirm that the as-deposited AlN and Ti layers were stoichiometric and without intermixing. It was also used to see that annealing led to interdiffusion between the layers and intermixing of Ti, Al, and N. In *Paper 7* RBS was used to check for stoichiometry changes when depositing with the same parameters at different substrate temperatures. To make sure that no interdiffusion between the layers had occurred during annealing of the films in *Paper 3*, RBS measurements were performed.

With the substrates used in the different papers it has always been necessary to calibrate the absolute spectrum height according to the substrate. The N content is estimated as 100 at. %

minus all the heavy elements and presupposes a low C and O content. In this Thesis, ERDA was used to quantify the amount of N relative to other light elements.

6.1.3 CHANNELING RBS

In channeling RBS the incoming ion beam is aligned along a crystal axis of the sample so that atoms in deeper layers of the sample are shadowed by each other from the beam. This can, for example, be applied for measurements of very thin amorphous or defected crystals on single-crystal substrates where the light elements overlap with the substrate. The alignment of the crystal will lower the intensity coming from the substrate and thereby increase the intensity detected from the film. Channeling RBS can also be used for thick epitaxial layers to check for the amount of impurities or lattice disorder.^{129,130} Channeling RBS has not been used particularly here, but might be a good option to use for future measurements on single-crystal samples.

6.1.4 ELASTIC RECOIL DETECTION ANALYSIS

The possibility to measure light elements with RBS is limited and it is not possible to detect H. Instead, a forward scattering technique like ERDA can be used. With ERDA it is also possible to quantify the amount of light elements in a film on a heavy substrate. All elements lighter than the incoming beam can be detected, in a depth range of up to $\sim 1 \mu\text{m}$ for the 40 MeV iodine beam used for experiments in this Thesis. A typical ERDA spectrum is shown in Figure 25. In comparison to RBS, where the incoming ions are backscattered, the incoming heavy ions knock out lighter target ions which are detected as a function of energy and mass.

Most of the theory in RBS is also valid for ERDA. The major difference is the way recoil atoms are detected and identified. A detection setup that simultaneously obtains information from both the mass of the recoil atom and its energy is needed. A common type is the time-of-flight energy (ToF-E) setup, which distinguishes between atoms (mass m) of the same energy E due to their different velocities v according to

$$E = \frac{mv^2}{2} . \quad (6.12)$$

By measuring the time t it takes for an atom to move between two foils separated a distance L , the mass m is calculated with

$$m = \frac{2E \cdot t^2}{L^2} . \quad (6.13)$$

In contrast to RBS, heavier recoil atoms have a lower energy, but as in RBS the energy decreases deeper into the sample.

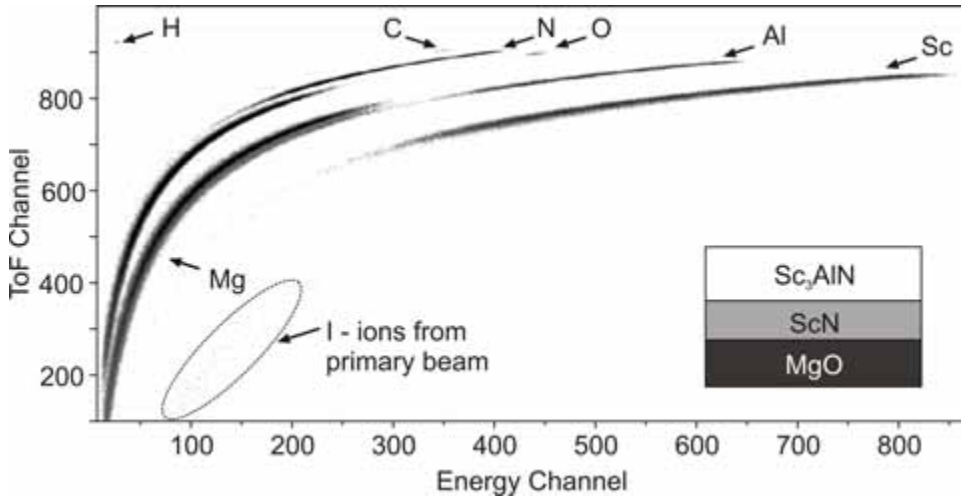


Figure 25: A typical ERDA spectrum from a Sc₃AlN film deposited onto a ScN seed layer and MgO substrate.

The evaluation of an ERDA spectrum requires, like RBS, a few samples with known surface elements for calibration. First the time-of-flight for different masses is calibrated, where the surface edge is specified for each element. Then the energy is calibrated with the same elements.

ERDA was used in *Paper 1* since the films were too thick to be measured with RBS. The depth profile in the paper illustrates nicely how evenly distributed the elements were in the film and how low the H, C, and O impurity levels were. In *Paper 2* and *Paper 3*, ERDA was used to see the amount of O in both as-deposited and annealed films. The depth

resolution in ERDA is much worse than for RBS, and most films in this Thesis are too thin to get good statistics. For those films RBS and ERDA are used simultaneously.

A problem that sometimes arises with both the RBS and ERDA techniques is that the results are average compositions from film areas which are at least $2 \times 2 \text{ mm}^2$. This means that if the film consists of several phases in nm-sized crystallites, like in *Paper 4*, normal ion beam analysis techniques will not be able to separate them.

6.2 X-RAY DIFFRACTION

X-rays have a wavelength of the same order of magnitude as the lattice constants in crystals (Ångströms). They are therefore well suited for characterization of materials' crystal structures. It is a popular technique, which does not require sample preparation (more than a clean surface), is non-destructive, and without need for lengthy evaluations.

The X-rays used for this Thesis are either generated in an X-ray Cu-tube or in a synchrotron with a far greater intensity. In a Cu-tube electrically charged particles are accelerated onto a Cu-plate from where the X-rays are emitted. With a Ni-filter only the Cu K_α -radiation is filtered out, giving a wavelength of 1.54 \AA . The synchrotron radiation is produced by accelerated electrons that move along a curved path within a deflecting magnetic field. A radiation range from microwaves to hard X-rays is produced, yielding a possibility to choose wavelengths for measurements.¹³⁴

When X-rays are scattered by a periodic crystal they will interfere constructively and thereby give rise to intensity peaks. The requirements for constructive interference are given by Bragg's law,

$$n\lambda = 2d \sin \theta, \quad (6.14)$$

where n is an integral number of the wavelength λ , d is the lattice plane distance, and θ the scattering angle.

Bragg's law says that the pathway difference between two atomic layers is $2d\sin\theta$, yielding an intensity maximum for an integral number of wavelengths, see Figure 26.¹³⁵

The way the X-rays will be scattered is dependent on the structure factor and multiplicity of the crystal planes, yielding different intensities for the diffracted beam. If randomly oriented crystallites in the sample are smaller than 2-5 nm they may not be possible to detect due to a severe peak broadening and the structure is then called *X-ray amorphous*.¹³⁶

The user should then consider using another technique, like transmission electron microscopy, to fully discard crystallinity.

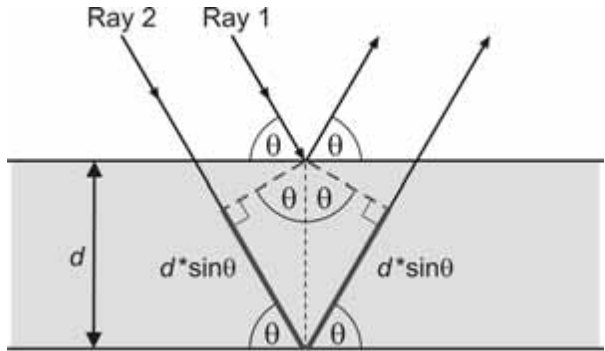


Figure 26: A schematic view of diffraction according to Bragg's law.

The most common use of X-ray diffraction (XRD) is for phase-, texture-, and stress analysis of polycrystalline materials. In the present work the substrates are single-crystals and the films are epitaxial. From such materials, the information gained with XRD is about phases, thickness, roughness, and texture. If a film consists of an unknown phase, like in *Paper 1*, XRD is an important technique to gain information about lattice parameter, crystal structure, and texture. For the *in situ* XRD work in *Paper 3*, *Paper 5* and *Paper 7*, the X-rays are also used for determination of the thickness, phase, and roughness evolution during film growth and in annealing studies. A schematic view over the tilting possibilities of the samples in the diffractometers used in this work is shown in Figure 27.

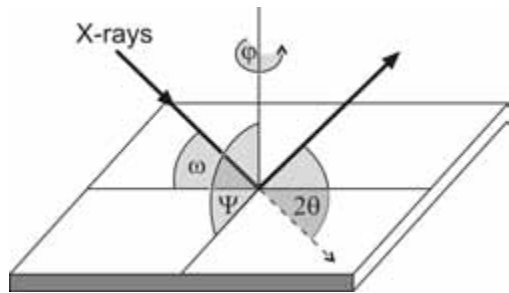


Figure 27: Schematic of the XRD setup showing the applied tilting possibilities of a sample.

6.2.1 X-RAY DIFFRACTION

In a so-called symmetric $\theta-2\theta$ diffraction scan only the specular reflections originating from lattice planes parallel to the sample surface are revealed. The positions of the peaks are used to identify the phases and the texture in the studied films. The full width at half maximum (FWHM) of a peak is an indication for the grain size in the film.

In some crystal structures, diffraction on planes with Miller indices hkl gives destructive interference, i.e., no peak intensity due to the structure factor of the material. This was used in *Paper 1*, where the perovskite Sc_3AlN (with no forbidden peaks) can be distinguished from the face centered cubic structure ScN and MgO (with peak intensity only for all hkl being even or odd). For this, non-specular $\omega-2\theta$ scans were made around all hkl . The setup for such scans is asymmetric and a tilt in φ and Ψ is necessary. Here, all phases yielded intensity for all allowed fcc crystal hkl values and only Sc_3AlN gave peaks corresponding to the other hkl values. The intensities from the perovskite peaks were very low, but their relative heights agreed with the calculated structure factor.

In *Paper 3*, symmetric $\theta-2\theta$ diffraction was the most important technique to *in situ* follow the phase separation of $\text{Sc}_{1-x}\text{Al}_x\text{N}$ and $\text{Ti}_{1-x}\text{Al}_x\text{N}$ films into their binaries. After each scan it was clearly seen if any phase transformation had occurred or if a further increase in temperature was needed. I encountered some problems, however, when using $\theta-2\theta$ diffraction for phase determination in *Paper 4*. The severe peak overlaps between $w\text{-AlN}$ seed layers and $w\text{-Sc}_{1-x}\text{Al}_x\text{N}$ films made it impossible to draw conclusions about the crystalline quality of $w\text{-Sc}_{1-x}\text{Al}_x\text{N}$. Instead, analytical transmission electron microscopy techniques had to be used.

6.2.2 POLE FIGURES

Pole figures can be used to find out more about the preferred orientation, or texture, in a film. Before recording a pole figure the exact position in θ and 2θ for the expected peak needs to be determined. During measurement the sample is scanned in both $\Psi(0-90^\circ)$ and $\varphi(0-360^\circ)$, revealing a view over all sample orientations yielding intensity for the set 2θ angle. A measurement like this gives the symmetry of the crystal and is used as a help to identify a certain crystal structure. In Figure 28, pole figures from two different plane spacings in Sc_3AlN in *Paper 1* are shown. They clearly show the three-fold symmetry of

200 and 111 reflections, exactly as expected from a cubic film grown on a cubic ScN(111) seed layer.

Determining the crystal symmetry from a pole figure is often not trivial. If there are no expected θ and 2θ positions, e.g., due to an unknown crystal structure like in *Paper 3*, one pole figure for all possible d -spacings should be recorded. This can be a very lengthy procedure if the equipment is not suited for it or the scattered intensity from the material is low. Stereographic projections (mentioned in Section 4.1.2) are a helpful tool for setting up and evaluating results from a pole figure experiment.

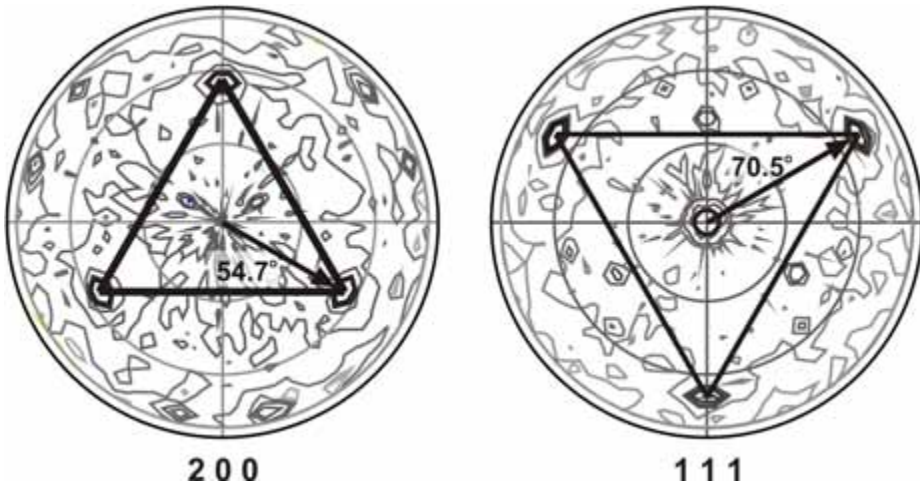


Figure 28: Pole figures from the Sc_3AlN perovskite in *Paper 1*. The angular position of the reflections agree with the expected ones from a cubic structure grown along the $[111]$ direction.

6.2.3 X-RAY REFLECTIVITY

X-ray reflectivity measurements are recorded in a symmetrical setup, at low θ and 2θ angles, and are based on the reflections of X-rays from surfaces and interfaces. These measurements are mostly used for thickness determination, but also to check for roughness of the film. In this Thesis, two different reflectivity techniques are used, namely *X-ray reflectivity (XRR)* and *time resolved X-ray interference*.

The film thickness can be determined by the modified Bragg's law, which takes into account the grazing incidence angle θ offset, caused by refraction in the material.

$$n\lambda = 2D \sin \theta \sqrt{1 + \frac{\eta^2 - 1}{\sin^2 \theta}}, \quad (6.15)$$

where D is the thickness and η is the complex refractive index of the film.

In XRR, a symmetrical $\theta - 2\theta$ scan is recorded at 2θ angles between ~ 0.5 and $\sim 5^\circ$. Each intensity maxima n corresponds to constructive interference from the path way difference of the X-ray beams, which are scattered at the substrate and film surface.

By plotting n^2 against $\sin^2 \theta$, the slope of the linear curve can be used for determining the optical thickness. When depositing the different layers in *Paper 5* an XRR scan was taken after each deposition. Every added layer added a unique phase shift of the X-rays which, together with X-rays reflected from previous layers, significantly altered the reflectivity curve. The evaluation of an irregular multilayer structure like this requires computer simulations. Depending on the shape of the decrease of the curve at increasing θ angles conclusions about the roughness can be drawn.

Time-resolved X-ray interference data are recorded to follow the thickness and roughness evolution during film growth. Fixed θ and 2θ angles are chosen and the number of counts in the detector with respect to deposition time is recorded. Again, the intensity oscillations originate from the constructive and destructive interference when X-ray beams are scattered at the substrate and film surface. When the film thickness D is such that the pathway difference is an integer number of wave lengths, the beam will interfere constructively, according to modified Bragg's law.

In Figure 29 the time-resolved X-ray interference graph from *Paper 5* is redrawn. A roughening of the film surface, compared to the extremely smooth $\text{Al}_2\text{O}_3(0001)$, leads to a steep decrease in the oscillation maxima, as seen in Layer 1. The decay at fixed angles is linked to a decreasing intensity in the corresponding XRR scan.

In addition, the X-ray beams are scattered at monolayers on the film surface to interfere constructively and destructively.¹³⁸ A symmetric oscillation intensity decrease, as seen in Layer 3 in Figure 29, is typical for roughening on the monolayer scale, while the oscillation amplitude increase in Layer 2 is typical for smoothening. The oscillations are only observable for very smooth layers, like during layer-by-layer growth, where the surface roughness is only a few monolayers.

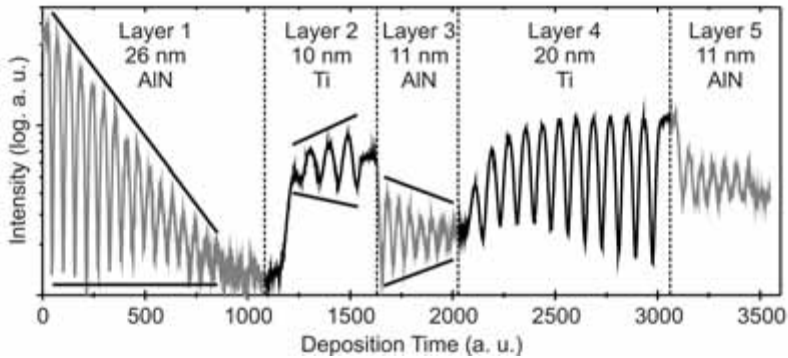


Figure 29: Time resolved X-ray interference data recorded during deposition of AlN/Ti multilayers in *Paper 5*, see also Figure 14 for the layer architecture.

In *Paper 5* each AlN layer roughened the surface due to the relatively low ad-atom mobility on the AlN(0001) surface at a growth temperature of 200 °C. Each Ti layer smoothed the surface again, due to weak bonding on the Ti(0001) surface implying a high ad-atom mobility.

6.3 TRANSMISSION ELECTRON MICROSCOPY

The wavelength of visible light limits the image resolution in light microscopes, which was the main reason for developing electron microscopes that use the wave nature of highly energetic electrons instead of light. For materials science and especially thin film research, this has been revolutionary due to the possibility of imaging samples with a resolution of $<1 \text{ \AA}$, which means that it is possible to image the atomic arrangement in a material. What limits the resolution is not the wavelength, but apertures, aberration in lenses, and the inelastic scattering processes in the samples.

A TEM consists in principle of an electron gun emitting an electron beam, two or more electromagnetic lenses condensing the beam on the sample, an imaging lens system collecting the transmitted and scattered beams, and lenses projecting the image on a screen or into a CCD camera.¹⁰⁷

There are two different mechanisms that yield contrast in a TEM image; *amplitude contrast* (which is divided into *mass-thickness contrast* and *diffraction contrast*) and *phase contrast*.

Mass-thickness contrast arises when electrons are elastically and incoherently scattered by atoms in the sample. The scattering is dependent on the atomic mass, the density, and the thickness of the sample. The higher the mass and density of the material and the thicker the sample, the more scattering will occur. This contrast mechanism is especially important for non-crystalline materials. Mass-thickness contrast was in this Thesis used for images taken at low magnification, where no effort was put into aligning the crystal. Mass-thickness contrast dominates in the so-called *bright-field mode*.¹⁰⁷

Diffraction contrast occurs due to coherent elastic scattering of electrons at certain Bragg angles in crystalline materials. Alignment of the sample (or the electron beam) along certain crystal zone axes is required. Diffraction contrast images are taken in *dark-field mode*. I have used diffraction contrast in overview images, to see that the films consist of equally oriented crystallites.¹⁰⁷

Phase contrast is the contrast mechanism used in high resolution imaging and requires more than one beam. The contrast arises from the pathway difference between the beams, when one of the beams is scattered. The pathway changes due to a phase shift of the scattered beam, but can also be due to, e.g., scattering factors, orientations, or thickness variations. Phase contrast is in this work mainly used to study the structural periodicity in a crystal. In an aligned sample, lattice fringes originating from phase contrast show up. They give information about lattice spacing in the crystal, but it is important not to interpret them as direct images of the structure. Moiré fringes also arise from phase contrast effects, and show up when two differently aligned crystallites overlap along the electron path.¹⁰⁷

6.3.1 HIGH-RESOLUTION TRANSMISSION ELECTRON MICROSCOPY

In high-resolution TEM (HRTEM) it is possible to image the lattice of a material. To achieve high quality images an accurate alignment is required, both of the beam and of the sample. Some characteristic features for certain crystalline structures can be seen in HRTEM and help identifying the crystalline phase. An example can be found in Figure 3 in *Paper 7*, where a clear difference is seen between the small d -spacing in the cubic solid solution of $\text{Ti}_{1-x}\text{Al}_x\text{N}$ (111) compared to the significant layering of the (0001) planes in the Ti_2AlN MAX phase.

The objective lens in a TEM suffers from spherical aberration, chromatic aberration, and astigmatism, which limits the resolution at very high magnifications. The FEI TITAN microscope at Forschungszentrum Dresden-Rossendorf used in *Paper 1* has a corrector for

spherical aberration making it possible to get images with an even higher resolution (1.0-1.1 Å) than the ones achieved in the FEI Tecnai G² TF 20 UT at Linköping University (1.9 Å) used for all other images.

6.3.2 SCANNING TRANSMISSION ELECTRON MICROSCOPY

Scanning Transmission Electron Microscopy (STEM) mainly differs from a conventional TEM (with a parallel μm -sized electron beam) in that the electron beam is focused into an atomic sized probe. The probe is scanned across an area of the sample, like in a scanning electron microscope (SEM). The image is then constructed by the scattered intensity at each scanning point. Higher magnification is achieved by decreasing the area size and increasing the number of pixels. STEM imaging was the key technique in *Paper 4* to prove that wurtzite $\text{Sc}_{1-x}\text{Al}_x\text{N}$ phase separates at ScN concentrations higher than $\sim 22\%$. *Z contrast* was used to form the image. This is an imaging mode which is based on mass-thickness contrast and uses that single atoms scatter electrons elastically and incoherently. The higher the mass of the atom is, the more the electron will be scattered.¹⁰⁷

6.3.3 ENERGY DISPERSIVE X-RAY SPECTROSCOPY

Energy dispersive X-ray spectroscopy is a chemical characterization technique which uses the characteristic X-rays that are emitted from the sample when it interacts with the electron beam. If the high-energy beam electrons interact with a core electron of an atom in the sample, and the energy is high enough, the core electron will be ejected and leave a hole in the inner shell. The atom is consequently excited and for it to return to the ground state the core hole must be filled by an electron from an outer shell. This is accompanied by the emission of an X-ray. The fact that the X-ray is characteristic in the difference in energy between the involved electron shells and is unique for each atom is used to identify the positions of different elements in the sample. EDX mapping is done in STEM mode in the TEM, and the characteristic X-rays at each scanning point are used to form the image. EDX mapping was successfully used in *Paper 3* to show the local atomic distribution in as-deposited cubic $\text{Sc}_{1-x}\text{Al}_x\text{N}$ in comparison to when the material was phase separated into ScN and AlN.¹⁰⁷

6.3.4 ELECTRON DIFFRACTION

In the electron diffraction mode, like in XRD, the reciprocal lattice is imaged. When the electron beam passes through the specimen, the electrons are scattered. The way scattering will occur, depends on the structure of the sample. Electron diffraction is therefore a useful tool for getting lattice structural information. Due to the small wave length of the electrons (in the pm-range) and the small sampling volumes, features from samples that are supposed to be X-ray amorphous can show up in electron diffraction. To limit the information to come from a certain area of the sample, like from a small area or single grain, an aperture can be inserted in the image plane of the objective lens. This technique is called *selected area electron diffraction* (SAED) and has been an important tool in most included papers. For example, SAED was used in *Paper 1* to test that the phase was indeed a perovskite and that the film was a single-crystal. Both bright and weak spots were observed, which agreed with the structure factor of a perovskite. In *Paper 2*, SAED was the technique that helped solving the different epitaxial relations between the ScN seed layers and $\text{Sc}_{1-x}\text{Al}_x\text{N}$ films. More about diffraction patterns is written in Section 4.1.2.

6.3.5 SAMPLE PREPARATION

A TEM sample has to be thin enough to transmit the electron beam and still keep intensity while containing the materials structure of interest. A thin sample also minimizes the risk that any two grains overlap in depth or that the electrons are multiply scattered. This requires careful sample preparation. My samples are all cross-sectional samples, meaning that the whole thickness of a film can be studied, including any microstructural evolution. A TEM sample is prepared by gluing two samples with the films against each other into a Ti-grid, grinding it down to $\sim 50\ \mu\text{m}$ thickness followed by ion etching until there is a hole in the center. The extremely thin (1 – 100 nm) area next to the hole is used for imaging.

6.4 ELECTRICAL CHARACTERIZATION

Following structural and compositional characterization, the next task for a new material like Sc_3AlN in *Paper 1* is to measure its physical properties. Here, resistivity measurements were performed to find out whether it is conducting like the binary intermetallics or semiconducting like ScN and AlN. Since it is a perovskite and some of them are reported to be superconducting,⁸¹ even at temperatures of up to 120 K,⁸² we also measured the

temperature-dependent resistivity, from room temperature down to a few Kelvin. A van der Pauw setup at the University of Illinois, Urbana, was used instead of the four point probe that usually is used for resistivity measurements.

6.4.1 VAN DER PAUW RESISTIVITY MEASUREMENTS

The advantage with van der Pauw resistivity measurements is that the measurement can be done on a sample with arbitrary shape. Four small Pt-contacts were milled into half of the thickness of the film, preferably in a square ~ 5 mm apart, by focused ion beam, see Figure 30. On top of each contact a wire bonding was evaporated. A current was sent from contact a to c , the voltage was measured between b and d , and the resistance R was calculated. To get better statistics also a measurement with a current from a to b and a voltage from c to d should be done.¹⁴⁰

The sheet resistance R_s is given by

$$R_s = \frac{\pi \cdot R}{\ln 2}. \quad (6.16)$$

The resistivity ρ is then calculated by measuring the film thickness D and using

$$\rho = D \cdot R_s. \quad (6.17)$$

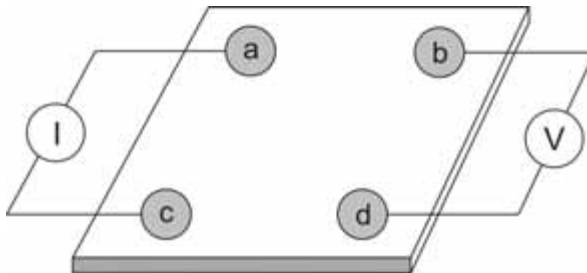


Figure 30: A van der Pauw measurement setup.

For the temperature-dependent resistivity measurements, the sample was cooled down to 4 K and the resistivity was continuously measured while the temperature increased to room

temperature. Initial results indicate that as-deposited $\text{Sc}_3\text{AlN}(111)$ films are not superconducting above 4 K.

6.5 MECHANICAL CHARACTERIZATION

6.5.1 NANOINDENTATION

Nanoindentation experiments are useful to find out about the mechanical properties of a thin film. During a measurement a sharp diamond tip is pressed into the surface of the material with a controlled load. By recording the displacement of the indenter during loading and unloading, see Figure 31, and employing the evaluation method developed by Oliver and Pharr,¹⁴¹ the hardness and reduced elastic modulus can be determined.

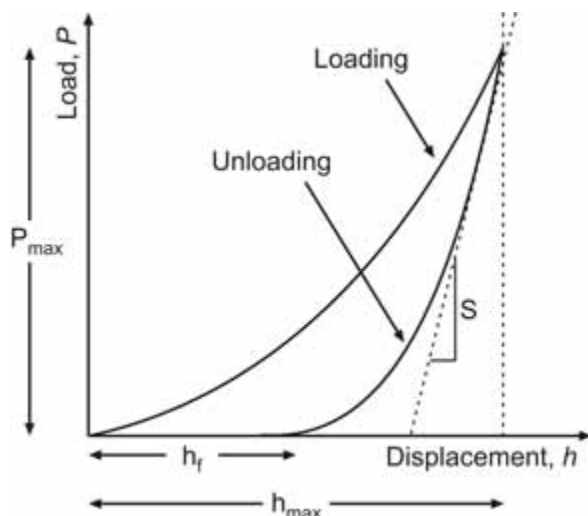


Figure 31: A schematic representation of load P versus indenter displacement data h for an indentation experiment, redrawn from Reference 141, where P_{\max} is the applied load, h_{\max} is the maximum displacement, and h_f is the resulting plastic deformation.

The reduced modulus E_r is given by the slope of the initial gradient when unloading ($S = dP / dh$), the contact area A and the equation

$$E_r = \frac{1}{2} \sqrt{\frac{\pi}{A}} \left(\frac{dP}{dh} \right). \quad (6.18)$$

The elastic modulus E_i and Poisson's ratio ν_i from the indenter have to be taken into account and the elastic modulus of the sample E can be calculated by

$$\frac{1}{E_r} = \frac{1-\nu^2}{E} + \frac{1-\nu_i^2}{E_i}. \quad (6.19)$$

In this Thesis nanoindentation was used in *Paper 1* to get a first hint about the mechanical properties of Sc_3AlN . The results yielded a hardness of 14.2 GPa and an elastic modulus of 249 GPa. This is lower than the reported hardness and elastic modulus of ScN, being 21 GPa and 356 GPa, respectively,¹⁴² and in the same range as for Ti_3AlC with values of 11 GPa and 240 GPa, respectively.¹⁴³

7.

SUMMARY OF RESULTS

7.1 THE Sc-Al-N SYSTEM

A considerable part of my Thesis has been to explore the Sc-Al-N system. Sc is a transition metal, next to Ti in the periodic table. Even though there has been much research going on regarding ternary nitrides with Ti, the Sc-Al-N system remains almost unexplored. Reference 44 reports about bulk Sc_3AlN in equilibrium with ScN, Sc, AlSc_2 , and AlSc . Except for that paper, there was essentially nothing published within the field until this work started. Here, I summarize my main results.

7.1.1 THE INVERSE PEROVSKITE Sc_3AlN

The aim with *Paper 1* was to explore the ternary Sc-Al-N phase diagram. It is found that the inverse perovskite Sc_3AlN can be deposited as a single-crystal thin film at 650 °C. Reactive magnetron sputter epitaxy from two targets under ultra high vacuum conditions was used to grow $\text{Sc}_3\text{AlN}(111)$ with $\text{ScN}(111)$ seed layers onto $\text{MgO}(111)$ substrates. Elastic recoil detection analysis shows Sc:Al:N composition ratios of 3:1:1 and an impurity level close to the detection limit.

X-ray diffraction was used for phase information. Pole figures and $\theta - 2\theta$ scans support that the film and seed layer have exclusively grown in the $\langle 111 \rangle$ -direction, show a cube-on-cube epitaxy, and reveal the lattice parameter of 4.40 Å. By non-specular $\omega - 2\theta$ scans it is possible to distinguish the face center cubic crystals ScN and MgO from the perovskite Sc_3AlN , detecting additional reciprocal lattice points unique for a perovskite.

Cross sectional transmission electron microscopy with selected area electron diffraction of the Sc_3AlN layers confirm the results and show that the film is single-crystal. High resolution C_s -corrected microscopy of the Sc_3AlN film along its [210]-zone axis reveals its characteristic layered structure, with Sc-N and Sc-Al layers.

Density functional theory calculations show that the perovskite Sc_3AlN is thermodynamically stable and that its theoretical lattice parameter agrees with the experiments.

Nanoindentation experiments of $\text{Sc}_3\text{AlN}(111)$ show a hardness of 14.2 GPa and an elastic modulus of 21 GPa. Resistivity measurements show a room temperature resistivity of $41.2 \mu\Omega\text{cm}$.

7.1.2 THE CUBIC $\text{Sc}_{1-x}\text{Al}_x\text{N}$ SOLID SOLUTION

The metastable cubic solid solution of $\text{Sc}_{1-x}\text{Al}_x\text{N}$ is expected to have excellent mechanical properties due to the similarities with related ternary transition metal nitrides, like $\text{Ti}_{1-x}\text{Al}_x\text{N}$. Two papers in this Thesis deal with cubic (c-) $\text{Sc}_{1-x}\text{Al}_x\text{N}$. In *Paper 2*, I determined the solid solubility of AlN in the material, while the main purpose with *Paper 3* was to experimentally compare the influence of two different driving forces for phase separation in c- $\text{Sc}_{1-x}\text{Al}_x\text{N}$ and c- $\text{Ti}_{1-x}\text{Al}_x\text{N}$, respectively.

Paper 2 showed that an Al molar fraction up to $x = 0.6$ can be dissolved into the metastable cubic disordered solid solution of $\text{Sc}_{1-x}\text{Al}_x\text{N}$. Reactive magnetron sputter epitaxy was used to deposit seven stoichiometric $\text{Sc}_{1-x}\text{Al}_x\text{N}$ films with $0 \leq x \leq 1$. Deposition parameters which would be optimal for c-ScN were used to, possibly, extend the limit for solubility in the cubic structure. The films were deposited from elemental Sc and Al targets onto $\text{MgO}(111)$ substrates with $\text{ScN}(111)$ seed layers at substrate temperatures of 600°C .

Rutherford backscattering spectroscopy and elastic recoil detection analysis were used to determine the compositions and to check for impurities in the films. The resulting AlN molar fractions of $x = 0, 0.14, 0.29, 0.51, 0.73, 0.90,$ and 1.00 , exhibit a linear dependence between the applied magnetron powers and resulting Sc-to-Al ratios. Sharp edges in the spectra show that there has been no interdiffusion between substrates, seed layers, and films.

X-ray diffraction shows a peak shift towards higher angles for increasing AlN content, corresponding to a decreasing lattice parameter. From X-ray diffraction determined lattice parameters agree well with Vegard's rule and with results from first principles calculations.

For $x \leq 0.51$, selected area electron diffraction shows a cube-on-cube epitaxial relationship between film and seed layer, with $\text{Sc}_{1-x}\text{Al}_x\text{N}(111) \parallel \text{ScN}(111)$ and $\text{Sc}_{1-x}\text{Al}_x\text{N}[1\bar{1}0] \parallel \text{ScN}[1\bar{1}0]$. For $x \geq 0.73$, the films clearly phase separate, resulting in diffraction patterns containing contributions from up to four epitaxial relationships to the seed layer. These are

(1) cube-on cube epitaxial contribution,

- (2) growth of film $(10\bar{1}1) \parallel \text{ScN}(111)$ and film $[\bar{1}2\bar{1}0] \parallel \text{ScN}[\bar{1}\bar{1}0]$,
- (3) growth of film $(0001) \parallel \text{ScN}(111)$ and film $[\bar{1}2\bar{1}0] \parallel \text{ScN}[\bar{1}\bar{1}0]$,
- (4) growth of film $(10\bar{1}1) \parallel \text{ScN}(113)$, without an unambiguous crystallite orientation.

Results obtained from electron diffraction, X-ray diffraction, ion beam analysis, and together with first principles calculations, show that a maximum molar fraction of 60% AlN can be dissolved into c-ScN.

The first principles calculations in Reference 48 show that the magnitude of the positive isostructural mixing enthalpy in the c-Sc_{1-x}Al_xN and c-Ti_{1-x}Al_xN systems appears very similar. However, there is a clear difference between the systems, due to that the electronic structure is the driving force for phase separation in Ti_{1-x}Al_xN, the effect is absent in Sc_{1-x}Al_xN. Therefore, the decomposition mechanisms in the two systems were expected to differ and originate in volume mismatch and electronic structure for Sc_{1-x}Al_xN and Ti_{1-x}Al_xN, respectively. In *Paper 3* the behavior during phase separation of the two materials was investigated.

In situ X-ray diffraction was used to follow the growth and subsequent annealing of epitaxial Sc_{0.57}Al_{0.43}N and Ti_{0.51}Al_{0.49}N thin films in a deposition chamber mounted to a goniometer at the European Synchrotron Radiation Facility (ESRF). The growth was performed with reactive magnetron sputtering at 675 °C and 600 °C for Sc_{0.57}Al_{0.43}N and Ti_{0.51}Al_{0.49}N, respectively, and the annealing was performed in vacuum to a maximum temperature of 1100 °C.

Rutherford backscattering spectroscopy and elastic recoil detection analysis shows that there is no significant change in composition between the as-deposited and annealed Sc_{0.57}Al_{0.43}N films. The as-deposited Ti_{0.51}Al_{0.49}N film contains a relatively high amount of oxygen and is even more oxidized during annealing.

In situ X-ray diffraction shows the first indications for phase separation of Sc_{0.57}Al_{0.43}N at 1000 °C. An increase to 1050 °C or 1100 °C is necessary to have the material fully decomposed into ScN and wurtzite-structure AlN within a few hours. Ti_{0.51}Al_{0.49}N shows the first steps of spinodal decomposition at 800 °C, a temperature that agrees with previous *ex situ* studies on a comparable materials system.⁴⁰ The phase separation of the material into TiN and c-AlN is complete at 1000 °C.

The phase separation of Sc_{0.57}Al_{0.43}N was further studied *ex situ* with energy dispersive X-ray spectroscopy maps, lattice resolved transmission electron microscopy, and pole figures. The results confirm the complete phase separation at 1100 °C and reveal that the

precipitated w-AlN domains are a few nanometers wide and have a topotaxial relationship to the surrounding ScN matrix, with $\text{AlN}(0001) \parallel \text{ScN}(001)$ and $\text{AlN}\langle 0\bar{1}10 \rangle \parallel \text{ScN}\langle \bar{1}10 \rangle$. The nucleation and growth type of phase separation in $\text{Sc}_{1-x}\text{Al}_x\text{N}$ (and the absence of isostructural decomposition) agree with conclusions drawn from first principles calculations of mixing energies versus lattice spacing curves.

7.1.3 THE WURTZITE $\text{Sc}_{1-x}\text{Al}_x\text{N}$ SOLID SOLUTION

Analog to the cubic $\text{Sc}_{1-x}\text{Al}_x\text{N}$ system I wanted to determine how much ScN that can be dissolved into wurtzite-structure (w-) AlN, while keeping it single-crystal. The material has recently drawn attention due to that it, for $x = 0.5$, is said to have a piezoelectric coefficient which is 400% higher than for pure w-AlN.⁴⁹

In *Paper 4*, magnetron sputter epitaxy was used to deposit a disordered $\text{Sc}_{1-x}\text{Al}_x\text{N}$ solid solution, starting from optimal conditions for wurtzite AlN. X-ray diffraction results show that the films were wurtzite and single-crystal for $0.78 \leq x \leq 1.0$. Both a and c lattice parameters agree with calculated ones.

Cross-sectional transmission electron microscopy (TEM) and selected area electron diffraction show that the $\text{Sc}_{0.06}\text{Al}_{0.94}\text{N}$ film has a single-crystal quality. Increasing ScN content to $x = 0.76$, yields an apparently deteriorated crystal quality and mass-sensitive imaging in scanning TEM mode shows strong indications for phase separation of the film into nanometer sized ScN and AlN rich domains. Films with $x = 0.28$, show the same cubic crystal structure as is seen in *Paper 2*.

First-principles calculations were performed on the mixing enthalpies of solid solutions in cubic, wurtzite, and hexagonal structures. They indicate that the rocksalt structure is the thermodynamically most favorable for $x \leq 0.45$, while higher AlN concentrations favor the wurtzite structure. Close to $x = 0.50$, all three structures are almost degenerate in energy. This is compared to the experimentally determined transitions from single phase to phase separated, for the cubic structure at $x = 0.60$ and for wurtzite structure at $x = 0.78$. The experimental results in *Paper 4* and *Paper 2*, together with mixing enthalpy calculations show how important growth kinetics is in comparison to thermodynamics, if a structural extension of the composition regime of phase formation is desirable.

7.2 THE Ti-Al-N SYSTEM

7.2.1 NEW ROUTES FOR Ti₂AlN MAX PHASE FORMATION

Understoichiometric nitrides, including the Ti₂AlN MAX phase, are tricky to deposit with reactive magnetron sputtering due to the very accurate nitrogen flow control needed. In addition, before this work the temperature needed for basal plane Ti₂AlN growth was 675 °C,⁶ and it has been an ambition to lower the deposition temperature. Here I summarize the results from two papers which present new ways of depositing Ti₂AlN, both based on solid state reactions. In *Paper 5*, Ti₂AlN(0001) was formed by a solid state reaction in an epitaxial Ti and AlN multilayer at a temperature as low as 500 °C, while deposition of TiN_x onto Al₂O₃ in *Paper 6* yielded the same phase with incorporation of oxygen.

The multilayer experiments resulting in *Paper 5* were carried out at the European Synchrotron Radiation Facility (ESRF) allowing X-ray scattering analysis *in situ* during depositions and annealing. Sequential layers of wurtzite-AlN(0001) and α-Ti(0001) were deposited by (reactive) magnetron sputtering from elemental Ti and Al targets onto Al₂O₃(0001) at 200 °C. Time resolved X-ray interference scans during deposition showed a decrease in the oscillation amplitude for AlN and an increase in the amplitude for Ti, indicating surface roughening and smoothening, respectively.

X-ray reflectivity scans were recorded to measure the thickness of each layer and to confirm that the surface of each layer is smooth. *Ex situ* Rutherford backscattering spectroscopy shows that the layers are stoichiometric to within 2 at.% and that there is no intermixing of the individual AlN and Ti layers.

After deposition of the layers, the sample was annealed and an X-ray diffraction scan was recorded every 30 min. At a temperature of 400 °C it is seen that perovskite Ti₃AlN forms within 5 min and the reaction is completed after 30 min. At 500 °C the Ti₂AlN phase forms within 5 min, after 30 min the perovskite vanishes and after 1 h the phase transformation to Ti₂AlN is completed with some residual AlN.

The paper suggests a sequence of steps for diffusion and phase transformation of the diffusion couples as illustrated in Figure 13. Ti is highly reactive at a temperature of 400 °C and has a large solid solubility in the α-phase. Therefore N interstitially diffuses into Ti, followed by substitutional diffusion of Al forming Ti₃AlN. The decomposition rate of AlN and the Al diffusivity are amplified at 500 °C. This makes it possible to add Al and N to Ti₃AlN, reorganizing the crystal structure, and forming Ti₂AlN.

The TiN_x films in *Paper 6* were deposited with reactive magnetron sputtering onto single-crystal $\text{Al}_2\text{O}_3(0001)$ substrates, in two series with varied temperatures and N_2 partial pressures, respectively. The results show that TiN_x react with the substrate, forming an oxygen containing $\text{Ti}_2\text{Al}(\text{O},\text{N})$ MAX phase.

In a temperature series, the N_2 partial pressure was kept constant at 0.2 mTorr, while the temperature was varied from 800 °C to 1000 °C. In a partial pressure series, the temperature was kept constant at 900 °C, while the N_2 partial pressure was varied between 0.1 mTorr and 1.0 mTorr.

X-ray diffraction was used to determine the crystalline phases in the films and their epitaxial relation to the substrate. The results from the N_2 series show that for a high enough N_2 partial pressure (in this case 0.2 – 0.3 mTorr) growth of $\text{Ti}_2\text{Al}(\text{O},\text{N})$ is possible through a solid state reaction of the understoichiometric TiN_x with the substrate. The MAX phase co-exists with Ti_2O , Ti_3Al and TiN_x . With N_2 partial pressures as high as 1.0 mTorr, instead, the thermodynamically more stable TiN forms. Varying the temperature from 800 °C to 1000 °C does not change the forming phases, but increases the surface mobility, resulting in a better crystalline quality.

Energy dispersive X-ray spectroscopy in combination with transmission electron microscopy was used to map out the distribution of Ti, Al, N, and O elements in the film and to point out the position of the different phases in the film. These techniques in combination with elastic recoil detection analysis show that the reaction of TiN_x with the substrate is less pronounced for higher N_2 partial pressures. A change in temperature does not influence the substrate reaction. Electron energy loss spectroscopy was the key technique to show that oxygen can be incorporated into Ti_2AlN , forming a $\text{Ti}_2\text{Al}(\text{O},\text{N})$ oxynitride MAX phase.

7.2.2 Ti_4AlN_3 THIN FILM GROWTH ATTEMPTS

Until now Ti_2AlN is the only MAX phase nitride reported as a thin film, but another MAX phase, Ti_4AlN_3 , is known from the bulk.⁶⁶ The aim of *Paper 7* was to explore the synthesis of Ti_4AlN_3 by thin film deposition. The influence of the substrate temperature was studied particularly, as it affects the Al mobility which, in turn, determines the composition, texture, and morphology during growth.

Ti-Al-N films, both with Ti:Al:N ratios of 2:1:1 and 4:1:3, were deposited onto $\text{Al}_2\text{O}_3(0001)$ substrates in a deposition chamber mounted to a goniometer at the European

Synchrotron Radiation Facility (ESRF). *In situ* $\theta-2\theta$ scans show that deposition of $4\text{TiAl}_3\text{N}$ at $675\text{ }^\circ\text{C}$ directly onto the substrate or with a Ti_2AlN seed layer yields a phase mixture of Ti_2AlN and $\text{Ti}_{1-x}\text{Al}_x\text{N}$ with x close to 0. At a temperature of $725\text{ }^\circ\text{C}$ the $\text{Ti}_{1-x}\text{Al}_x\text{N}$ peak intensity increases. When lowering the temperature to $600\text{ }^\circ\text{C}$ peaks show up, which can be attributed to high order Ti_4AlN_3 000 ℓ or tilted basal plane peaks.

Rutherford backscattering spectroscopy results show that depositions at $600\text{ }^\circ\text{C}$ yield Ti:Al:N ratios of 4:1:3, while higher temperatures result in an Al loss and O uptake. The Al loss is not observed in Ti_2AlN though. Therefore, it seems that Ti_2AlN is more stable than Ti_4AlN_3 at temperatures above $600\text{ }^\circ\text{C}$ at the deposition conditions used in this study.

Cross sectional transmission electron micrographs shows that the film deposited at $675\text{ }^\circ\text{C}$ consists of both Ti_2AlN and $\text{Ti}_{1-x}\text{Al}_x\text{N}$. The film deposited at $600\text{ }^\circ\text{C}$, however, has sections with pronounced hillock formations between smooth sections. Both sections show a layered structure with repeated twinning as in $\text{M}_{n+1}\text{AX}_n$, but without the periodicity of Ti_4AlN_3 . The Fourier transformations of the images correspondingly show streaks instead of individual spots, representing different $\text{Ti}_{n+1}\text{AlN}_n$ stacking sequences.

X-ray photoelectron spectroscopy sputter depth profiles were obtained and the N(1s) spectra all show a peak originating from Ti-N bonds in the samples and the Ti(2p) shows the corresponding typical nitride doublet peaks. The Al(2p) signal differs, however, significantly between the $\text{Ti}_{1-x}\text{Al}_x\text{N}$, with Al-N bonds, and Ti_2AlN and $4\text{TiAl}_3\text{N}$, with binding energies close to Al-Al bonds. This confirms the above finding that the $4\text{TiAl}_3\text{N}$ film contains mirror planes of Al as in a MAX phase, but without the periodical stacking.

In conclusion, Ti_4AlN_3 did not form by the present deposition processing. At temperatures above $600\text{ }^\circ\text{C}$, Al is lost to the vacuum and there is not enough left to form stoichiometric Ti_4AlN_3 . Lower temperatures prevent Al loss, but the Al ad-atom mobility is too small for growth of the periodic layers forming Ti_4AlN_3 . Instead competing film-forming reactions lead to Ti_2AlN with intergrown $\text{Ti}_{n+1}\text{AlN}_n$ structures.

8. CONTRIBUTIONS TO THE FIELD

I have increased the knowledge about functional ternary transition metal (TM) nitrides deposited in the form of thin films by reactive magnetron sputtering. Noteworthy is that TM-Al-N alloys with element 21 (Sc) and 22 (Ti) in the periodic table yield quite different phases and solid solutions.

Generally, I have...

- ... systematically studied Sc-Al-N and pioneered the thin film work in this system.
- ... developed two new ways for Ti_2AlN MAX phase growth, and shown that competing nitride formation can hinder Ti_4AlN_3 formation.
- ... demonstrated a powerful combination of *in situ* and *ex situ* techniques to follow growth and phase stabilities of TM-Al-N alloys.
- ... shown the impact of lattice match, epitaxy, and choices of substrates, and seed layers on the final film structure.
- ... demonstrated the importance in parallel use of *ab-initio* calculations and experiments to obtain a deeper understanding of growth and phase stabilities of TM-Al-N alloys.
- ... shown that there can be a significant difference between relaxed bulk thermodynamics and epitaxial thin film growth of multinary nitrides.

More specifically, I have shown...

- ... that Sc_3AlN can be deposited as a single-crystal thin film, has a lattice parameter of 4.40 \AA , and is thermodynamically stable.
- ... that an Al molar fraction of at least $x = 0.6$ can be dissolved into rocksalt structure (c-) $Sc_{1-x}Al_xN$ using magnetron sputter epitaxy at $600 \text{ }^\circ\text{C}$ and $p \leq 1 \text{ atm}$.
- ... that up to four epitaxial relationships exist between $ScN(111)$ and AlN-rich $Sc_{1-x}Al_xN$.
- ... that the decomposition mechanism in c- $Sc_{1-x}Al_xN$ is the volume mismatch between the binaries.

- ... that the first indications for phase separation of $c\text{-Sc}_{1-x}\text{Al}_x\text{N}$ are visible at 1000 °C, and that the topotaxial relationship between the binaries after phase separation is $\text{AlN}(0001) \parallel \text{ScN}(001)$ and $\text{AlN}\langle 0\bar{1}10 \rangle \parallel \text{ScN}\langle \bar{1}10 \rangle$.
- ... that the molar ScN solubility in single-crystal wurtzite-structure $\text{Sc}_{1-x}\text{Al}_x\text{N}$ is 22% under the applied growth conditions.
- ... that a solid state reaction between $\text{Ti}(0001)$ and $\text{AlN}(0001)$ multilayers takes place, which lowers the temperature for $\text{Ti}_2\text{AlN}(0001)$ formation by 175 °C to 500 °C.
- ... that understoichiometric TiN_x reacts with Al_2O_3 substrates, forming $\text{Ti}_2\text{Al}(\text{O},\text{N})$, the first reported oxygen containing MAX phase nitride.
- ... that Ti_4AlN_3 can not easily be grown in a standard deposition process, because low temperatures hinder the partitioning of elements along the c -axis yielding irregularly stacked $\text{Ti}_{n+1}\text{Al}_n\text{N}$ layers, while increasing temperatures result in Al loss to the vacuum.

- ¹ C. Höglund, *Effects of scandium on mechanical properties and microstructure in aluminium alloys*, Techn. Report No: LITH-IFM-EX—05/1520--SE (Linköping University, Linköping, Sweden, 2005).
- ² J. Birch, T. Joelsson, F. Eriksson, N. Ghafoor, and L. Hultman, *Single crystal CrN/ScN superlattice soft X-ray mirrors : Epitaxial growth, structure, and properties*, *Thin Solid Films* **514**, 10 (2006).
- ³ T. Joelsson, A. Hörling, J. Birch, and L. Hultman, *Single-crystal Ti₂AlN thin films*, *Applied Physics Letters* **86**, 111913 (2005).
- ⁴ M. Beckers, N. Schell, R. M. S. Martins, A. Mücklich, W. Möller, and L. Hultman, *Microstructure and nonbasal-plane growth of epitaxial Ti₂AlN thin films*, *Journal of Applied Physics* **99**, 034902 (2006).
- ⁵ T. Joelsson, A. Flink, J. Birch, and L. Hultman, *Deposition of single-crystal Ti₂AlN thin films by reactive magnetron sputtering from a 2Ti:Al compound target*, *Journal of Applied Physics* **102**, 074918 (2007).
- ⁶ M. Beckers, N. Schell, R. M. S. Martins, A. Mücklich, and W. Möller, *Phase stability of epitaxially grown Ti₂AlN thin films*, *Applied Physics Letters* **89**, 074101 (2006).
- ⁷ Wikipedia.com, “Scandium”, (2010-04-20).
- ⁸ C. Kittel, *Introduction to solid state physics, 7th edition* (John Miley & Sons, Inc, Hoboken, USA, 1996).
- ⁹ Z. Ahmad, *The properties and application of Scandium-reinforced aluminum*, *Journal of the Minerals Metals & Materials Society* **55**, 35 (2003).
- ¹⁰ L. S. Kramer, W. T. Tack, and M. T. Fernandes, *Scandium in aluminum alloys*, *Advanced Materials and Processes* **10**, 23 (1997).
- ¹¹ Easton Technology report, www.eastonbike.com/downloadable_files_unprotected/r&d_files/R&D-03%20Scandium.pdf, (2010-04-20).
- ¹² IUPAC. *Compendium of chemical terminology*, 2nd ed. (the "Gold Book"). Compiled by A. D. McNaught and A. Wilkinson. (Blackwell Scientific Publications, Oxford, 1997).
- ¹³ www.stanfordmaterials.com/sc.html?gclid=CLifnO_RzqACFUWU3wod8E2x0A, (2010-03-23).
- ¹⁴ <http://www.webelements.com/aluminium/history.html>, (2010-04-20).
- ¹⁵ Wikipedia.com, “Aluminum”, (2010-02-17).
- ¹⁶ <http://www.webelements.com/nitrogen/history.html>, (2010-04-20).

- ¹⁷ Wikipedia.com, “Nitrogen”, (2010-04-20).
- ¹⁸ W. Lengauer, *Investigations in the scandium-nitrogen system*, Journal of Solid State Chemistry **76**, 412 (1988).
- ¹⁹ D. Gall, I. Petrov, N. Hellgren, L. Hultman, J.-E. Sundgren, and J. E. Greene, *Growth of poly- and single-crystal ScN on MgO(111): Role of low-energy N₂⁺ irradiation in determining texture, microstructure evolution, and mechanical properties*, Journal of Applied Physics **84**, 6034 (1998).
- ²⁰ K. A. Gschneider, Jr., G. A. Melson, D. A. Melson, D. H. Youngblood, and H. H. Schock, in *Scandium: Its occurrence*, edited by C. T. Horovitz (Academic, London, 1975), Vol. 165, cited in Ref. 32.
- ²¹ W. R. L. Lambrecht, *Electronic structure and optical spectra of the semimetal ScAs and of the indirect-band-gap semiconductor ScN and GaN*, Physical Review B **62**, 13538 (2000).
- ²² D. Gall, M. Städele, K. Järrendahl, I. Petrov, P. Desjardins, R. T. Haasch, T.-Y. Lee, and J. E. Greene, *Electronic structure of ScN determined using optical spectroscopy, photoemission, and ab initio calculations*, Physical Review B **63**, 125119 (2001).
- ²³ C. Stampfl, W. Mannstadt, R. Asahi, and A. J. Freeman, *Electronic structure and physical properties of early transition metal mononitrides: Density functional theory LDA, GGA, and screened-exchange LDA FLAPW calculations*, Physical Review B **63**, 155106 (2001).
- ²⁴ H. A. Al-Brithen, A. R. Smith, and D. Gall, *Surface and bulk electronic structure of ScN(001) investigated by scanning tunneling microscopy/spectroscopy and optical absorption spectroscopy*, Physical Review B **70**, 045303 (2004).
- ²⁵ J. P. Dismukes, W. M. Yim, J. J. Tietjen, and R. E. Novak, *Vapor deposition of semiconducting mononitrides of scandium, yttrium, and the rare- earth elements*, RCA Review **31**, 680 (1970).
- ²⁶ J. P. Dismukes, W. M. Yim, and V. S. Ban, *Epitaxial growth of semiconducting ScN*, Journal of Crystal Growth **13/14**, 365 (1972).
- ²⁷ J. P. Dismukes, W. M. Yim, J. J. Tietjen, and R. E. Novak, *Vapor deposition of semiconducting mononitrides of Sc, Y, and the rare earth elements*, Journal of Crystal Growth **9**, 295 (1971).
- ²⁸ D. Gall, I. Petrov, L. D. Madsen, J.-E. Sundgren, and J. E. Greene, *Microstructure and electronic properties of the refractory semiconductor ScN grown on MgO by ultra-high-vacuum reactive magnetron sputter deposition*, Journal of Vacuum Science and Technology **16**, 2411 (1998).
- ²⁹ H. Al-Brithen, and A. R. Smith, *Molecular beam epitaxy growth of atomically smooth scandium nitride films*, Applied Physics Letters **77**, 2485 (2000).

- ³⁰ M. A. Moram, T. B. Joyce, P. R. Chalker, Z. H. Barber, and C. J. Humphreys, *Microstructure of epitaxial scandium nitride films grown on silicon*, Applied Surface Science **252**, 8385 (2006).
- ³¹ M. A. Moram, Z. H. Barber, and C. J. Humphreys, *The effect of oxygen incorporation in sputtered scandium nitride films*, Thin Solid Films **516**, 8569 (2008).
- ³² N. Farrer and L. Bellaiche, *Properties of hexagonal ScN versus wurtzite GaN and InN*, Physical Review B **66**, 201203 (2002).
- ³³ V. Ranjan, S. Bin-Omran, D. Sichuga, R. S. Nichols, L. Bellaiche, and A. Alsaad, *Properties of GaN/ScN and InN/ScN superlattices from first principles*, Physical Review B **72**, 085315 (2005).
- ³⁴ W. M. Yim, E. J. Stofko, P. J. Zanzucchi, J. I. Pankove, M. Ettenberg, and S. L. Gilbert, *Epitaxially grown AlN and its optical band gap*, Journal of Applied Physics **44**, 292 (1973).
- ³⁵ P. Limsuwan, N. Udomkan, S. Meejoo, and P. Winotai, *Surface morphology of submicron crystals in aluminum nitride films grown by DC magnetron sputtering*, International Journal of Modern Physics B **19**, 2073 (2005).
- ³⁶ A. Kumar, H. L. Chan, J. J. Weimer, and L. Sanderson, *Structural characterization of pulsed laser-deposited AlN thin films on semiconductor substrates*, Thin Solid Films **308**, 406 (1997).
- ³⁷ G. A. Slack, R. A. Tanzilli, R. O. Pohl and J. W. Vandersande, *The intrinsic thermal conductivity of AlN*, Journal of Physics and Chemistry of Solids **48**, 641 (1987).
- ³⁸ Y. Baik, and R. A. L. Drew, *Aluminum nitride: Processing and Applications*, Key Engineering Materials **122-124**, 553 (1996).
- ³⁹ W. T. Lin, L. C. Meng, G. J. Chen, and H. S. Liu, *Epitaxial growth of cubic AlN films on (001) and (111) silicon by pulsed laser ablation*, Applied Physics Letters **66**, 2066 (1995).
- ⁴⁰ P. H. Mayrhofer, A. Hörling, L. Karlsson, J. Sjöln, C. Mitterer, and L. Hultman, *Self-organized nanostructures in the Ti-Al-N system*, Applied Physics Letters **83**, 2049 (2003).
- ⁴¹ F. Adibi, I. Petrov, L. Hultman, U. Wahlström, T. Shimizu, D. McIntyre, J. E. Greene, and J.-E. Sundgren, *Defect structure and phase transitions in epitaxial metastable cubic $Ti_{0.5}Al_{0.5}N$ alloys grown on MgO(001) by ultra-high-vacuum magnetron sputter deposition*, Journal of Applied Physics **69**, 6437 (1991).
- ⁴² A. Hörling, L. Hultman, M. Odén, J. Sjöln, and L. Karlsson, *Thermal stability of arc evaporated high aluminum-content $Ti_{1-x}Al_xN$ thin films*, Journal of Vacuum Science and Technology A **20(5)**, 1815 (2002).
- ⁴³ T. B. Massalski, *Binary alloy phase diagrams* (ASM International, Ohio, USA, 1986).

- ⁴⁴ J. C. Schuster and J. Bauer, *The ternary systems Sc-Al-N and Y-Al-N*, Journal of Less-Common Metals **109**, 345 (1985).
- ⁴⁵ M. Magnuson, M. Mattesini, C. Höglund, I. A. Abrikosov, J. Birch, and L. Hultman, *Electronic structure investigation of the cubic inverse perovskite Sc₃AlN*, Physical Review B **78**, 235102 (2008).
- ⁴⁶ A. S. Mikhaylushkin, C. Höglund, J. Birch, Zs. Czigány, L. Hultman, S. I. Simak, B. Alling, F. Tasnádi, and I. A. Abrikosov, *Stability of the ternary perovskites Sc₃EN (E=B, Al, Ga, In) from first principles*, Physical Review B **79**, 134107 (2009).
- ⁴⁷ M. Mattesini, M. Magnuson, F. Tasnádi, C. Höglund, I. A. Abrikosov, and L. Hultman, *Elastic properties and electrical correlations in ternary scandium-based cubic inverse perovskites: A first-principles study*, Physical Review B **79**, 125122 (2009).
- ⁴⁸ B. Alling, A. Karimi, and I. A. Abrikosov, *Electronic origin of the isostructural decomposition in cubic M_{1-x}Al_xN (M=Ti, Cr, Sc, Hf): A first principles study*, Surface and Coatings Technology **203**, 883 (2008).
- ⁴⁹ M. Akiyama, T. Kamohara, K. Kano, A. Teshigahara, Y. Takeuchi, and N. Kawahara, *Enhancement of piezoelectric response in scandium aluminum nitride alloy thin films prepared by dual reactive cosputtering*, Advanced Materials **21**, 593 (2009).
- ⁵⁰ M. Akiyama, K. Kano, and A. Teshigahara, *Influence of growth temperature and scandium concentration on piezoelectric response of scandium aluminum nitride alloy thin films*, Applied Physics Letters **95**, 162107 (2009).
- ⁵¹ F. Tasnádi, B. Alling, C. Höglund, G. Wingqvist, J. Birch, L. Hultman, and I. A. Abrikosov, *Origin of anomalous piezoelectric response in wurtzite Sc_xAl_{1-x}N alloys*, Physical Review Letters **104**, 137601 (2010).
- ⁵² T. Bohnen, G. R. Yazdi, R. Yakimova, G. W. G. van Dreumel, P. R. Hageman, E. Vlieg, R. E. Algra, M. A. Verheijen, and J. H. Edgar, *ScAlN nanowires: A cathodoluminescence study*, Journal of Crystal Growth **311**, 3147 (2009).
- ⁵³ W. W. Lei, D. Liu, P. W. Zhu, X. H. Chen, Q. Zhao, G. H. Wen, Q. L. Cui, and G. T. Zou, *Ferromagnetic Sc-doped AlN sixfold-symmetrical hierarchical nanostructures*, Applied Physics Letters **95**, 162501 (2009).
- ⁵⁴ Wikipedia.com, “Titanium”, (2010-04-20).
- ⁵⁵ Wikipedia .com, “Titan”, (2010-04-20).
- ⁵⁶ C. Y. Ting, *TiN formed by evaporation as a diffusion barrier between Al and Si*, Journal of Vacuum Science and Technology **21**, 14 (1982).
- ⁵⁷ S.-K. Rha, S.-Y. Lee, W.-J. Lee, Y.-S. Hwang, C.-O. Park, D.-W. Kim, Y.-S. Lee, and C.-N. Whang, *Characterization of TiN barriers against Cu diffusion by capacitance-voltage measurement*, Journal of Vacuum Science and Technology B **16**, 2019 (1998).

- ⁵⁸ J. S. Zabinski and A. A. Voevodin, *Recent development in the design, deposition, and processing of hard coatings*, Journal of Vacuum Science and Technology A **16**, 1890 (1998).
- ⁵⁹ P. Roquiny, F. Bodart, and G. Terwagne, *Colour control of titanium nitride coatings produced by reactive magnetron sputtering at temperature less than 100 °C*, Surface and Coatings Technology **116-119**, 278 (1999).
- ⁶⁰ H. Ichimura and A. Kawana, *High temperature oxidation of ion-plated TiN and TiAlN films*, Journal of Materials Research **8**, 1093 (1993).
- ⁶¹ P. Panjan, B. Navinsek, A. Cvelbar, A. Zalar and I. Milosev, *Oxidation of TiN, ZrN, TiZrN, CrN, TiCrN and TiN/CrN multilayer hard coatings reactively sputtered at low temperature*, Thin Solid Films **281-282**, 298 (1996).
- ⁶² W. Jeitschko, H. Nowotny, and F. Benesovsky, *Ti₂AlN, eine stickstoffhaltige H-Phase*, Monatshefte für Chemie **94**, 1198 (1963).
- ⁶³ J. C. Schuster, and J. Bauer, *The ternary system titanium-aluminum-nitrogen*, Journal of Solid State Chemistry **53**, 260 (1984).
- ⁶⁴ M. W. Barsoum, L. Farber, I. Levin, A. Procopio, T. El-Raghy, and A. Berner, *High-resolution transmission electron microscopy of Ti₄AlN₃, or Ti₃Al₂N₂ revisited*, Journal of American Ceramic Society **82**, 2545 (1999).
- ⁶⁵ B. Holm, R. Ahuja, S. Li, and B. Johansson, *Theory of the ternary layered system Ti-Al-N*, Journal of Applied Physics **91**, 9874 (2002).
- ⁶⁶ A. T. Procopio, T. El-Raghy, and M. W. Barsoum, *Synthesis of Ti₄AlN₃ and phase equilibria in the Ti-Al-N system*, Metallurgical and Materials Transactions A **31**, 373 (2000).
- ⁶⁷ O. Knotek, W. D. Münz, and T. Leyendecker, *Industrial deposition of binary, ternary, and quarternary nitrides of titanium, zirconium, and aluminum*, Journal of Vacuum Science and Technology A **5**, 2173 (1987).
- ⁶⁸ K. Kutschej, P. H. Mayrhofer, M. Kathrein, P. Polcik, R. Tessadri, and C. Mitterer, *Structure, mechanical and tribological properties of sputtered Ti_{1-x}Al_xN coatings with 0.5 ≤ x ≤ 0.75*, Surface and Coatings Technology **200**, 2358 (2005).
- ⁶⁹ H. A. Jehn, S. Hofmann, V.-E. Rückborn, and W.-D. Münz, *Morphology and properties of sputtered (Ti,Al)N layers on high speed steel substrates as a function of deposition temperature and sputtering atmosphere*, Journal of Vacuum Science and Technology A **4**, 2717 (1986).
- ⁷⁰ L. E. Toth, *Transition metal carbides and nitrides* (Academic Press, New York, USA, 1971).
- ⁷¹ Mineralogical Society of America, *Handbook of mineralogy*, www.handbookofmineralogy.org, (2010-03-21).

- 72 C. Giacobazzo, H. L. Monaco, G. Artioli, D. Viterbo, G. Ferraris, G. Gilli, G. Zanotti, and M. Catti, *Fundamentals of crystallography, Second edition*, (Oxford University Press, Oxford New York, USA, 2002).
- 73 S. Limpijumngong, and W. R. L. Lambrecht, *Theoretical study of the relative stability of wurtzite and rocksalt phases in MgO and GaN*, Physical Review B **63**, 104103 (2001).
- 74 H. Nowotny, *Strukturchemie einiger Verbindungen der Übergangsmetalle mit den Elementen C, Si, Ge, Sn*, Progress in Solid State Chemistry **5**, 27 (1971).
- 75 M. W. Barsoum, *The $M_{N+1}AX_N$ phases: A new class of solids*, Progress in Solid State Chemistry **28**, 201 (2000).
- 76 T. Seppänen, *Ti₃SiC₂ thin films*, Technical Report no: R-229 (Linköping University, Linköping, Sweden, 2001).
- 77 T. Seppänen, J. -P. Palmquist, P. O. Å. Persson, J. Emmerlich, J. Molina, J. Birch, U. Jansson, P. Isberg, and L. Hultman, *Proceedings of the SCANDEM 2002*, Tampere, Finland, 2002, p 142.
- 78 J. P. Palmquist, U. Jansson, T. Seppänen, P. O. Å. Persson, J. Birch, L. Hultman, and P. Isberg, *Magnetron sputtered epitaxial single-phase Ti₃SiC₂ thin films*, Applied Physics Letters **81**, 835 (2002).
- 79 G. Rose, *Beschreibung einiger neuen Mineralien des Urals*, Annalen der Physikalischen Chemie **48**, 551 (1839).
- 80 A. von Hippel, R. G. Breckenridge, A. P. de Bretteville Jr., J. M. Brownlow, F. G. Chesley, G. Oster, L. Tisza, and W. B. Westphal, NRDC Report No. 300 (1944).
- 81 A. W. Sleight, J. L. Gillson, and P. E. Bierstedt, *High-temperature superconductivity in the BaPb_{1-x}Bi_xO₃ system*, Solid State Communications **17**, 27 (1975).
- 82 S. N. Putilin, E. V. Antipov, and M. Marezio, *Superconductivity above 120 K in HgBa₂CaCu₂O_{6+δ}*, Physica C **212**, 266 (1993).
- 83 R. von Helmolt, J. Wecker, K. Samwer, and K. Bärner, *Transport properties of manganates with giant magnetoresistance*, Journal of Magnetism and Magnetic Materials **151**, 411 (1995).
- 84 M. Y. Chern, D. A. Vennos, and F. J. DiSalvo, *Synthesis, structure, and properties of anti-perovskite nitrides Ca₃MN, M = P, As, Sb, Ge, Sn, and Pb*, Journal of Solid State Chemistry **96**, 415 (1992).
- 85 R. Niewa, W. Schnelle, and F. R. Wagner, *Synthesis, crystal structure, and physical properties of (Ca₃N)Tl*, Zeitschrift Anorganischer Allgemeiner Chemie **627**, 365 (2001).
- 86 M. Kirchner, W. Schnelle, F. R. Wagner, R. Niewa, *Preparation, crystal structure and physical properties of ternary compounds (R₃N)In, R = rare-earth metal*, Solid State Science **5**, 1247 (2003).

- ⁸⁷ K. Adomi, J.-I. Chyi, S. F. Fang, T. C. Shen, S. Strite, and H. Morkoc, *Molecular beam epitaxial growth of GaAs and other compound semiconductors*, *Thin Solid Films* **205**, 182 (1991).
- ⁸⁸ T. Seppänen, *Growth and characterization of metastable wide band-gap $Al_{1-x}In_xN$ epilayers*, Ph.D. dissertation No. 1027, Linköping Studies in Science and Technology, 2006.
- ⁸⁹ K. Bobzin, E. Lugscheider, R. Nickel, and P. Immich, *($Cr_{1-x}Al_x$)N ein Review über ein vielseitig einsetzbares Schichtsystem*, *Materialwissenschaft und Werkstofftechnik* **37**, 833 (2006).
- ⁹⁰ L. Vegard, *Die Konstitution der Mischkristalle und die Raumfüllung der Atome*, *Zeitschrift für Physik* **5**, 17 (1921).
- ⁹¹ T. Seppänen, L. Hultman, J. Birch, M. Beckers, and U. Kreissig, *Deviations from Vegard's rule in $Al_{1-x}In_xN$ (0001) alloy thin films grown by magnetron sputter epitaxy*, *Journal of Applied Physics* **101**, 043519 (2007).
- ⁹² P. Hohenberg and W. Kohn, *Inhomogenous electron gas*, *Physical Review B* **136**, 864 (1964).
- ⁹³ W. Kohn and L. J. Sham, *Self-consistent equations including exchange and correlation effects*, *Physical Review A* **140**, 1133 (1965).
- ⁹⁴ R. M. Martin, *Electronic structure, basic theory and practical methods* (Cambridge University Press, Cambridge, UK, 2004).
- ⁹⁵ J. Perdew, K. Burke, and M. Ernzerhof, *Generalized gradient approximation made simple*, *Physical Review Letters* **77**, 3865 (1996).
- ⁹⁶ P. E. Blöchl, *Projector augmented-wave method*, *Physical Review B* **50**, 17953 (1994).
- ⁹⁷ G. Kresse, and J. Hafner, *Ab initio molecular dynamics for open-shell transition metals*, *Physical Review B* **48**, 13115 (1993).
- ⁹⁸ G. Kresse, and D. Joubert, *From ultrasoft pseudopotentials to the projector augmented-wave method*, *Physical Review B* **50**, 1758 (1999).
- ⁹⁹ G. Kresse, and J. Hafner, *Ab initio molecular-dynamics simulation of the liquid-metal–amorphous-semiconductor transition in germanium*, *Physical Review B* **49**, 14251 (1994).
- ¹⁰⁰ A. Zunger, S. H. Wei, L. G. Ferreira, and J. E. Bernard, *Special quasirandom structures*, *Physical Review Letters* **65**, 353 (1990).
- ¹⁰¹ M. Dahlqvist, B. Alling, I. A. Abrikosov, and J. Rosén, *Phase stability of Ti_2AlC upon oxygen incorporation : A first-principles investigation*, *Physical Review B* **81**, 024111 (2010).
- ¹⁰² B. Alling, M. Dahlqvist *et al.*, unpublished.

- ¹⁰³ B. Alling, *A theoretical study of disorder and decomposition in multinary nitrides hard coatings materials*, Ph.D. dissertation No. 4430, École Polytechnique Fédérale de Lausanne, 2009.
- ¹⁰⁴ H. Holleck, *Metastable coatings – prediction of composition and structure*, Surface and Coatings Technology **36**, 151 (1988).
- ¹⁰⁵ L. Weber, *Das viergliedrige Zonensymbol des hexagonalen systems*, Zeitschrift für Kristallographie, Kristallgeometrie, Kristallphysik, Kristallchemie **57**, 200 (1922).
- ¹⁰⁶ F. C. Frank, *On Miller-Bravias indices and four-dimensional vectors*, Acta Crystallografica **18**, 862 (1965).
- ¹⁰⁷ D. B. Williams, and C. B. Carter, *Transmission electron microscopy* (Springer, New York, USA, 1996).
- ¹⁰⁸ CaRIne Crystallography 3.1, C.Boudias & D.Monceau (1989-1998).
- ¹⁰⁹ J. M. Zuo and J. C. Mabon, Web-based Electron Microscopy Application Software: Web-EMAPS, Microsc Microanal 10(Suppl 2), 2004; <http://emaps.mrl.uiuc.edu/>, (2010-04-20).
- ¹¹⁰ B. D. Cullity, *Elements of X-ray diffraction* (Addison-Wesley Publishing Company, New Jersey, USA, 2001).
- ¹¹¹ M. Ohring, *Materials science of thin films* (Academic Press, San Diego, USA, 2002).
- ¹¹² H. Vollstädt, E. Ito, M. Akaishi, S. Akimoto, and O. Fukunaga, *High pressure synthesis of rocksalt type of AlN*, Proceedings of the Japan Academy B **66**, 7 (1990).
- ¹¹³ M. Beckers, N. Schell, R. M. S. Martins, A. Mücklich, W. Möller, and L. Hultman, *Nucleation and growth of Ti₂AlN thin films deposited by reactive magnetron sputtering onto MgO(111)*, Journal of Applied Physics **102**, 074916 (2007).
- ¹¹⁴ P. O. Å. Persson, J. Rosén, D. R. McKenzie, M. M. M. Bilek, and C. Höglund, *A solid phase reaction between TiC_x thin films and Al₂O₃ substrates*, Journal of Applied Physics **103**, 066102 (2008).
- ¹¹⁵ D. J. Seol, S. Y. Hu, Y. L. Li, J. Shen, K. H. Oh, and L. Q. Chen, *Computer simulation of spinodal decomposition in constrained films*, Acta Materialia **51**, 5173 (2003).
- ¹¹⁶ M. Beckers, F. Eriksson, and C. Baehtz, Experimental Report from experiment HS 3443 in *Bi-Annual Report 2007/2008, The Rossendorf-Beamline at ESRF, FZD-517* (2009).
- ¹¹⁷ Svenska Vakuüm Sällskapet, *Grunderna i tillämpad vakuümteknik* (Svenska Vakuüm Sällskapet, Sweden, 1989).
- ¹¹⁸ Wikipedia.com, “monolayer”, (2010-04-20).
- ¹¹⁹ R. Ranjan, J. P. Allain, M. R. Hendricks, and D. N. Ruzic, *Absolute sputtering yield of Ti/TiN by Ar⁺/N⁺ at 400-700 eV*, Journal of Vacuum Science and Technology A **19**, 1004 (2001).

- ¹²⁰ S. Berg, M. Moradi, C. Nender, and H.-O. Blom, *The use of process modelling for optimum design of reactive sputtering processes*, Surface and Coatings Technology **39/40**, 465 (1989).
- ¹²¹ S. Berg, T. Larsson, C. Nender, and H.-O. Blom, *Predicting thin-film stoichiometry in reactive sputtering*, Journal of Applied Physics **63**, 887 (1988).
- ¹²² S. Berg, H.-O. Blom, T. Larsson, and C. Nender, *Modeling of reactive sputtering of compound materials*, Journal of Vacuum Science and Technology A **5**, 202 (1987).
- ¹²³ J. Birch, S. Tungasmita, and V. Darakchieva, *Magnetron sputter epitaxy of AlN, Vacuum science and technology: Nitrides as seen by the technology*, Research Signpost **37/661**, 421 (2002).
- ¹²⁴ I. Petrov, P. B. Barna, L. Hultman, and J. E. Greene, *Microstructural evolution during film growth*, Journal of Vacuum Science and Technology A **21**, S117 (2003).
- ¹²⁵ D. Gall, S. Kodambaka, M. A. Wall, I. Petrov, and J. E. Greene, *Pathways of atomistic processes on TiN(001) and (111) surfaces during film growth: an ab initio study*, Journal of Applied Physic **93**, 9086 (2003).
- ¹²⁶ M. A. Wall, D. G. Cahill, I. Petrov, D. Gall, and J. E. Greene, *Nucleation kinetics versus nitrogen partial pressure during homoepitaxial growth of stoichiometric TiN(001): A scanning tunneling microscopy study*, Surface Science **581**, L122 (2005).
- ¹²⁷ P. O. Å. Persson, S. Kodambaka, I. Petrov, and L. Hultman, *Epitaxial Ti₂AlN(0001) thin film deposition by dual-target reactive magnetron sputtering*, Acta Materialia **55**, 4401 (2007).
- ¹²⁸ J. R. Bird, and J. S. Williams, *Ion beams for materials analysis* (Academic Press, Australia, 1989).
- ¹²⁹ J. R. Tesmer, and M. Nastasi, *Handbook of modern ion beam materials analysis* (MRS, Pittsburgh, USA, 1995).
- ¹³⁰ D. D. Cohen, R. Bird, N. Dytlewski, and R. Siegele, *Ion beams for materials analysis, encyclopedia of physical science and technology*, (Academic Press, 2001).
- ¹³¹ W. Chu, J. W. Mayer, M. A. Nicolet, *Backscattering spectrometry*, (Academic Press, 1978).
- ¹³² www.simnra.com, (2010-03-25).
- ¹³⁴ B. D. Cullity, *Elements of X-ray diffraction* (Prentice Hall, New Jersey, USA, 2001).
- ¹³⁵ D. Halliday, R. Resnick, and J. Walker, *Fundamentals of physics*, 7th Edition (John Wiley & Sons, USA 2005).
- ¹³⁶ M. Birkholz, *Thin film analysis by X-ray scattering* (Wiley-VCH, Weinheim, Germany, 2006).

- ¹³⁸ E. Vlieg, A. W. Denier van der Gon, J. F. van der Veen, J. E. Macdonald, and C. Norris, *Surface X-ray scattering during crystal growth: Ge on Ge(111)*, *Physical Review Letters* **61**, 2241 (1988).
- ¹⁴⁰ L. J. van der Pauw, *A method of measuring specific resistivity and Hall effect of discs of arbitrary shape*, *Philips Research Reports* **13**, 1 (1958).
- ¹⁴¹ W. C. Oliver, and G. M. Pharr, *An improved technique for determining hardness and elastic modulus using load and displacement sensing indentation experiments*, *Journal of Materials Research* **7**, 1564 (1992).
- ¹⁴² D. Gall, I. Petrov, N. Hellgren, L. Hultman, J. E. Sundgren, and J. E. Greene, *Microstructure and electronic properties of the refractory semiconductor ScN grown on MgO(001) by ultra-high-vacuum reactive magnetron sputter deposition*, *Journal of Applied Physics* **84**, 6034 (1998).
- ¹⁴³ O. Wilhelmsson, J. P. Palmquist, E. Lewin, J. Emmerlich, P. Eklund, P. O. Å. Persson, H. Högberg, S. Li, R. Ahuja, O. Eriksson, L. Hultman, and U. Jansson, *Deposition and characterization of ternary thin films within the Ti-Al-C system by DC magnetron sputtering*, *Journal of Crystal Growth* **291**, 290 (2006).